Jagellonian University
Institute of Physics

Study of the production mechanism of the η meson in proton-proton collisions by means of analysing power measurements

Rafał Czyżykiewicz

A doctoral dissertation prepared at the Institute of Nuclear Physics of the Jagellonian University and at the Institute of Nuclear Physics of the Research Centre Jülich, submitted to the Faculty of Physics, Astronomy and Applied Computer Science at the Jagellonian University, conferred by Dr. hab. Paweł Moskal

Cracow 2006

Uniwersytet Jagielloński
Instytut Fizyki

Badanie mechanizmu produkcji mezonu η w zderzeniach proton-proton za pomocą pomiarów zdolności analizującej

Rafał Czyżykiewicz

Praca na stopień doktora nauk fizycznych wykonana w Zakładzie Fizyki Jądrowej Instytutu Fizyki Uniwersytetu Jagiellońskiego oraz w Instytucie Fizyki Jądrowej Centrum Badawczego Jülich pod kierunkiem dr hab. Pawła Moskala, przedstawiona Radzie Wydziału Fizyki, Astronomii i Informatyki Stosowanej Uniwersytetu Jagiellońskiego.

Kraków 2006

Abstract

The analysing power measurements for the $\vec{p}p \to pp\eta$ reaction studied in this dissertation are used in the determination of the reaction mechanism of the η meson production in nucleon-nucleon collisions.

Measurements have been performed in the close-to-threshold energy region at beam momenta of $p_{beam} = 2.010$ and 2.085 GeV/c, corresponding to the excess energies of Q = 10 and 36 MeV, respectively. The experiments were realised by means of a cooler synchrotron and storage ring COSY along with a cluster jet target. For registration of the reaction products the COSY-11 facility has been used. The identification of the η meson has been performed with the missing mass method.

The results for the angular dependence of the analysing power combined with the hitherto determined isospin dependence of the total cross section for the η meson production in the nucleon-nucleon collisions, reveal a statistically significant indication that the excitation of the nucleon to the S_{11} resonance, the process which intermediates the production of the η meson, is predominantly due to the exchange of a π meson between the colliding nucleons.

The determined values of the analysing power at both excess energies are consistent with zero implying that the η meson is produced predominantly in the s-wave at both excess energies.

Streszczenie

Zaprezentowane w tej pracy pomiary zdolności analizującej dla reakcji $\vec{p}p \to pp\eta$ mają na celu wyznaczenie mechanizmu produkcji mezonu η w zderzeniach nukleonów.

Pomiary wykonano w przyprogowym obszarze energii. W eksperymentach wykorzystano wiązkę protonów spolaryzowanych poprzecznie o pędach $p_{beam} = 2.010$ i 2.085 GeV/c, odpowiadających energiom wzbudzenia Q = 10 oraz 36 MeV dla reakcji $\vec{p}p \to pp\eta$. Do badań wykorzystano synchrotron COSY, tarczę klastrową, oraz system detekcyjny COSY-11. W doświadczeniach rejestrowano produkty reakcji obdarzone ładunkiem elektrycznym, natomiast identyfikacji mezonu η dokonano za pomocą metody masy brakującej.

Uzyskane doświadczalnie rozkłady kątowe zdolności analizującej, w połączeniu ze zmierzoną uprzednio zależnością izospinową produkcji mezonu η w zderzeniach nukleon-nukleon, pozwalają stwierdzić, iż wzbudzenie nukleonu do rezonansu $S_{11}(1535)$ – proces pośredniczący w produkcji mezonu η – następuje w głównej mierze poprzez wymianę mezonu π pomiędzy zderzającymi się nukleonami.

Wartości zdolności analizującej dla obu energii wzbudzenia są równe zeru w granicach błędów statystycznych, co wskazuje, iż mezon η jest w głównej mierze produkowany w fali s.

Contents

Chapter 1

Introduction

The main goal of this dissertation is the closer insight into the production mechanism of the η meson in the interaction of nucleons. Despite the fact that the discovery of this meson – a member of the pseudoscalar meson nonet (see Appendix A) – took place almost half a century ago [1] its production dynamics has remained an open question for a long time.

From the precise and extensive measurements of the total cross section for the η meson production in the $pp \to pp\eta$ reaction in the close-to-threshold region [2–10] it was concluded [11] that this process proceeds through the excitation of one of the protons to the $S_{11}(1535)$ state which subsequently deexcites via the emission of the η meson and a proton. The crucial observations here were the large value of the absolute cross section and isotropic distributions of the angle of the η meson emission in the reactions centre-of-mass system [8, 12]. However, there are plenty of possible scenarios of the excitation of $S_{11}(1535)$. In fact, any of the π, η, ω or/and ρ mesons may contribute to the resonance creation. Taking solely into account the total cross section one cannot deduce which one out of this rich spectrum of mesons plays the most important role in the excitation of the intermediate resonance.

Further investigations of the η meson production process, namely the determination of the isospin dependence of the total cross section by the WASA/PROMICE collaboration [13], put some restrictions to the above-mentioned possibilities of the resonance excitation process. The ratio $R_\eta = \sigma(pn \to pn\eta)/\sigma(pp \to pp\eta)$ was determined to be about 6.5 in the excess energy range between 16 and 109 MeV, which revealed strong isospin dependence of the production process. The production of the η meson with the total isospin $I = 0$ exceeds the production with the isospin $I = 1$ by a factor of 12, suggesting [13] that the isovector meson exchange – the π or/and ρ meson exchange – is the dominant process in the excitation of the S_{11} resonance. However, the relative contributions of the pseudoscalar π meson and vector ρ meson still remained to be determined.

Here the measurements of the polarisation observables can assist, because the predictions of the one boson exchange models [11, 14] with respect to the most

basic polarisation observable as the analysing power are sensitive to the type of meson being exchanged between the protons in order to excite one of them into the resonant state. Measurements of the beam analysing power for the $\vec{p}p \to pp\eta$ reaction performed by the DISTO collaboration [15] as well as the tentative experiment of the COSY-11 group [16,17] did not bring the univocal solution of this problem. The interpretation of results of the DISTO measurements, performed in the far-from-threshold region at the excess energies of Q = 324, 412, and 554 MeV suffered from the lack of a theoretical prediction for the analysing power. This is due to the fact that far from the reaction threshold the higher partial waves are involved in the reaction process, and so the theoretical description becomes more complicated. COSY-11 results at the excess energy of Q = 40 MeV, due to the insufficient statistics, could not have been used in order to judge between the predictions of pseudoscalar and vector meson exchange models.

This gap is filled by the results of experiments described in this dissertation. For the first time ever the COSY-11 group was able to perform the measurements of the analysing power for the $\vec{p}p \to pp\eta$ reaction in the close-to-threshold region that has brought the answer to the open question of the η meson production mechanism in hadronic collisions.

It is worth mentioning that the precise determination of this mechanism – a process that proceeds through the strong interaction – delivers information about the nature of the strong forces. Thanks to the results presented in this dissertation the theoretical models might be revisited with new input parameters applied to these models: the coupling constants in the description of the production process of the η meson, the initial and final state interactions and also dimensions of the reaction region.

Experiments presented in this work have been performed by the COSY-11 collaboration by means of the COSY-11 facility [18–20] at the COoler SYnchrotron and storage ring COSY [21, 22] in the Research Center Jülich in Germany. The analysing powers have been measured during two runs at different beam momenta: p_{beam} = 2.010 GeV/c (May 2003) and 2.085 GeV/c (September 2002), which for the $\vec{p}p \to pp\eta$ reaction correspond to the excess energies of Q = 10 and 36 MeV, respectively.

This thesis consists of eight chapters. In the following one the basic definitions are given, which are important in the understanding of the general methods that are applied to the experiments with polarised beams. In particular the definitions of the spin of a quantum particle, the polarisation vector, and the analysing power are given. We introduce the reference frames used in the polarisation experiments, in particular we show how to construct the so called *Madison frame* following the Madison convention. This is relevant in order to determine the sign of the analysing power. At the end of this part of the thesis we derive the formula which will be used to determine the analysing power.

In Chapter 3 an overview of the theoretical models of the η meson production in hadronic collisions is sketched. Superimposed are the phenomenological models working within the *one boson exchange* frame. A special emphasis is put on the pseudoscalar meson exchange model of Nakayama et al. [11] and the vector meson exchange model of Fäldt and Wilkin [14] as these are the only models giving the predictions of the analysing power for the $\vec{p}p \to pp\eta$ process in the close-to-threshold region. The summary of the so far measured observables for the $pp \to pp\eta$ reaction and the conclusions from these measurements are given in this chapter.

The general description of the cooler synchrotron COSY along with the method of the formation and acceleration of the polarised proton beam are elucidated in Chapter 4. Also the experimental facility COSY-11 is briefly described. The detector setup and the method of analysis has been previously presented in various dissertations [23–25] so here we will only focus on the description of the detectors which are interesting from the point of view of the analysis of the $\vec{p}p \to pp\eta$ reaction.

In Chapter 5 the calibration of the detectors needed to register the $\vec{p}p \to pp\eta$ process is described. Also the methodology of the analysis is given i.e. the missing mass technique, identification of the beam spin mode from the number of elastically scattered events, the methods of determination of the production yields, relative luminosity, and the beam polarisation. At the end of this chapter the final results of both analyses are presented.

Chapter 6 contains the confrontation of the theoretical models with the experimentally determined values of the analysing power. Using statistical inference we conclude about the production mechanism of the η meson in hadronic collisions.

The possibilities of extending the experiments presented in this work are discussed in Chapter 7.

In Chapter 8 we summarize the thesis. Conclusions from the analyses presented in this dissertation can be found in this part.

Three appendices have been added at the end of this dissertation in order to elucidate in more detail some issues discussed in the text. We shall explain the differences between the pseudoscalar and vector mesons (Appendix A), prove a property of the analysing power (Appendix B) postulated and used in the analysis in Chapter 6. We will also demonstrate that the elastic scattering in the polarisation plane does not depend on the degree of polarisation (Appendix C), a property which originates from the parity invariance rule and is used in Section 5.3 for the calculation of the relative luminosity.

Chapter 2

Definitions

2.1 Spin and the beam polarisation

The formal quantum mechanical description of spin 1/2 particle is given. The polarisation vector and polarisation plane are defined.

The *spin* of a particle is an internal degree of freedom, which is governed by the same equations of motion as the angular momentum. Therefore, we can assign to observable "spin" a vectorial operator $\hat{\mathbf{S}} = [\hat{S}_x, \hat{S}_y, \hat{S}_z]$, where $\hat{S}_i$ (i=x,y,z) are the hermitian operators. Subsequently we will only consider the spin-1/2 particles. In this case the spin operators can be expressed in terms of the Pauli matrices σ_i:

$$\hat{S}_i = \frac{\hbar}{2}\sigma_i, \tag{2.1}$$

where

$$\sigma_x = \begin{pmatrix} 0 & 1 \\ 1 & 0 \end{pmatrix}, \sigma_y = \begin{pmatrix} 1 & 0 \\ 0 & -1 \end{pmatrix}, \sigma_z = \begin{pmatrix} 0 & -i \\ i & 0 \end{pmatrix}. \tag{2.2}$$

With respect to the arbitrary quantization axis Oy, a spin 1/2 particle can be found in one of the two eigenstates of $\hat{S}_y$. These eigenstates may be represented by the eigenfunctions

$$\chi_+ = \begin{pmatrix} 1 \\ 0 \end{pmatrix}, \chi_- = \begin{pmatrix} 0 \\ 1 \end{pmatrix}. \tag{2.3}$$

The $\chi_\pm$ are the eigenfunctions of $\hat{S}_y$ with the eigenvalues $\pm\hbar/2$. In what follows we will refer to the χ_+ and χ_- states as to the "spin up" and "spin down" states, respectively.

Let us denote the fractions of protons in the pure spin up and spin down states by n_+ and n_-, respectively. Define a *polarisation* P_y along the Oy quantization axis as the asymmetry of the populations n_+ and n_-:

$$P_y = \frac{n_+ - n_-}{n_+ + n_-}. \tag{2.4}$$

Analogously we could define the polarisations P_x and P_z with respect to the Ox and Oz axes, but we will assume that these two cancel out in the experiment described in this thesis. From these properties we can construct a *polarisation vector* $\tilde{\mathbf{P}}$ defined as follows:

$$\tilde{\mathbf{P}} \equiv [P_x, P_y, P_z] = [0, P, 0]. \tag{2.5}$$

The modulus of $\tilde{\mathbf{P}}$ shall be called the *degree of polarisation*. A single spin 1/2 particle in a pure spin state χ_+ or χ_- is fully polarised, and for such a particle $|\tilde{\mathbf{P}}| = 1$, which follows from definition 2.4 and the fact that single fermions can be found only in one out of two states: χ_+ or χ_-. In reality we deal with the systems containing a large number of particles, and for such systems the degree of polarisation is usually smaller than 1.

By the *polarisation plane* we will refer to a plane spanned by the beam momentum vector $\tilde{\mathbf{p}}_{\mathbf{beam}} \equiv [0, 0, p_z]$ and a polarisation vector $\tilde{\mathbf{P}} = [0, P, 0]$.

2.2 Reference frames

The reference frames along with the angles of production are defined.

We will describe the polarisation observables within the Cartesian coordinates, however in the beginning we have to introduce the certain reference frames that are convenient to this description.

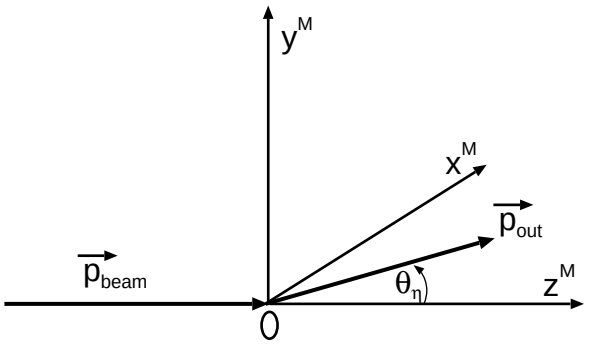

Figure 2.1: Definition of the reference system according to the Madison convention for the description of the polarisation observables.

According to the Madison convention [26] we construct the reference system $(\hat{\mathbf{x}}^{\mathbf{M}}, \hat{\mathbf{y}}^{\mathbf{M}}, \hat{\mathbf{z}}^{\mathbf{M}})$ in the following manner: let a unit vector $\hat{\mathbf{z}}^{\mathbf{M}}$ of the Oz^M-axis be

parallel to the beam momentum direction given by the vector $\tilde{\mathbf{p}}_{\mathbf{beam}}$, and the Oy^M-axis unit vector $\hat{\mathbf{y}}^{\mathbf{M}}$ along the direction of the $\tilde{\mathbf{p}}_{\mathbf{beam}} \times \tilde{\mathbf{p}}_{\mathbf{out}}$ vector, where $\tilde{\mathbf{p}}_{\mathbf{out}}$ is the momentum vector of the η meson. Both $\tilde{\mathbf{p}}_{\mathbf{beam}}$ and $\tilde{\mathbf{p}}_{\mathbf{out}}$ vectors are defined in the centre-of-mass (CM) frame. The $\hat{\mathbf{x}}^{\mathbf{M}}$ – a unit vector along the Ox^M-axis is defined such that the basis $(\hat{\mathbf{x}}^{\mathbf{M}}, \hat{\mathbf{y}}^{\mathbf{M}}, \hat{\mathbf{z}}^{\mathbf{M}})$ forms an orthonormal, right-handed set. Such defined reference frame is sketched in Fig. 2.1. We will refer to this frame as to the *Madison frame*.

The angle θ_η will be called the *polar angle of η production*. This is an angle between $\tilde{\mathbf{p}}_{\mathbf{out}}$ and $\hat{\mathbf{z}}^{\mathbf{M}}$:

$$\cos(\theta_\eta) = \frac{\vec{p}_{out} \cdot \hat{z}^M}{|\vec{p}_{out}|}. \tag{2.6}$$

Now, we introduce the fixed in the centre-of-mass an *accelerator coordinate frame* $(\hat{\mathbf{x}}^{\mathbf{acc}}, \hat{\mathbf{y}}^{\mathbf{acc}}, \hat{\mathbf{z}}^{\mathbf{acc}})$. Define $\hat{\mathbf{z}}^{\mathbf{acc}}$ – a unit vector that is parallel to the beam momentum, a unit vector $\hat{\mathbf{y}}^{\mathbf{acc}}$ perpendicular to the accelerator plane, pointing up, and $\hat{\mathbf{x}}^{\mathbf{acc}}$ which completes the right-handed basis. The accelerator frame is shown in Figure 2.2.a.

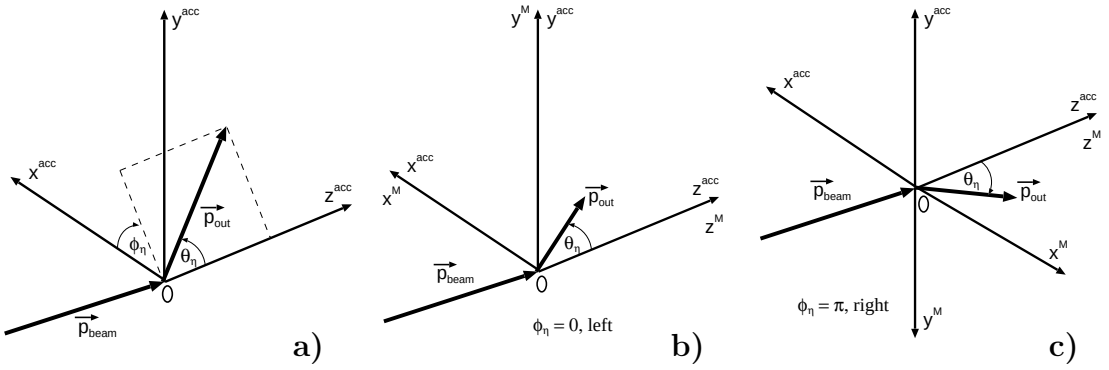

Figure 2.2: (a) Accelerator reference frame. Definition of the scattering to the left (b) and to the right (c) with respect to the polarisation plane.

In the case of the accelerator frame the polar angle of η – θ_η – is the same as in the case of Madison frame, as the Oz^M and Oz^{acc} axes are defined in the same manner.

By the *azimuthal angle of the η meson emission* – ϕ_η – we will understand the angle between the $\hat{\mathbf{x}}^{\mathbf{acc}}$ vector and the projection of $\tilde{\mathbf{p}}_{\mathbf{out}}$ onto the x^{acc}-y^{acc} plane. Both angles are presented in Figure 2.2.a. If the momentum of the η meson is lying in the horizontal plane, i.e. if $\phi_\eta = 0$ or $\phi_\eta = \pi$, then the Oy^M and Oy^{acc} axes (and also Ox^M and Ox^{acc} axes) may be either parallel or antiparallel, depending on whether the η meson is emitted to the left (Fig. 2.2.b) or to the right side (Fig. 2.2.c) in the accelerator system.

It is important to distinguish between the Madison and the accelerator frame. Whereas the accelerator frame is fixed in the centre-of-mass frame, the Madi-

son coordinate system may vary in space from event to event. According to the Madison convention all the physical observables, like for example the beam polarisation vector, should be considered in the Madison frame in order to avoid the ambiguities in the determination of the sign of the analysing power.

2.3 Analysing power

A five-dimensional phase space for the description of the $NN \to NNM$ reactions is defined. The most general formula for the cross section for experiments with polarised beam and target is given, which contains the definition of the analysing power.

For a nuclear reaction with a given initial channel and a three body final state twelve parameters (four-momenta of three particles) have to be known to fully describe the exit channel. Some of these twelve parameters are bound with the relativistic formula:

$$E_i^2 = m_i^2 + (\tilde{\mathbf{p}}_\mathbf{i})^2, \qquad i = 1, 2, 3; \tag{2.7}$$

where E_i, m_i, $\tilde{\mathbf{p}}_\mathbf{i}$ denote the total energy, mass, and the momentum vector of the i-th particle. Equations 2.7 reduce the number of variables to nine, and these variables are dependent on the initial state parameters on the basis of the four-momentum conservation (four additional equations). Therefore, there are eventually five linearly independent variables that need to be measured for each reaction in order to fully describe its kinematics. Here, we follow the references [8, 27] in the choice of these kinematical variables. We will use the invariant masses of the proton-proton system m_{pp} and proton-η system $m_{p\eta}$, the polar θ_η and azimuthal ϕ_η angles of the η momentum in the centre-of-mass (CM) frame, as well as the angle ψ – describing the rotation around the direction established by the momentum of the η meson [27]. These variables are orthogonal and form a basis in the five-dimensional phase space. Let this basis be denoted by $\zeta = \{m_{pp}, m_{p\eta}, \phi_\eta, \theta_\eta, \psi\}$.

Let us denote by

$$\sigma_0(\zeta) \equiv \frac{d^5\sigma_0(\zeta)}{dm_{pp}dm_{p\eta}d\phi_\eta d\theta_\eta d\psi} \tag{2.8}$$

the differential cross section for the reaction in absence of the polarisation of beam and target, and since the internucleon strong interaction is spin-dependent, let us also define

$$\sigma(\zeta, \tilde{\mathbf{P}}, \tilde{\mathbf{Q}}) \equiv \frac{d^5\sigma(\zeta, \tilde{\mathbf{P}}, \tilde{\mathbf{Q}})}{dm_{pp}dm_{p\eta}d\phi_\eta d\theta_\eta d\psi} \tag{2.9}$$

as the differential cross section for the reaction induced by a polarised beam on the polarised target, where $\tilde{\mathbf{P}}$ and $\tilde{\mathbf{Q}}$ are the polarisation vectors of beam and target, respectively. **The beam polarisation vector $\tilde{\mathbf{P}}$ and the target polarisation vector $\tilde{\mathbf{Q}}$ should be referred to in the Madison frame** defined in Section 2.2.

In the most general case, when both $\tilde{\mathbf{P}}$ and $\tilde{\mathbf{Q}}$ are the non-zero vectors, the formula for σ reads:

$$\sigma(\zeta, \tilde{\mathbf{P}}, \tilde{\mathbf{Q}}) = \sigma_0(\zeta)(1 + \sum_{i=1}^{3} P_i A_i(\zeta) + \sum_{i=1}^{3} Q_i A'_i(\zeta) + \sum_{i,j=1}^{3} c_{ij}(\tilde{\mathbf{P}}, \tilde{\mathbf{Q}}) C_{ij}(\zeta)), \quad (2.10)$$

where A_i and A'_i are the beam and target analysing powers, respectively, and $\mathrm{C}_{ij}(\zeta)$ are the spin correlation coefficients. P_i, Q_i and c_{ij} are the expansion coefficients, which depend on the polarisation of beam and target. In our case, where the target is unpolarised, the Q_i and c_{ij} coefficients disappear and we only deal with the A_i vector. Hence Equation 2.10 simplifies to:

$$\sigma(\zeta, \tilde{\mathbf{P}}) = \sigma_0(\zeta)(1 + \sum_{i=1}^{3} P_i A_i(\zeta)). \quad (2.11)$$

For in Equation 2.11 the scalar product of $\tilde{\mathbf{P}}$ and $\tilde{\mathbf{A}}$ is present, in the case of a transversally polarised beam we can rewrite this equation in the following manner:

$$\sigma(\zeta, \tilde{\mathbf{P}}) = \sigma_0(\zeta)(1 + P A_y(m_{pp}, m_{p\eta}, \theta_\eta, \psi) \cos(\phi_\eta)), \quad (2.12)$$

where P is the component of the beam polarisation normal to the incident beam, such that the y-component of polarisation vector expressed in the Madison frame is given by $P_y = P \cos\phi_\eta$.

At this point we would like to mention that the acceptance of the COSY-11 facility allows to register only events scattered near the horizontal plane. In the analysis the azimuthal angle ϕ_η was restricted to values of $\cos\phi_\eta$ ranging between 0.87 and 1. This is depicted in Figure 2.3, where we show the shape of the acceptance of the COSY-11 system for the registration of the events with the η meson production as a function of the azimuthal angle ϕ_η. One can see that the acceptance for events with $\phi_\eta \in [30^\circ, 330^\circ]$ is relatively very small. Moreover, the acceptance is much larger for the cases where the η meson is emitted to the left ($\phi_\eta \approx 0^\circ$) than when it is emitted to the right side of the polarisation plane ($\phi_\eta \approx 180^\circ$). Therefore we decided to consider in our analyses only the events with the η meson production to the left side with respect to the polarisation plane. For such a case $\cos\phi_\eta \approx 1$, and considering that the beam was vertically polarised along the Oy^{acc} axis (polarisation vector given by Equation 2.5) we can rewrite Formula 2.12:

$$\sigma(m_{pp}, m_{p\eta}, \theta_\eta, \psi, P) \approx \sigma_0(m_{pp}, m_{p\eta}, \theta_\eta, \psi)(1 + P A_y(m_{pp}, m_{p\eta}, \theta_\eta, \psi)). \quad (2.13)$$

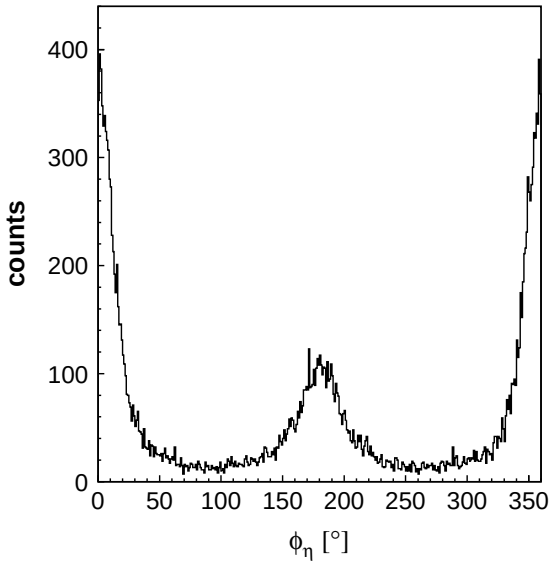

Figure 2.3: Distribution of the $\vec{p}p \to pp\eta$ events which can be registered with the COSY-11 setup as a function of the azimuthal angle of the η meson production in the centre-of-mass system – ϕ_η.

It is worth mentioning that in the case of the $\vec{p}p \to pp\eta$ reaction $A_x(\zeta)$ and $A_y(\zeta)$ are equivalent, because the rotation of the whole system by $\pi/2$ around the Oz axis does not lead to a change of the scattering pattern. Therefore, in case of spin 1/2 particles, there are only two independent polarisation observables: $A_y(\zeta)$ and $A_z(\zeta)$ – the transversal and longitudinal analysing power, the latter being of no significance in the experiments considered here.

From Equation 2.13 it follows that the vector analysing power $A_y(\zeta)$ may be understood as a measure of the relative deviation between the differential cross section for the experiments with and without polarised beam (in the absence of the target polarisation), normalized to the beam polarisation:

$$A_y(\zeta) = \frac{1}{P}\frac{\sigma(\zeta, P) - \sigma_0(\zeta)}{\sigma_0(\zeta)}. \tag{2.14}$$

2.4 Practical formula for the analysing power

The practical recipe for the calculation of the analysing power is derived.

In this section we consider the meson production where the beam consists of vertically polarised protons and the production takes place on an unpolarised proton target.

Naturally, the Madison frame defined in Section 2.2 is not fixed in space, as is schematically shown in Figure 2.4. In the left panel there is depicted a situation when the η meson is produced to the left side with respect to the polarisation plane, whereas the right panel shows the production of the η meson to the right side with respect to the polarisation plane, defined in Section 2.1. While the Madison frame changes depending on $\vec{p_\eta}$ the accelerator frame remains unalterred in space. **One should also notice that the production of the η meson to the left (right) with the polarisation vector of the beam pointing up in the accelerator frame is physically equivalent to the production of the η meson to the right (left) with the beam polarisation vector pointing down.** In both cases the physics, meaning the spin-dependent nuclear interaction, is the same and the two abovementioned cases are equivalent, from which we will make use in due course.

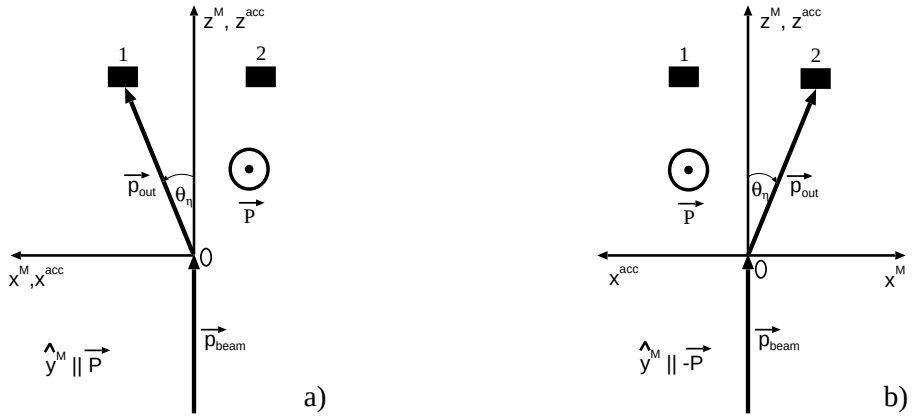

Figure 2.4: Schematic picture of the η meson production to the left (a) and right side (b) with respect to the polarisation plane. The polarisation vector $\tilde{\mathbf{P}}$ is pointing up (out of the paper), which is denoted by $\odot$. Black squares are the virtual η "detectors".

In Figure 2.4 we presented schematically the production of the η meson in the accelerator frame's plane x^{acc}-z^{acc}. The polarisation vector of the beam of protons is pointing up, i.e. along the y^{acc} axis. Denoting by $N(\theta_\eta, \phi_\eta)$[1] the number of the η mesons emitted into the solid angle around θ_η and ϕ_η and by N_1 and N_2 the numbers of the η mesons reaching the virtual η "detectors" 1 and 2 we can write:

$$N_1^{\uparrow} = N^{\uparrow}(\theta_\eta, 0) \equiv N_+^{\uparrow} = \sigma_0(\theta_\eta)(1 + P^{\uparrow} A_y(\theta_\eta))E(\theta_\eta, 0) \int L^{\uparrow} dt, \tag{2.15}$$

and

$$N_2^{\uparrow} = N^{\uparrow}(\theta_\eta, \pi) \equiv N_-^{\uparrow} = \sigma_0(\theta_\eta)(1 - P^{\uparrow} A_y(\theta_\eta))E(\theta_\eta, \pi) \int L^{\uparrow} dt, \tag{2.16}$$

[1] We remind, that the angles θ_η and ϕ_η are referred to the accelerator frame.

where the symbol "↑" stands for the spin up orientation, $\int L^{\uparrow} dt$ is the luminosity during the measurement with spin up, integrated over the whole time of the measurement, $E(\theta_\eta, \phi_\eta)$ is the efficiency of the detection setup for "registering" the η mesons produced into the solid angle around θ_η and ϕ_η, $\sigma_0(\theta_\eta)$ is the cross section for the η meson production with absence of the beam polarisation, $P^{\uparrow}$ is the beam polarisation during the spin up cycles and $A_y(\theta_\eta)$ is the analysing power for the η production averaged over m_{pp}, $m_{p\eta}$ and ψ. The "+" sign denotes the production with the polarisation vector along the Oy^M-axis (according to the Madison convention P_y is positive in this case), and the "−" sign is for the production with the polarisation vector antiparallel to the Oy^M-axis (negative P_y).

Now, if we flipped the polarisation vector i.e. if we made it pointing down (into the paper in Figure 2.4) we would get:

$$N_1^{\downarrow} = N^{\downarrow}(\theta_\eta, 0) \equiv N_-^{\downarrow} = \sigma_0(\theta_\eta)(1 - P^{\downarrow} A_y(\theta_\eta))E(\theta_\eta, 0) \int L^{\downarrow} dt, \tag{2.17}$$

$$N_2^{\downarrow} = N^{\downarrow}(\theta_\eta, \pi) \equiv N_+^{\downarrow} = \sigma_0(\theta_\eta)(1 + P^{\downarrow} A_y(\theta_\eta))E(\theta_\eta, \pi) \int L^{\downarrow} dt, \tag{2.18}$$

where the quantities with arrows pointing down refer to the respective quantities from Equations 2.15 and 2.16, but for the cycles with spin down mode.

From Equations 2.15 and 2.16 we obtain:

$$A_y(\theta_\eta) = \frac{1}{P^{\uparrow}} \frac{N_+^{\uparrow}/E(\theta_\eta, 0) - N_-^{\uparrow}/E(\theta_\eta, \pi)}{N_+^{\uparrow}/E(\theta_\eta, 0) + N_-^{\uparrow}/E(\theta_\eta, \pi)}. \tag{2.19}$$

The same is valid for Equations 2.17 and 2.18, but we have to change ↑ into ↓ in Equation 2.19. Note, that Equation 2.19 is independent of the integrated luminosity. Equation 2.19 shows that the analysing power $A_y(\theta_\eta)$ may be calculated from the production with only one spin orientation (spin up or spin down), if both scatterings – into left and right side in the accelerator plane – can be measured. To some extend it may be realised by the COSY-11 detector. However, for the COSY-11 detector setup $E(\theta_\eta, 0) \gg E(\theta_\eta, \pi)$ (see Figure 2.3, where between $\phi_\eta \in [330^0, 30^0]$ there are much more events than for $\phi_\eta \in [150^0, 210^0]$), and therefore in practice we have to perform the measurement with two beam spin orientations.

Assuming that the degree of polarisation during the cycles with spin down is equal to the degree of polarisation for cycles with spin up, which is the case within the 2% of accuracy[2] as has been shown in the previous measurements by means of the EDDA polarimeter [28], we may introduce the average degree of polarisation P:

$$P \approx P^{\uparrow} \approx P^{\downarrow} \approx \frac{P^{\uparrow} + P^{\downarrow}}{2}. \tag{2.20}$$

[2]See also Section 5.4.2.

Assuming that the degrees of polarisation for spin up and down are equal, the asymmetry between $N_+^{\uparrow}$ and $N_-^{\downarrow}$ may be used as a measure of the spin-dependent η meson production. Dividing Equation 2.15 by Equation 2.17, and replacing $P^{\uparrow}$ and $P^{\downarrow}$ by P yields to:

$$\frac{N_+^{\uparrow}(\theta_\eta)}{N_-^{\downarrow}(\theta_\eta)} = \frac{\int L_{\uparrow} dt}{\int L_{\downarrow} dt} \; \frac{1 + P A_y(\theta_\eta)}{1 - P A_y(\theta_\eta)}. \tag{2.21}$$

Introducing the relative luminosity defined as:

$$L_{rel} \equiv \frac{\int L_{\uparrow} dt}{\int L_{\downarrow} dt}, \tag{2.22}$$

and solving Equation 2.21 for A_y we obtain:

$$A_y(\theta_\eta) = \frac{1}{P} \frac{N_+^{\uparrow}(\theta_\eta) - L_{rel} N_-^{\downarrow}(\theta_\eta)}{N_+^{\uparrow}(\theta_\eta) + L_{rel} N_-^{\downarrow}(\theta_\eta)}, \tag{2.23}$$

a formula which is independent of the efficiency of the detection setup. In what follows, Formula 2.23 will be used for the calculation of the analysing power.

Chapter 3

Theory

3.1 Theoretical models of the η meson production in nucleon-nucleon collisions

Some phenomenological models of the η meson production in the $pp \to pp\eta$ reaction are shortly reviewed. Conclusions from the analysis of the available physical observables along with the predictions for the analysing power are pointed out.

Despite the fact that the discovery of the η meson took place over forty years ago [1], its production mechanism still remains an open question [29, 30]. After early measurements of the total cross sections for the $pp \to pp\eta$ reaction in bubble chamber experiments [31–38], only recently there appeared high-statistics, close-to-threshold data from storage rings, giving opportunity to investigate more accurately the structure, properties, production mechanism as well as the interaction of the η meson with hadronic matter. The close-to-threshold total cross section measurements for the $pp \to pp\eta$ reaction [2–10], investigations on the differential cross sections for this reaction [8, 12, 39–41] and recently performed measurements of the analysing power for the $\vec{p}p \to pp\eta$ reaction [15, 16] made the theoretical analysis possible aiming in understanding the production process.

3.1.1 Conclusions from the total cross section measurements

From the total cross section measurements for the $pp \to pp\eta$ reaction it is inferred that amongst several possible scenarios the resonant current is the dominant one in the process of the η meson production in proton-proton collisions.

The majority of the theoretical models tries to elucidate the production of the η meson within the framework of a one-boson-exchange formalism [11, 14, 42–50],

where two interacting nucleons on the basis of a momentary energy violation exchange a virtual meson, which subsequently, under the interaction with nucleons turns into the η meson. Some of the possible mechanisms which may lead to the η meson creation in nucleon-nucleon collisions are pointed out in Figure 3.1 and will be described in the further part of this section. What is characteristic to this kind of approach to the meson production is that the models do not enter into the quark-gluonic structure of the meson and nucleons, but rather introduce the phenomenological parameters like for example the coupling constants for different channels, the scattering lengths, the effective ranges, and cut-offs.

On the other hand there are also trials to explain the η meson production mechanism on the basis of instanton models for QCD vacuum [51, 52]. In these QCD-oriented approaches the calculations are on the very elementary level, where the effective degrees of freedom are not mesons and baryons like it was in the case of the one boson exchange models but rather the constituent quarks and gluons. These models however are temporarily in the early stage of development, and so we will deal here with the phenomenological meson-exchange models solely.

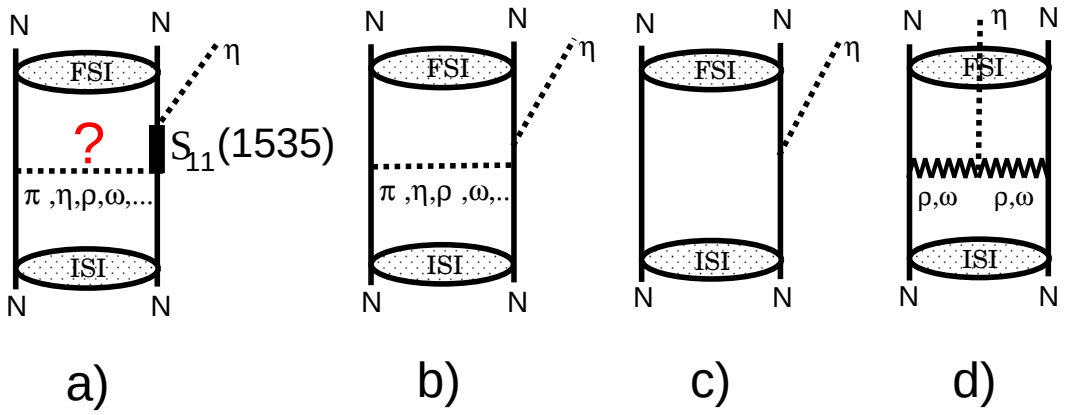

Figure 3.1: Possible mechanisms of the η meson production in nucleon-nucleon collisions: (a) resonant currents, (b) nucleon currents, (c) direct production, (d) mesonic currents.

In Figure 3.1 there are depicted some of the possible scenarios for the η meson production in the nucleon-nucleon collisions. Figure 3.1.a shows the resonant current, where the η meson is produced in a two-step process: in the first stage the exchange of one of the pseudoscalar or vector mesons excites the nucleon to the $S_{11}(1535)$ resonance and subsequently in the second step this resonance decays into a proton-η pair. Apart from the $S_{11}(1535)$ resonance, also the contributions from the other possible resonances are considered. For example in the model reported in the reference [11] also $P_{11}(1440)$ and $D_{13}(1520)$ states, excited by the exchange of π, η, ρ, and ω mesons have been included, however, the contribution from the

$S_{11}(1535)$ excitation by the π and η mesons has been found to be dominant. The $S_{11}(1535)$ resonance seems to play an important role as an intermediate state since it has a large width, covering the threshold energy for the $pp \to pp\eta$ reaction, and couples strongly to the proton-η system with the branching ratio corresponding to 30–55% [53]. The mechanism of the excitation of the colliding proton to the $S_{11}(1535)$ resonance remains an open issue. The authors of [14, 44, 47] have found the ρ meson exchange to play the dominant role in this excitation. It has been stated that the ρ meson exchange is particularly important to explain the shape of the angular distribution of the $pp \to pp\eta$ reaction. On the other hand, the authors of article [11] showed that the excitation function of the total cross section for the $pp \to pp\eta$ reaction as well as the angular distribution of the emitted η meson can be equally well described by the resonant mechanism, where the $S_{11}(1535)$ is excited by the π meson. This is presented in Figures 3.2.a and 3.2.b showing the comparison of the theoretical description of the excitation function for the $pp \to pp\eta$ reaction: in Figure 3.2.a the pseudoscalar meson exchange model has been used, while in Figure 3.2.b there are presented predictions of the vector meson dominance model.

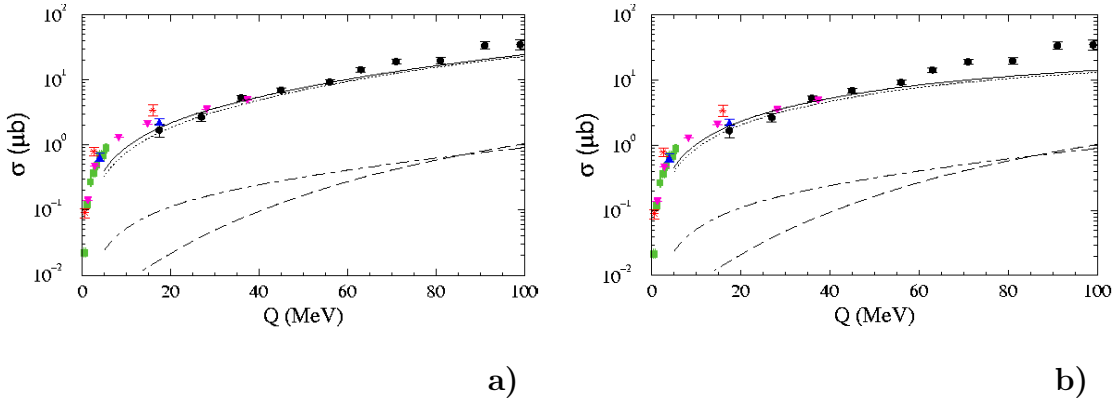

Figure 3.2: Description of the close-to-threshold total cross section data for the $pp \to pp\eta$ reaction by means of the pseudoscalar meson exchange model (a) and vector meson exchange model (b). Data are from references [3–7]. The dotted curves are the resonance current contributions, the dashed lines represent the nucleonic current contribution, while the dashed-dotted curves are the mesonic current contribution. The solid lines show the total contribution. The figure is adapted from [11].

As can be seen from these figures, both models give equally well descriptions of the experimental data. The underestimation of the data by the models in the very close-to-threshold region results mainly from neglecting the η-proton final state interaction (FSI). Proton-proton FSI has been accounted for in both calculations. Also at the higher excess energies (Q>60 MeV) models underestimate the existing data, which may be due to the higher partial waves which were not taken into account. The main conclusion here is that the resonant current (dotted curves),

i.e. the mechanism shown in Figure 3.1.a, plays the dominant role in the η meson creation. However, as far as only the excitation function of the total cross section is being considered, we are not able to state about the exchanged mesons in the process of the η meson production in proton-proton collisions.
Contribution of the other process that is depicted in Figure 3.2 is the nucleonic current (dashed curves) which we deal with when one of the nucleons emits a meson, which subsequently mixes its quark-gluonic structure with the structure of the other nucleon, and in the final state we again finish with a proton along with the η meson (see diagram 3.1.b). Naturally, the final state proton may have different properties – momentum and/or angular momentum, etc. – than the initial state proton.
The last process taken into account in the abovementioned models is the mesonic current (dash-dotted curves, schematically presented in diagram 3.1.d), when the η meson is being produced via the exchange and fusion of two mesons emitted instantly from interacting nucleons.

As has been mentioned previously, in this model the contribution of the two latter currents is rather negligible with comparison to the contribution of the resonant current (see Figure 3.2).

Last possible scenario presented in Figure 3.1.c – the direct η production – although not taken into account in the calculations of [11] has been considered in the model of reference [50]. It has been found that the contribution from this process is of minor importance, being a one order of magnitude weaker than the mesonic current contribution.

3.1.2 Differential cross sections

Results of the measurements of the differential cross section for the $pp \to pp\eta$ reaction are reported.

Figure 3.3 shows one-dimensional differential spectra of the cross sections for the $pp \to pp\eta$ process at Q = 36 MeV, namely the angular distributions of the emitted η meson in the centre-of-mass (CM) frame. Left panel presents the theoretical predictions of the pseudoscalar meson exchange model confronted with the data. The description of the curves shown in this figure is the same as that of Figure 3.2. The data have the tendency to bend down in the range of extreme values of the $\cos(\theta)$. On the other hand, the contribution from the resonant current of the pseudoscalar meson exchange model (see Fig. 3.3.a) has the opposite tendency, i.e. it bends upwards. However, the interference with the remaining two currents – nucleonic and mesonic – bends the overall contribution downwards. The behavior of the experimental data, as can be seen in Fig. 3.3.a, is not quite well reproduced by the resultant interference.

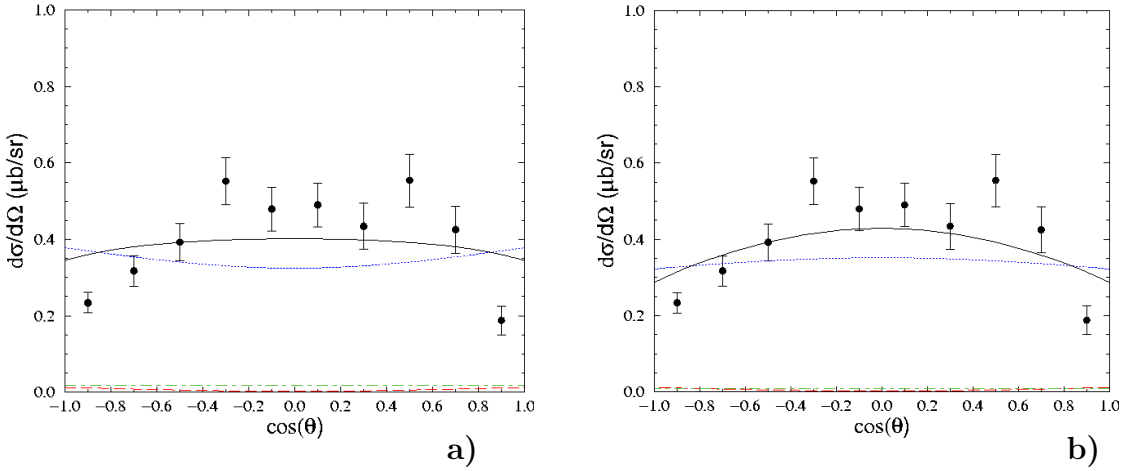

Figure 3.3: Description of the angular distribution of the produced η meson in the CM system in the $pp \rightarrow pp\eta$ reaction at Q = 36 MeV within the pseudoscalar meson exchange model (a) and vector meson exchange model (b). Data are from reference [39]. The meaning of the curves is the same as in Figure 3.2. The figure is adapted from [11].

In the case when the main contribution to the excitation of the S_{11} resonance originates from the ρ meson exchange (Figure 3.3.b) the experimental data are slightly better reproduced, especially at the edges of the $\cos(\theta)$ range. This might indicate that the vector meson exchange mechanism was better in explaining the shape of the angular distributions for the $pp \rightarrow pp\eta$ process.

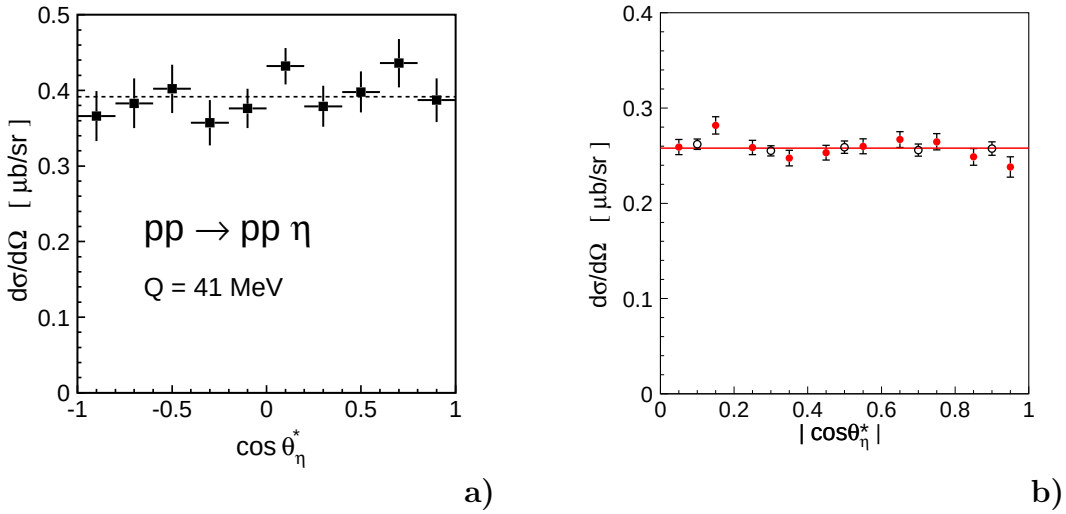

Figure 3.4: Angular distribution for the η meson emission in the CM system for the $pp \rightarrow pp\eta$ reaction (a) as measured by the COSY/TOF collaboration [12] at Q = 41 MeV, (b) as obtained by the COSY-11 collaboration [8] at Q = 15.5 MeV (full circles) and by the COSY/TOF collaboration [12] at Q = 15 MeV (open circles). The solid line is the fit of the Legendre polynomials. Figures are adapted from [8].

Here, a few words of explanation are required. At the time when the work of [11] has been released the only measurements of the differential cross section for the $pp \to pp\eta$ reaction available were the early results of H. Calen et al. [39]. Unfortunately, the detector used in these measurements – the PROMICE/WASA detector [39] – had relatively poor angular acceptance in the side-range of θ angle (i.e. the $\cos(\theta)$ around 0 value). Later on, the measurements have been repeated by means of the COSY/TOF experimental setup [12] at the excess energy of Q = 41 MeV and show, within the error bars, the isotropic behavior over the whole range of $\cos\theta$ – see Figure 3.4.a.

Therefore, as can be seen from comparison of Figures 3.3 and 3.4.a, the theoretical predictions suitable for description of the flat differential cross sections are either those of the total contribution of the pseudoscalar meson exchange model or those of the resonance current contribution of the vector exchange model.

The newer data on the angular distribution for the $pp \to pp\eta$ reaction at Q = 15.5 MeV [8] and Q = 15 MeV [12], both presented in Figure 3.4.b, show the flat distribution of the η meson emission angle in the CM frame. The discussed angular distributions suggest that in the close-to-threshold region, i.e. up to the excess energy of about Q = 50 MeV, the η meson is predominantly produced in the s wave and the higher partial waves are rather suppressed.

3.1.3 Isospin dependence of the hadronic η meson production

It is shown that the measurements of the isospin dependence of the total cross section for the $NN \to NN\eta$ reaction help to diminish the number of possible mesons in the excitation of the $S_{11}(1535)$ resonance.

The conclusion from the analysis of the results on the total and differential cross section for the $pp \to pp\eta$ reaction presented in Sections 3.1.1 and 3.1.2 is that the production of the η meson in proton-proton collisions proceeds predominantly via the excitation of one of the colliding protons to the resonant state $S_{11}(1535)$. However, the relative contributions from the π, η, ρ, and ω meson exchanges still remain to be determined.

For the $NN \to NN\eta$ reaction there are two independent total cross sections: σ_0 and σ_1, corresponding to the total isospin of two initial state nucleons I = 0 and I = 1, respectively. The $pp \to pp\eta$ reaction corresponds to the pure σ_1 cross section. The $pn \to pn\eta$ reaction is a mixture of I = 0 and I = 1 initial states, as the proton's and neutron's isospins may sum up to the total isospin 0 or 1. The theoretical considerations involving the Clebsch-Gordan coefficients yield:

$$\sigma(pn \to pn\eta) = \frac{1}{2}(\sigma_0 + \sigma_1). \tag{3.1}$$

The total cross section for the quasi-free $pn \to pn\eta$ reaction has been de-

termined in the excess energy range between Q = 16 and 109 MeV by the WASA/PROMICE collaboration [13]. The ratio $R_\eta = \sigma(pn \to pn\eta)/\sigma(pp \to pp\eta)$ has been found to equal about 6.5 in the quoted excess energy range, as depicted in Figure 3.5.

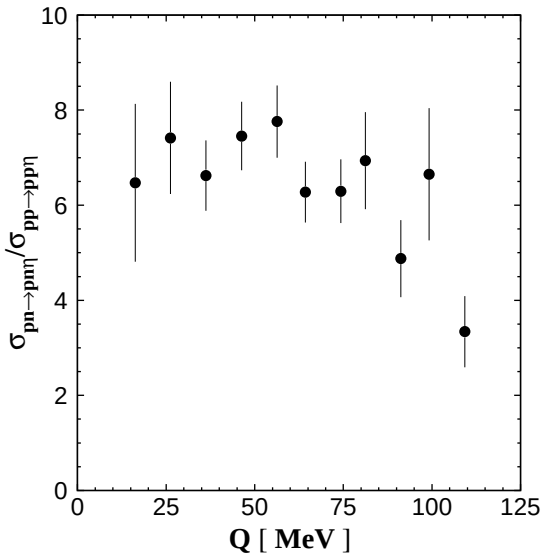

Figure 3.5: The ratio $R_\eta = \sigma(pn \to pn\eta)/\sigma(pp \to pp\eta)$ of the total cross section for the quasi-free $pn \to pn\eta$ to the total cross section for the $pp \to pp\eta$ reaction as the function of the excess energy. The original data are from reference [13].

From relation 3.1, the fact that $\sigma(pp \to pp\eta) = \sigma_1$, and the definition of the ratio $R_\eta = \sigma(pn \to pn\eta)/\sigma(pp \to pp\eta)$ we get:

$$\sigma_0 = (2R_\eta - 1)\sigma_1. \tag{3.2}$$

Therefore, the measured ratio $R_\eta = 6.5$ implies that the production of the η meson with the total isospin I = 0 exceeds the production with the isospin I = 1 by a factor of 12.

Using the short range approximation, where the S wave cross sections are given by [13, 54]

$$\sigma(pp \to pp\eta) = \sigma_1(pn \to pn\eta) = C|t_\pi + t_\eta + t_\rho + t_\omega|^2|\psi_{I=1}(0)|^2, \tag{3.3}$$

and

$$\sigma_0(pn \to pn\eta) = C|-3t_\pi + t_\eta + 3t_\rho - t_\omega|^2|\psi_{I=0}(0)|^2, \tag{3.4}$$

where t_i stands for the strength of the different meson exchanges. The relative phases of the meson exchanges were taken to be real. The factor C, which includes

the phase space and particles interaction, was assumed to be the same for both isospins. The squared ratio between I = 0 and I = 1 wave functions $\psi(r)$ at the zero distance between the particles was calculated to be approximately constant and equals 0.8 [54]. Therefore the ratio

$$\frac{|-3t_\pi + t_\eta + 3t_\rho - t_\omega|^2}{|t_\pi + t_\eta + t_\rho + t_\omega|^2} \approx 15, \tag{3.5}$$

which is a relatively large value, suggesting the dominance of the isovector meson exchange (π and ρ) over the isoscalar meson exchange for the η meson hadronic production.

3.2 How do the analysing power measurements enable a distinction between the possible scenarios?

The hitherto performed measurements of the analysing power for the $\vec{p}p \to pp\eta$ reaction are quoted. The available model predictions for the A_y at different excess energies as calculated based on different meson exchange models are shown. It is pointed out how the measurements of the analysing power enable to infer about the production mechanism of the η meson in hadronic collisions.

What has been described previously implicates that more limitations have to be added to the models in order to extract the information which meson – pseudoscalar π meson or vector ρ meson – plays the most important role in the excitation of the intermediating $S_{11}(1535)$ resonance.

One solution would be verification of the polarisation observables – like the analysing power or spin correlation functions – given by different models. At present there exist two models that predict the energy dependence of the beam analysing power for the $\vec{p}p \to pp\eta$ reaction [11,14]. There are significant differences between the predictions based on these models visible in Figure 3.6: e.g. the relative sign and the magnitude of the analysing power. Measurements of this observable might therefore serve in establishing the valid mechanism of the η meson production.

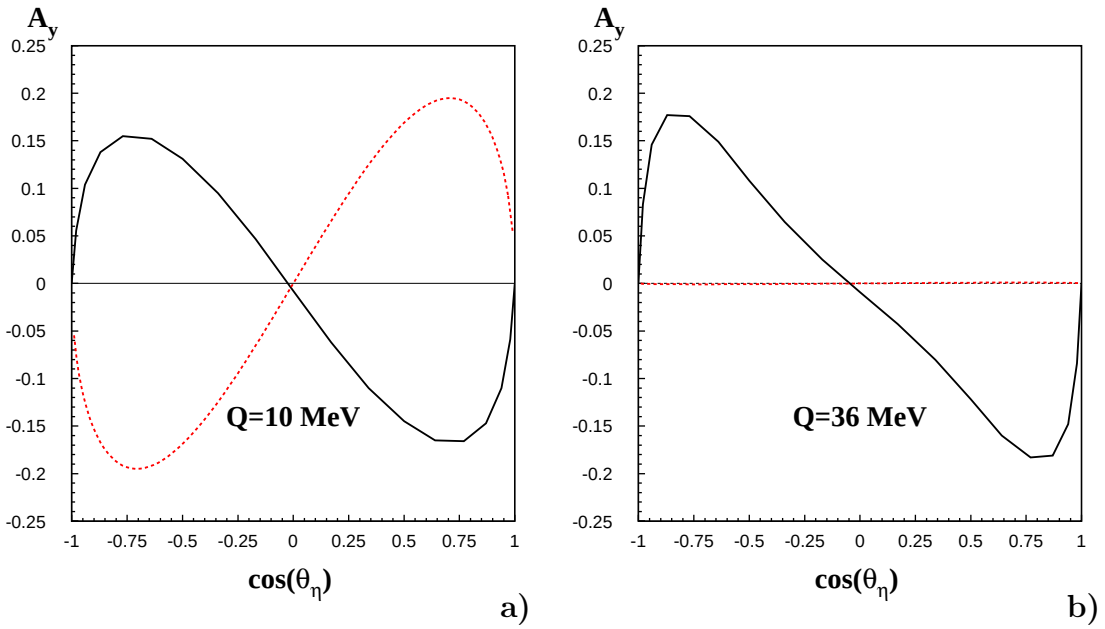

Figure 3.6: Predictions of the analysing power for the $\vec{p}p \to pp\eta$ reaction as a function of the cosine of centre-of-mass polar angle of η – $\cos(\theta_\eta)$ – at Q = 10 MeV (a) and Q = 36 MeV (b). Full lines are the predictions of the pseudoscalar meson exchange model [11] whereas the dotted lines represent the results of the calculations based on the vector meson exchange [14].

According to the model predictions of reference [14] the analysing power for the $\vec{p}p \to pp\eta$ reaction in the close-to-threshold region should have the following form:

$$A_y(Q, \theta_\eta) = A_y^{max}(Q)\sin(2\theta_\eta), \tag{3.6}$$

where θ_η is the angle of the η meson emission in the centre-of-mass frame. Equation 3.6 has been obtained under the assumption of only ρ meson exchange in the excitation mechanism of the $S_{11}(1535)$ resonance. The amplitude A_y^{max} in reference [14] is parameterized by means of the dimensionless parameter η, namely:

$$A_y^{max} = -1.5[(-3 \pm 0.5)\eta^2 + (16 \pm 4)\eta^4], \tag{3.7}$$

where

$$\eta = \sqrt{\frac{4M}{2mM + m^2}Q}. \tag{3.8}$$

In Equation 3.8 $m = 547.75 \pm 0.12$ MeV [53] denotes the η meson mass, while M = 938.27203 ± 0.00008 MeV is the proton mass [53]. The shape in the form of $\sin(2\theta_\eta)$ was obtained from the parameterization of the $\gamma p \to p\eta$ differential cross sections [55,56] with the Legendre polynomials, and by the assumption that vector-meson-induced reaction amplitudes may be obtained from the amplitudes

for photoproduction, using the proper Jacobians [14]. The predicted values for A_y^{max} as function of the excess energy Q are depicted in Figure 3.7.

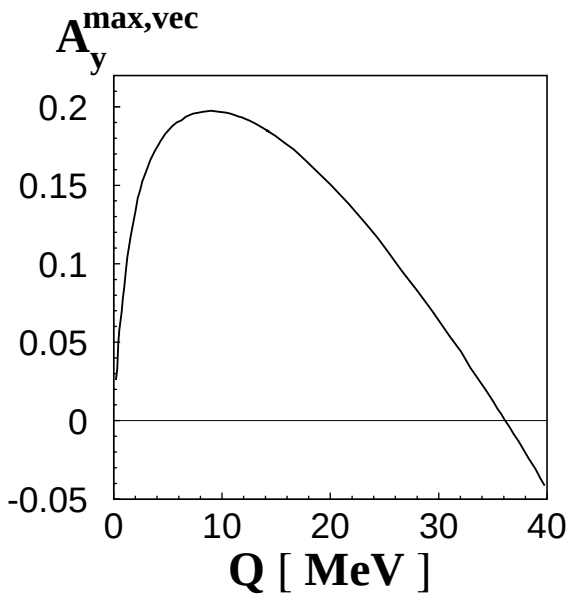

Figure 3.7: Predictions for the value of A_y^{max} for the $\vec{p}p \to pp\eta$ reaction as a function of excess energy. In the estimations, the vector meson exchange of reference [14] has been applied.

The characteristic feature here is that A_y^{max} is peaked at Q = 10 MeV, where COSY-11 has the largest acceptance. This feature has been one of the main motivations to perform the measurement of the analysing power at this particular excess energy value. At Q of about 36 MeV $A_y^{max} \approx 0$, and we also decided to investigate this region of the excess energy. Note that at this value of excess energy the A_y^{max} changes its sign and becomes negative for the higher excess energies in the close-to-threshold region.

The model independent considerations of the spin observables can be found in reference [57]. The details of the pseudoscalar model assumptions and its prediction concerning the analysing power for the $\vec{p}p \to pp\eta$ reaction has been described in [11, 58].

The first test measurement of the analysing power for the $\vec{p}p \to pp\eta$ reaction at the excess energy of Q = 40 MeV has been performed by the COSY-11 collaboration in the year 2001. The method of the analysis and the results have been reported in [16, 17] and are depicted in Figure 3.8.

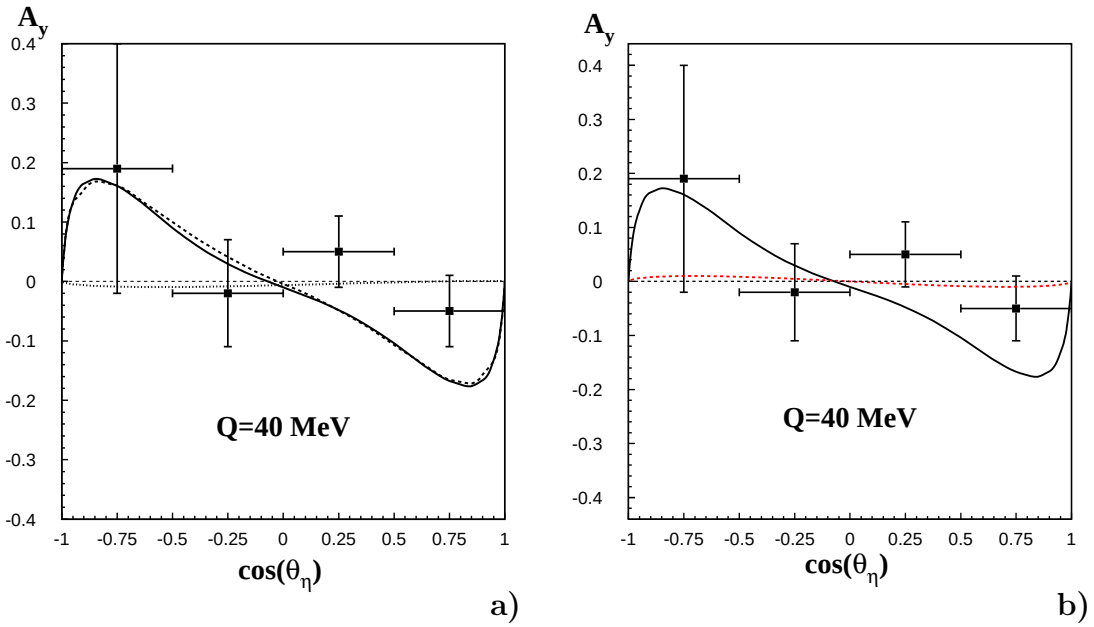

Figure 3.8: (a) Analysing power for the $\vec{p}p \to pp\eta$ reaction at Q = 40 MeV. Meaning of the curves is explained in the text. (b) Comparison of experimental data of the analysing power for the $\vec{p}p \to pp\eta$ reaction at Q = 40 MeV with the predictions of pseudoscalar (solid line) and vector meson exchange models (dashed line).

Figure 3.8.a shows the comparison of the experimental results with the theoretical predictions [59] of the individual partial waves contributions in the η meson production. Production of the η meson in the s wave solely would force analysing power to vanish [59], and therefore any non-zero result must involve the production of the η meson in higher partial wave. The dotted curve corresponds to the case, where the η meson is created in the $s + p$ waves, while the dashed curve represents the η meson production in the $s + p + d$ wave. The solid line is the full result of the model, where also the higher partial waves of the η meson production are taken into account. Unfortunately the accuracy of the data does not allow to state firmly whether the η meson is produced in the s or $s + p$ wave and therefore to cope with this problem further investigations were required. One should also mention that the data of [16] need to be reanalyzed in order to get rid of the occasional error, however as has been checked in the analysis described in this dissertation, the corrected results should not differ from the results presented in Figure 3.8 of more than one standard deviation.

Figure 3.8.b shows the comparison of the data with theoretical predictions of the pseudoscalar meson exchange model (solid line) and vector meson exchange model (dashed curve). Both model predictions lie within around 2σ distance from experimental data, and therefore at the level of accuracy obtained during the first measurement of the analysing power we were not able to distinguish between two

different hypotheses of the η production. Further investigations were necessary and constitute the subject of this dissertation.

Chapter 4

Experiment

The laboratory aparatus which enabled the experiments presented in this dissertation comprises the storage ring COSY, which provides the accelerated polarised proton beams, and the detection setup COSY-11 used to register and identify the products of reaction. Both facilities will be described in the following sections.

The COSY-11 detection setup has been described in details in many previous publications, therefore here we will present it only very briefly emphasizing the detectors relevant for measurements described in this thesis and aspects connected with the beam polarisation.

4.1 Cooler Synchrotron COSY

4.1.1 General properties

The rough description of the cooler synchrotron COSY is given.

The cooler synchrotron COSY [21, 22] – a storage ring designed to accelerate the polarised and unpolarised beams of protons and deuterons – is operated by the Institute of Nuclear Physics (IKP) in the Research Center Jülich in Germany. This device, sketched in Figure 4.1, consists of the ion source that provides the polarised or unpolarised ions of H^- and D^- to be further preaccelerated in the low energy cyclotron JULIC, which accelerates these beams up to the energies of 45 MeV for H^- ions and 75 MeV for D^- [60]. After the preacceleration, the beam is extracted and guided through the 100 m long beamline to be injected into the storage ring COSY, that further accelerates the beams to the demanded momenta in the range from 0.3 GeV/c up to 3.7 GeV/c.

The synchrotron consist of two arcs, containing in total 24 dipole magnets, and two straight sections, each of about 40 m length. The total length of the COSY ring is 183.4 m.

The synchrotron COSY is equipped with two systems of beam cooling: the electron and stochastic cooling [70]. In order to increase the intensity of the beams

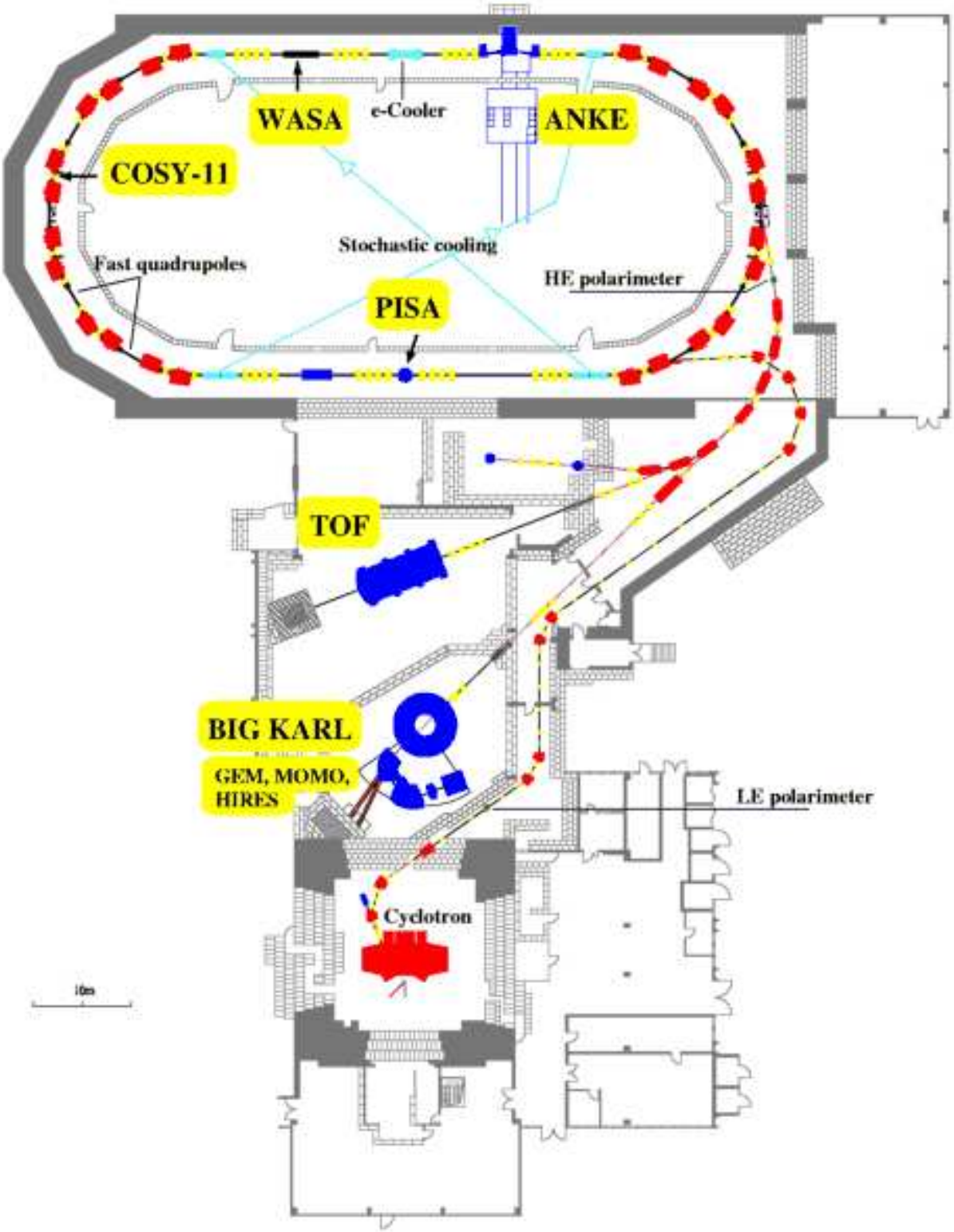

Figure 4.1: COoler SYnchrotron COSY - the floorplan. Several internal (ANKE [61], COSY-11 [62], PISA [63]) as well as external experiments (GEM [64], HIRES [65], MOMO [66], TOF [67, 68]) are making use of the COSY beams. Recently the 4π detection setup WASA [69] has been installed.

of polarised protons the electron cooler is being used. Using the electron cooler and the stacking technique it was possible to store 10^{10} polarised protons during the runs concerned in this thesis. The stochastic cooling for COSY [71,72] is designed to reduce the emmitance of the proton beams in the momentum range between 1.5 and 3.7 GeV/c. The system consists of one pickup tank of 4 m length and a kicker of 2 m length for each the vertical and horizontal planes. The stochastic cooling is generally used for internal target experiments in order to achieve the equilibrium conditions between target heating and stochastic cooling. For more details on the working principle of the COSY electron and stochastic cooler the reader is referred to [70, 72].

4.1.2 Production of the polarised proton beam

The source of the polarised proton beam is described along with the method of polarised beam production at the cooler synchrotron COSY.

The source of the polarised proton beam [73] is of a Colliding-Beam Source type, that provides the polarised $\vec{H}^-$ ions in a direct charge-exchange process of colliding beams:

$$\vec{H}^0 + Cs^0 \rightarrow \vec{H}^- + Cs^+. \tag{4.1}$$

Here, the neutral nuclear polarised beam of hydrogen produced in the atomic-beam source meets a fast neutral Cs^0 beam. The cross section for the process 4.1 is large because the binding energy of the electron in Cs (3.9 eV) is close to the binding energy of the electron in hydrogen's 2S state (3.4 eV). Additionally the $\vec{H}^0$ atoms are rather slow, which increases the probability of the charge-exchange reaction. For injection the nuclear polarised anions are used rather than H^+, as it has been experimentally proven that stripping off the electrons from H^- during injection into the COSY is about an order of magnitude more efficient than stacking injection of protons using a bunched beam [73].

The polarised ion source, presented in Figure 4.2, consists of dissociator, two groups of sextupole magnets, the radio frequency transitions, the solenoid magnet, cesium ionizer, colliding zone, the 90^0 deflector, and a Wienfilter. In the dissociator the H_2 molecules are dissociated into atoms, which subsequently through the cooled nozzle reach the sextupole magnets region. The first sextupole magnet produces the electron state polarisation of the atoms, and subsequently atoms with the electron spin state $m_J = -1/2$ are defocused and only atoms with m_J=+1/2 survive. The second sextupole magnet acts as the lense to focus the hydrogen atoms into the radio frequency transition units, which produce the nuclear polarisation. Afterwards the polarised $\vec{H}^0$ atoms collide with a cesium beam moving in the opposite direction. In the charge-exchange region where the reactions 4.1 occur the nuclear polarisation of hydrogen is preserved by the strong longitudinal magnetic field at the order of 1.7 kG. For this value of magnetic field the polarisa-

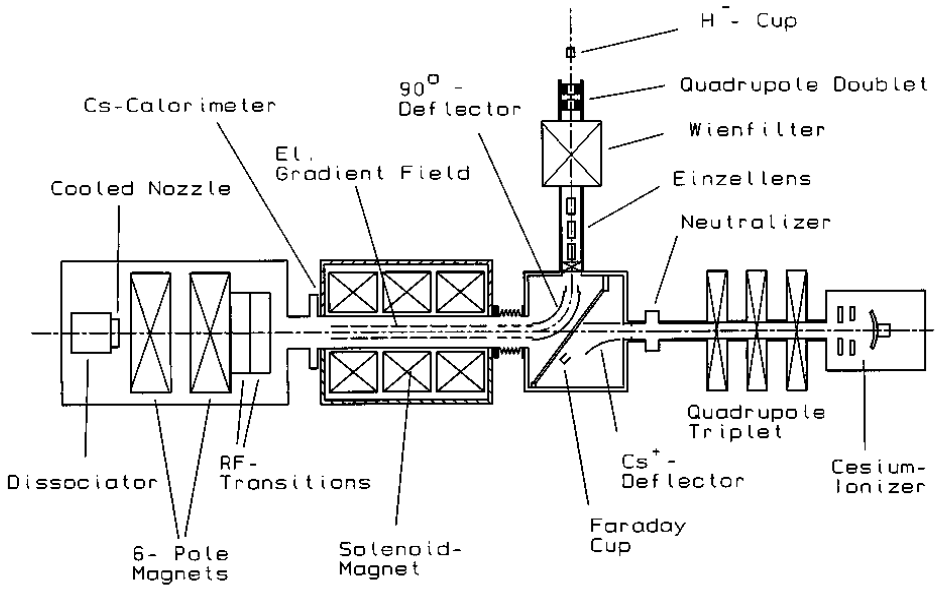

Figure 4.2: The polarised ion source for COSY. Figure is adapted from [73].

tion of protons at the level of circa 95% can be expected [73]. The polarised $\vec{H}^-$ anions are subsequently deflected by 90° in the magnetic deflector and guided into the extraction system, passing on the way the Wienfilter, which may be rotated around the beam axis, and therefore can select the required spin orientation of the $\vec{H}^-$ ions, and also separate the anions from the electrons and other background particles.

Subsequently the $\vec{H}^-$ beam is injected into the cyclotron JULIC at the energy of 4.5 keV. The cyclotron preaccelerates them up to energies of 45 MeV. After that, the beam of $\vec{H}^-$ anions is guided through the beam lines and reaches the stripping injector [74], where the $\vec{H}^-$ anions are stripped off two electrons and furthermore injected into the COSY-Ring as polarised protons with the selected polarisation orientation.

With this method the intensity of circa 10^{10} stored polarised protons with a degree of polarisation over 65% have been obtained [75] during the experiments reported in this work[1].

4.1.3 Acceleration of the polarised proton beam

Acceleration of the polarised proton beams is described. Superimposed are the methods of overcoming the intrinsic and imperfection resonances. The table of all possible

[1]Nowadays it is possible to achieve over 90% polarisation for the internal experiments and circa 80% for the external ones [76].

depolarising resonances at the COSY ring is presented.

The acceleration of the polarised beams is challenging due to the number of depolarising resonances that occur during this process, depending on the demanded momentum of the beam.

The polarisation vector of the beam of protons stored in the ring precesses around the magnetic fields encountered along the particles' orbit[2]. In the ideal ring, where the dipole magnetic fields are vertical, the number of spin precessions during one turn (so called spin tune) is given by [77]:

$$\nu = \gamma G, \tag{4.2}$$

where γ is the Lorentz factor, and G denotes the gyromagnetic anomaly – for protons $G = 1.79285$. Depolarising spin resonances arise when the frequency of the precession of the polarisation vector is such that upon each revolution the difference between the phases of the polarisation vector and the depolarising magnetic field vector is the same at the point where these two meet. At the COSY ring there are two main types of depolarising resonances [75]:

- **imperfection resonances**, caused by magnetic field errors, arising if the magnets are slightly misaligned or if there are vertical orbit distortions. These resonances occur at the beam momenta for which γG has an integer value;
- **intrinsic resonances**, caused by the radial fields due to vertical focusing of the beam, occurring when $\gamma G \pm (Q_y - 2)$ equals an integer, where Q_y is the betatron vertical tune, i.e. the number of vertical oscillations of the beam per one revolution.

The resonances connected with the horizontal betatron tune Q_x, occurring when $\gamma G \pm (Q_x - 2)$ equals an integer are not important at COSY[3] for the vertically polarised beams, because the horizontal betatron motion is driven by the vertical magnetic fields of the quadrupoles. Also we will not consider here the induced resonances, arising due to the longitudinal oscillating magnetic fields.

Table 4.1 [78] shows the chart of all depolarising resonances and the corresponding proton beam momenta p_{beam} in the momentum range of COSY. Resonance strengths ϵ_r and ratios of preserved polarisation P_f/P_i are shown. In the simulations [78] an energy gain per turn equal to 0.7 keV has been assumed. Number of intrinsic resonances depends on the superperiodicity S, the parameter which describes the machine setting of the quadrupole magnets. If all magnets are operated with the same quadrupole settings, the superperiodicity S = 6 and only one intrinsic resonance occurs. However, this setting does not allow to accelerate the

[2] In the case when the precession repeats on each revolution the particles are on the so called *spin closed orbit*.

[3] As long as the coupling between the horizontal and vertical betatron motion is not present.

beam up to the maximum beam momentum. For this purpose a special setting of the magnets is required [78] with S = 2, thus four additional intrinsic resonances appear, all listed in Table 4.1. The occurance of the imperfection resonances does not depend upon the superperiodicity.

Resonance type	γG	S	p_{beam} (MeV/c)	ϵ_r (10^{-3})	P_f/P_i
IMP	2	—	463.8	0.95	−1.00
INT	$6-Q_y$	2	826.9	0.26	0.20
IMP	3	—	1258.7	0.61	−0.88
INT	$0+Q_y$	2	1639.3	0.21	0.43
IMP	4	—	1871.2	0.96	−1.00
INT	$8-Q_y$	2;6	2096.5	1.62	−1.00
IMP	5	—	2442.6	0.90	−1.00
INT	$2+Q_y$	2	2781.2	0.53	−0.74
IMP	6	—	2996.4	0.46	−0.58
INT	$10-Q_y$	2	3208.9	0.25	0.25

Table 4.1: Imperfection (IMP) and intrinsic resonances (INT) at the synchrotron COSY.

The ratio of the preserved polarisation P_f/P_i depends on the strength of a resonance (see Table 4.1). Each time the beam is crossing the imperfection resonances, the polarisation may be completely lost if the strength of the resonance is not sufficient to flip the spin of all beam particles. At some ϵ_r value, for a certain imperfection resonance and certain momentum spread of the beam $\Delta p/p$, the ratio P_f/P_i is equal to -1, which means that crossing the resonance with a proper strength one deals with the spin flip, with no polarisation loss. Simulations reported in reference [78] showed, and the experiments confirmed, that the excitation of the vertical orbit by 1 mrad, using the horizontal correcting dipoles, is sufficient to adiabatically flip the spin at all imperfection resonances.

Another method to overcome the imperfection resonances involves the use of spin rotators – so called siberian snakes. At the synchrotron COSY the solenoids of the electron cooler, acting as the partial siberian snake, are able to rotate the spin around the longitudinal axis by circa 8° at the maximum momentum of COSY [78]. It has been experimentally proven that a rotation angle of less than 1^0 leads to a total spin flip with no polarisation loss at all five imperfection resonances.

In order to avoid the intrinsic resonances the technique of tune jumping is applied. A sudden tune jump increases significantly the crossing speed of the resonance and therefore the beam "jumps over" the intrinsic resonance with less than 5% polarisation loss at the strongest intrinsic resonances and no more than

1% loss at all other intrinsic resonances [78].

The experiments discussed in this dissertation have been performed at the beam momenta of $p_{beam} = 2.010$ and 2.085 GeV/c. Thus, according to Table 4.1, three imperfection and two intrinsic resonances had to be crossed. Finally, as we shall see in Section 5.4, the obtained polarisation degree was equal to about 68% and 66% at the lower and higher beam momentum, respectively.

4.2 COSY-11 facility

The detectors needed for identification of the $pp \to pp\eta$ and $pp \to pp$ reactions are described. The trigger conditions for both reactions are given.

The experiments described in this dissertation have been performed by means of the COSY-11 detector setup [18] presented in Figure 4.3. COSY-11 is an internal experiment at the cooler synchrotron and storage ring COSY, designed to study the production processes, the structure, and interactions of the mesons in the 1 GeV mass range. The facility makes use of a regular COSY dipole magnet, acting as a magnetic momentum spectrometer for charged reaction products.

A vertically polarised proton beam has been scattered on the H_2 molecules from an internal cluster target [79, 80] installed in front of the COSY magnet. Reaction products possess lower momenta than the beam protons, therefore these are bent more in the magnetic field of the dipole. Positively charged ejectiles leave the scattering chamber [18] through the thin exit window[4] reaching the detection system operating under the atmospheric pressure.

Trajectories of the positively charged protons, which are bent to the inside part of the ring, are measured by means of two planar drift chambers [18, 81] D1 and D2, presented schematically in Figure 4.3. These drift chambers are spaced by 70 cm and contain together $6 + 8 = 14$ detection planes. The active area of the chambers is 1680×433 mm^2. The D1 chamber contains 6 detection planes; two planes with vertical wires, two with wires inclined by $+31^\circ$, and last two with wires inclined by -31°. The D2 drift chamber has additional two planes in the back part with vertical wire orientation. The wires of the consecutive planes of each pair are shifted by half of the cell width (20 mm) in order to resolve the left-right ambiguity of passing through particles. Drift chambers operate with a gas mixture of 50% argon and 50% ethane at slightly more than atmospheric pressure. The particle trajectories are reconstructed using the computer code MEDUZA [82]. The code allows for reconstruction of multiple track events.

[4] This exit window (1870×76 mm^2) is made of a 30μm layer of aluminum foil, and two crossed unidirectional sheets of carbon fibers soaked in epoxy resin of 150μm width, acting as an outward carrier material. The choice of materials with low nuclear charge reduces straggling in the exit window to values below the resolution of the detection system [18].

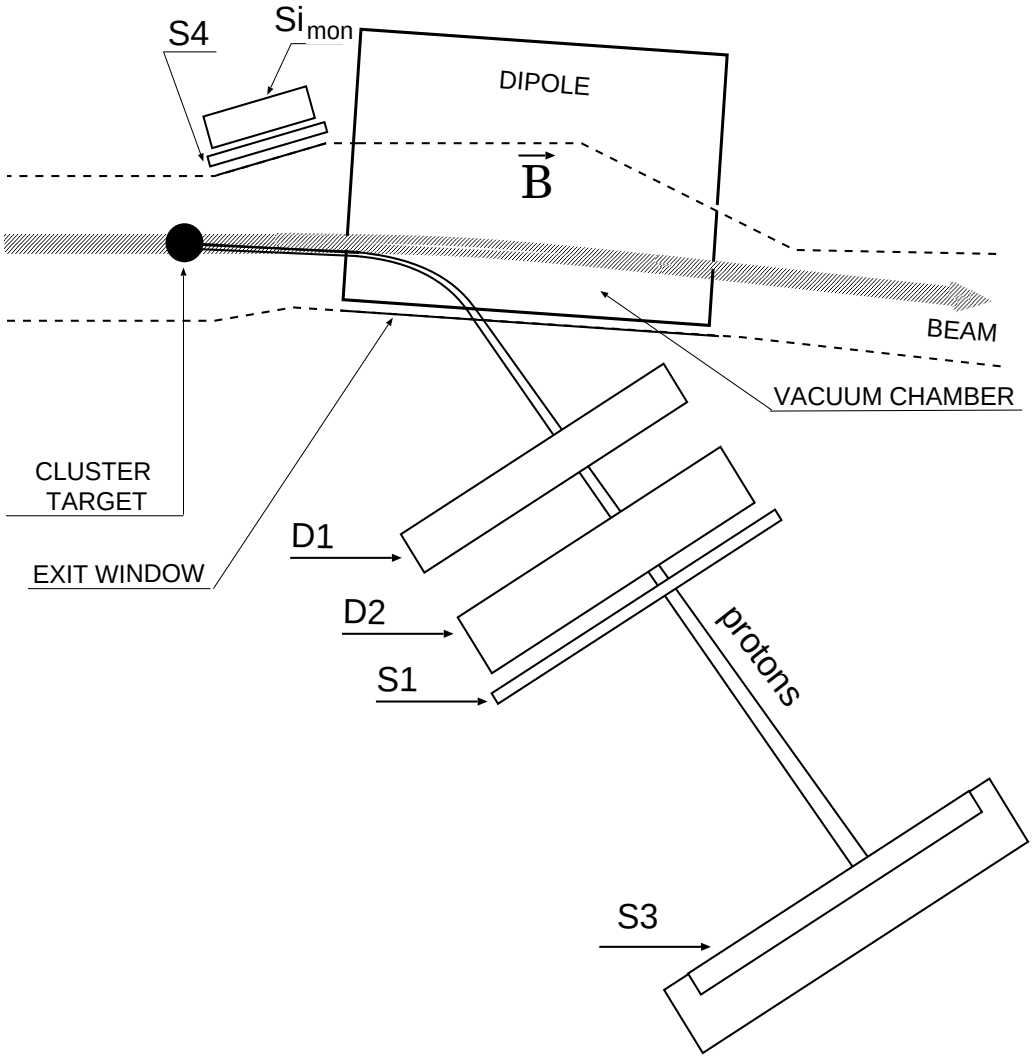

Figure 4.3: Schematic top view of the COSY-11 detection setup [18]. Only detectors needed for measurements of the $\vec{p}p \to pp\eta$ and $\vec{p}p \to pp$ reactions are shown. S1, S3, and S4 denote the scintillator detectors; D1 and D2 stand for the drift chambers; Si_{mon} are the silicon detectors for measurements of the elastic scattering. Figure is adapted from [23].

The particle trajectories are traced through the magnetic field of the dipole back to the interaction point. In this way the momenta of the particles can be determined with precision of 4 MeV/c (standard deviation) [8].

Leaving the drift chambers, the positively charged reaction products pass the scintillator hodoscope S1 [18], consisting of 16 scintillation modules with dimensions of 450 × 100 × 4 mm^3 made of Bicron BC 404 [83]. The scintillators are arranged vertically and read out at both sides by photomultipliers. The time resolution of this hodoscope in the range between 160 and 220 ps has been measured [84], depending on the hit position. This detector delivers the start signal

for the time-of-flight measurement.

The stop signal of the time-of-flight measurement is generated in the S3 scintillator wall [18] (made of a 220 × 100 × 5 cm^3 scintillator Bicron BC 404), situated at a distance of circa 9 m from S1. The scintillator wall generates a light signal upon a charged particle crossing its volume. This signal is read out by a matrix of 217 photomultipliers. The scintillator wall and the photomultipliers are separated with 4 cm air gap. The centre of gravity of the pulse height from individual photomultipliers is calculated in order to resolve the hit position of a particle. The restriction of few photomultipliers responding allows to separate two or more hit positions in the scintillator wall.

Time-of-flight measurement together with a reconstructed momentum of a particle yields a possibility of indentification of the particle by calculating its mass. Hence, the four momenta of the outgoing particles can be determined. This information, in connection with the known four momenta of initial state particles allows to calculate the missing mass of the undetected particle or system of particles. The missing mass method will be described in Section 5.1.5.

The trigger condition for registering the $\vec{p}p \to pp\eta$ reaction is:

$$T_{\vec{p}p\to pp\eta} = (S1_{\mu\geq 2} \vee S1_{\mu=1,high}) \wedge S3_{\mu>2}, \tag{4.3}$$

where μ denotes the multiplicity of segments in the S1 detector, and also the multiplicity of the photomultipliers that have fired in the S3 detector. Subscript *high* stands for the high energy deposition in the S1 scintillator module, corresponding to the case when two or more particles cross a single module.

Similarly, for registering the $\vec{p}p \to pp$ reaction a trigger condition of the type

$$T_{\vec{p}p\to pp} = S1_{\mu=1} \wedge S4 \tag{4.4}$$

has been set, where S4 is a scintillator detector used for registering the recoil protons from the elastic scattering. Protons passing through this detector reach the granulated silicon-pad detector Si_{mon} consisting of 144 silicon pads with dimensions of 22×4.5×0.28 mm^3 arranged in three layers one above the other. Two of the layers are located in the front part of the detector and one in the back.

For completeness we would like to mention that there are other detectors building up the COSY-11 facility like the silicon pad detector [85, 86] for the spectator protons from the quasi-free $pd \to ppnX$ reactions [87–89], the neutron detector [85, 90–92], the Cherenkov detector [93], the C-shaped hexagonal chamber [94] and the auxiliary scintillator detectors [18, 23]. However, as these detectors were not used during the experiments reported in this dissertation we omitted their description herein. The interested reader is referred to the publications quoted above.

Chapter 5

Data Analysis

5.1 Calibration of the detection system

5.1.1 Time-space calibration of the drift chambers

The method of time-space function derivation for the drift chambers is described.

The drift chambers described in Section 4.2 operate with a gas mixture of 50% argon and 50% ethane at slightly more than atmospheric pressure. Upon crossing of a charged particle through the gas-filled volume the electron clusters are generated and move towards the anode wires. The drift time of the electron clusters to the anode wire is a measure of the minimum distance between the sense wire and the trajectory of the particle. This relation is called a time-space calibration of the drift chamber and has to be determined from the experimental data.

The drift velocity varies with the atmospheric conditions [95]. Therefore, in order to perform the time-space calibration the experimental data have been divided into 32 groups for each energy, each group corresponding to about 6 hours of measurement. The time-space calibration [23] has been performed iteratively starting with an approximate time-space function $d(t)$. From this function and from measured drift times the points where the particle crossed the middle of the cells have been found for each detection plane and the straight line corresponding to the particle's trajectory has been fitted. For such obtained trajectory of the particle for an i-th event the distance d_i' to the sense wire has been calculated and the average of the differences

$$\Delta d(t) = \frac{\sum_{i=1}^{n} (d_i(t) - d_i'(t))}{n} \tag{5.1}$$

obtained from the mentioned sample of the experimental data have been used in order to correct the time-space function. In the Equation 5.1 d_i denotes the distance between the particle trajectory and the sense wire for an i-th event,

reconstructed using the $d(t)$ calibration function. Subsequently, new time-space functions $d(t) + \Delta d(t)$ have been used for further iteration. The procedure has to be repeated until the Δd corrections becomes negligible.

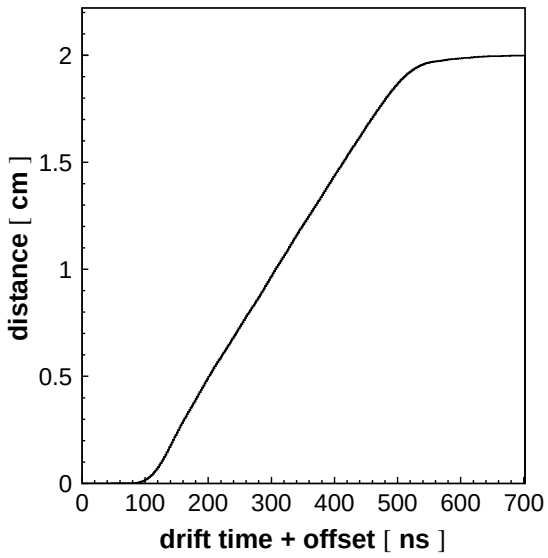

Figure 5.1: Distance from the sense wire as a function of the drift time for an arbitrarily chosen cell of DC1 – so called time-space calibration of the drift chambers.

Figure 5.1.a presents the time-space calibration of an arbitrarily chosen sense wire of the DC1. The linearity of the distance from the sense wire as a function of the drift time may be seen in the range between circa 100 and 500 ns. The value of 100 ns corresponds to the time offset introduced by the electronics.

5.1.2 Time-of-flight calibration

Time calibration of the scintillator detectors used for time-of-flight measurement is presented.

As it was mentioned in Section 4.2 the S1 and S3 counters serve as a start and stop detectors, respectively, for the time-of-flight measurement. As the S1 scintillator consists of 16 modules, in which signals are read from both sides by photomultipliers and the signals from S3 scintillator are read by a matrix of 217 photomultipliers, in order to obtain the credible time-of-flight information, the relative time offsets of the electronics for each photomultiplier have to be determined.

For the S1 time calibration, we used the events where particles were crossing adjacent modules. In this case we can assume that in both modules the signal is generated at the same time. The TDC value of the single photomultiplier of the S1 detector can be expressed as follows [23]:

$$TDC_{s1} = t_{s1} + t_y + t_{s1}^{walk}(PM) + t_{s1}^{offset}(PM) - t_{trigger}, \tag{5.2}$$

with t_{s1} denoting the real time of the signal generation in the S1 detector and t_y standing for the time that the signal needs for passing the distance between the hit position in the scintillator module and the edge of the scintillator. The t_{s1}^{walk}(PM) is the time walk effect correction[1], t_{s1}^{offset}(PM) denotes the time offset of the electronics for a given photomultiplier, and $t_{trigger}$ is the time when the trigger pulse started the readout of TDC modules.

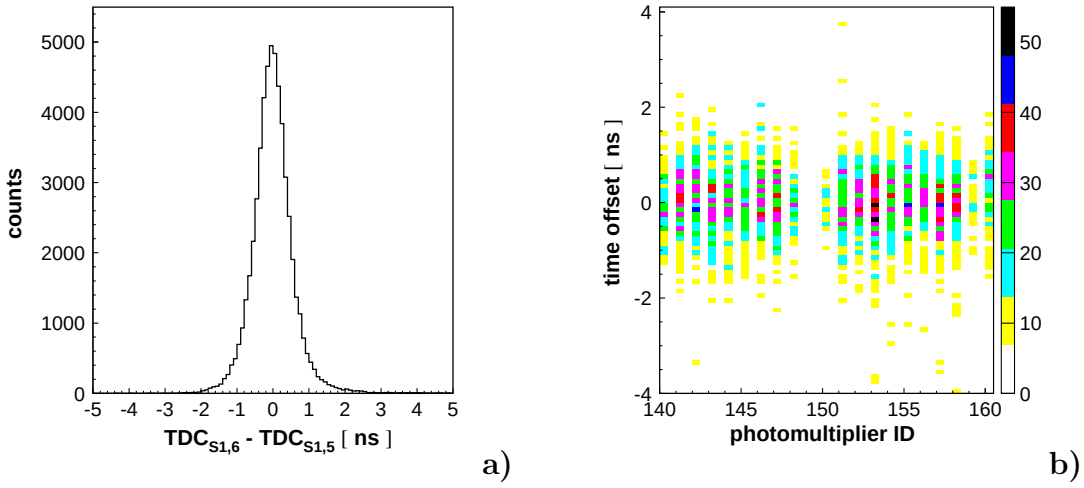

Figure 5.2: (a) Determined TDC time difference between arbitrarily chosen 6$^{\text{th}}$ and 5$^{\text{th}}$ module of the S1 scintillator detector after the calibration. (b) Difference between time-of-flight measured on the S1-S3 path from the signals registered in S1 and S3 detectors, and the time-of-flight between S1 and S3 calculated from the reconstructed momentum of the particle.

After the drift chamber calibration, we have chosen the events with only one track reconstructed and a signal in two neighboring modules of the S1 detector. The time offset for the first module in S1 (the one standing most to the inner part of the ring) has been set arbitrarily. Then, the time difference: $t_{s1,2}^{offset}$ = TDC$_{S1,2}$ - TDC$_{S1,1}$ has been taken as a correction for the time offset between the second

[1]By the *time walk effect* we understand the variation of the registered TDC time with the amplitude of the signal typical for leading edge discrimination [96]. This effect can be corrected by adding an offset t_{s1}^{walk}(PM)= $\frac{1}{\sqrt{ADC}}$, with ADC denoting the signal charge value [23].

and the first module of the S1 detector. The same procedure has been repeated for all modules. Figure 5.2.a depicts the TDC time difference between arbitrarily chosen 6^{th} and 5^{th} module of the S1 counter upon single particle crossing through the overlap region, after the correction for the time offset of the electronics and photomultipliers. One can see that this time difference is peaked around the zero value, which confirms the correctness of the time calibration of the S1 scintillator.

Having adjusted the time offsets of the individual photomultipliers in the S1 detector and hence having established the common start for the time-of-flight measurement we need to adjust the time offsets for each of the 217 photomultipliers in the S3 detector in order to set up the common stop. Similarly as it was in the case of the S1 detector, the TDC value for the individual electronic channel, corresponding to the single photomultiplier in the S3 detector reads:

$$TDC_{s3} = t_{s3} + t_{pos} + t_{s3}^{walk}(PM) + t_{s3}^{offset}(PM) - t_{trigger}. \tag{5.3}$$

Here, the t_{pos} denotes the time that light signals need to pass from the scintillation origin down to the photomultiplier photocathodes.

In Equations 5.2 and 5.3 the $t_{trigger}$ values are the same, and so the time-of-flight value

$$TOF(PM) = t_{s3}(PM) - t_{s1} \tag{5.4}$$

does not depend on the triggering time. Hence, the only unknown quantities in the TOF calculation are the time offsets for the individual photomultipliers in the S3 detector – $t_{s3}^{offset}(PM)$. These values determined for each photomultiplier can be extracted from comparing the TOF values with the time-of-flight calculated from the reconstructed momenta of the particles. The differences after the calibration for the photomultipliers no. 140-160 are presented in Figure 5.2.b. In order to extract the $t_{s3}^{offset}(PM)$ values the one-track events with an identified proton has been chosen.

Having established all the time offsets of the photomultipliers in the S1 and S3 scintillators, the time-of-flight were calculated as TOF $= t_{s3} - t_{s1}$. One should mention that the t_{s1} have been taken as the average of times from the upper and lower photomultipliers of the hit module, and t_{s3} were the weighted mean times for the proper cluster of photomultipliers in the S3 detector that registered the light pulses. For more details on the S1 and S3 calibration the reader is referred to [23].

5.1.3 Position of the drift chambers

A method for the search of the optimal position of the drift chambers is presented.

The time-space calibration of two drift chambers D1 and D2 has been described in Section 5.1.1. It is very important to know the exact position of these

drift chambers in order to achieve the required resolution in the momentum reconstruction of outgoing protons. This position can be parameterized for example introducing the parallel shift of drift chambers, which in the following we will denote by Δx, and their inclination $\Delta\alpha$. Both parameters are illustrated in Figure 5.3.

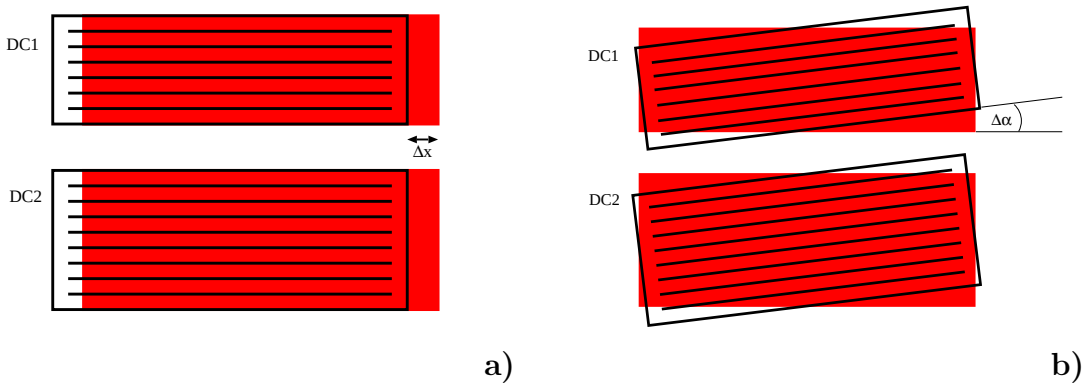

Figure 5.3: Schematic illustration of the parameters Δx (a) and $\Delta\alpha$ (b) mentioned in the text.

The parameters Δx and $\Delta\alpha$ influence the resolution of reconstructed four momenta of outgoing particles, and consequently influence also indirectly the missing mass resolution $\sigma\,(mm^2)$. The studies of the missing mass resolution as a function of Δx and $\Delta\alpha$ have been performed on the data set for the excess energy of Q = 10 MeV in order to optimize the position of drift chambers. We have varied these parameters in the range of $[-1cm; 2cm]$ for Δx, and $[-0.015°; 0.055°]$ for $\Delta\alpha$, investigating the width of the missing mass spectra as a function of these parameters. The minimum value of the width of the η peak in the missing mass squared histogram (which we will present in Section 5.1.5) has been found for Δx = 0.35 cm and $\Delta\alpha = 0.025°$ and equals $\sigma\,(mm^2) = 0.00164$ GeV^2/c^4. This corresponds to the value of the width of η missing mass peak which is $\sigma\,(mm) = 1.5$ MeV/c^2.

For the analysis at the excess energy of Q = 36 MeV the same optimal parameters have been chosen.

It is important to note that the determined values of Δx and $\Delta\alpha$ are in a very good agreement with the result obtained in the preceeding COSY-11 analyses [17, 25].

5.1.4 Beam-target relative settings

It is shown that the relative position of the beam and target influence the reconstructed momenta of the particles. A search for the optimal setting is presented.

Another parameter that influences the resolution of the reconstruction of four

momenta of protons are the dimensions of beam and target and also the relative position between them. In the procedure of momentum reconstruction it is assumed that the interaction vertex is a point where the infinitesimally thin target intersects with the absolutely thin beam of protons. However, in reality both beam and target are of finite dimensions. Therefore, the reactions may be initiated in some finite volume, size of which depends on the abovementioned parameters, introducing a spreading to the reconstructed four momenta of protons. In the analysis, following the studies reported in [27, 97], we used the approach that the target may be described by a cylinder of radius $r = 4.5$ mm with uniformly distributed protons [79, 80], and the density of the protons in the beam is given by the two dimensional gaussian distribution, as schematically illustrated in Figure 5.4. The σ_X and σ_Y denote spreadings of the beam distribution in horizontal and vertical directions, respectively. Basing on the previous measurements [97], in our Monte Carlo studies we assumed these parameters to equal $\sigma_X = 0.2$ cm and $\sigma_Y = 0.5$ cm. Distance between the centre of the target and the centre of proton beam distribution is denoted in Figure 5.4.a by b_X.

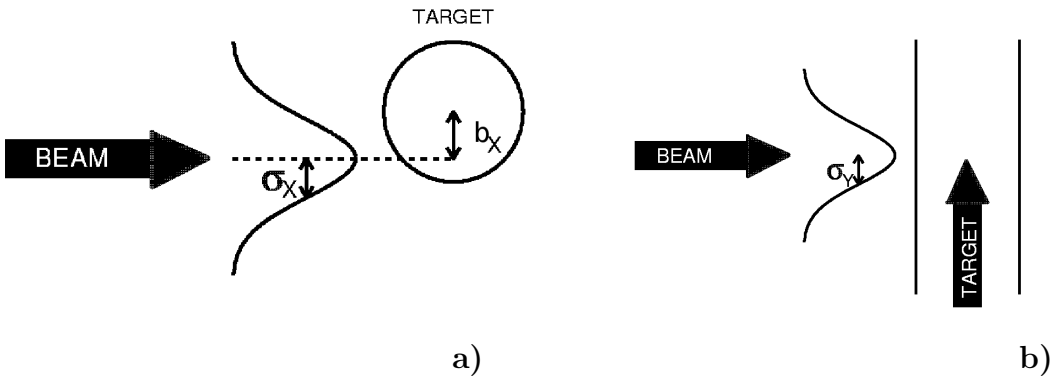

Figure 5.4: Schematic illustration of the beam and target dimensions and their relative position: (a) view from above, (b) side view. Figure is adapted from [27].

Let us denote by Δ_X the deviation between the center of the reaction region and the nominal position of the target. In order to determine the position of the center of the reaction region we used the elastically scattered protons, registered by means of the detectors shown in Figure 5.5. Forward scattered protons from the elastic process are detected by the scintillator detector S1 and the drift chambers D1 and D2. The recoil protons passing through the scintillator S4 reach the granulated position-sensitive silicon detector Si_{mon}.

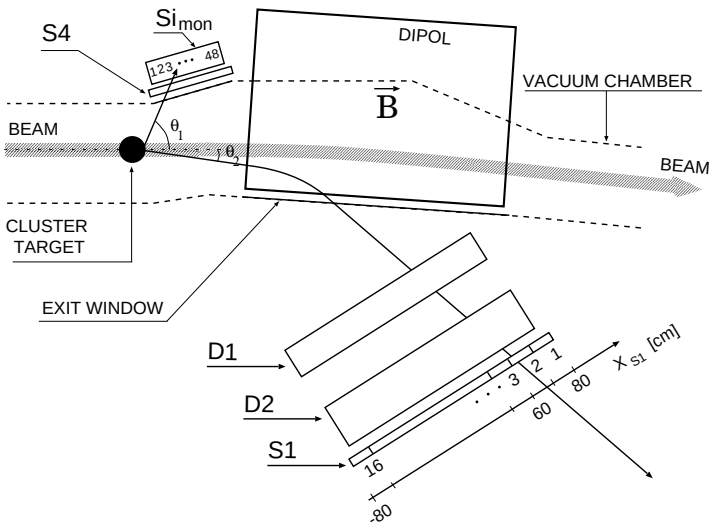

Figure 5.5: Schematic view of the COSY-11 detection setup. Only detectors used for the measurement of the proton-proton elastic scattering are shown. Figure is adapted from [23].

As the proton scattered forward under the θ_2 angle – passes through the stack of drift chambers D1 and D2, its trajectory may be reconstructed and subsequently traced back to the reaction vertex, through the known map of the magnetic field inside the COSY dipole. This procedure yields the momenta of the particles passing through the drift chambers. Further, the reconstructed momentum vector may be decomposed at the reaction point into two components: the transversal ($p_\perp$) and the longitudinal one ($p_\parallel$), with respect to the momentum of the beam protons. The two body kinematics puts some constraints on these two components, namely the set of points $\left(p_\parallel, p_\perp\right)$ should form an ellipse [98] in the momentum plane. The size of this ellipse depends on the $\sqrt{s}$ – the total energy in the centre-of-mass system. A part of one arm of this theoretical ellipse for the $\sqrt{s} = 2.43$ GeV, corresponding to the proton beam momentum of $p_{beam} = 2.010$ GeV/c, is depicted in Figures 5.6.a and 5.6.b as the solid line.

The value of the reconstructed particle's momentum depends on the correctness of the assumption of the reaction vertex position. Shifting the reaction vertex upwards the beam line presented in Figure 5.5 would yield in higher reconstructed momenta of the particles, as we decrease the curvature of the trajectory inside the dipole magnet. On the other hand, a parameter Δ_X with the negative values (shift of the reaction vertex downwards in Figure 5.5) would induce a higher curvature of the tracks inside the dipole magnet, hence lower momenta of the reaction products. The values of the components of the reconstructed momentum vector correspond to a point in the momentum plane $p_\perp$ – $p_\parallel$. This point is lying inside or outside the expected theoretical ellipse, depending whether the reconstructed particle's momentum is lower or greater than the actual one.

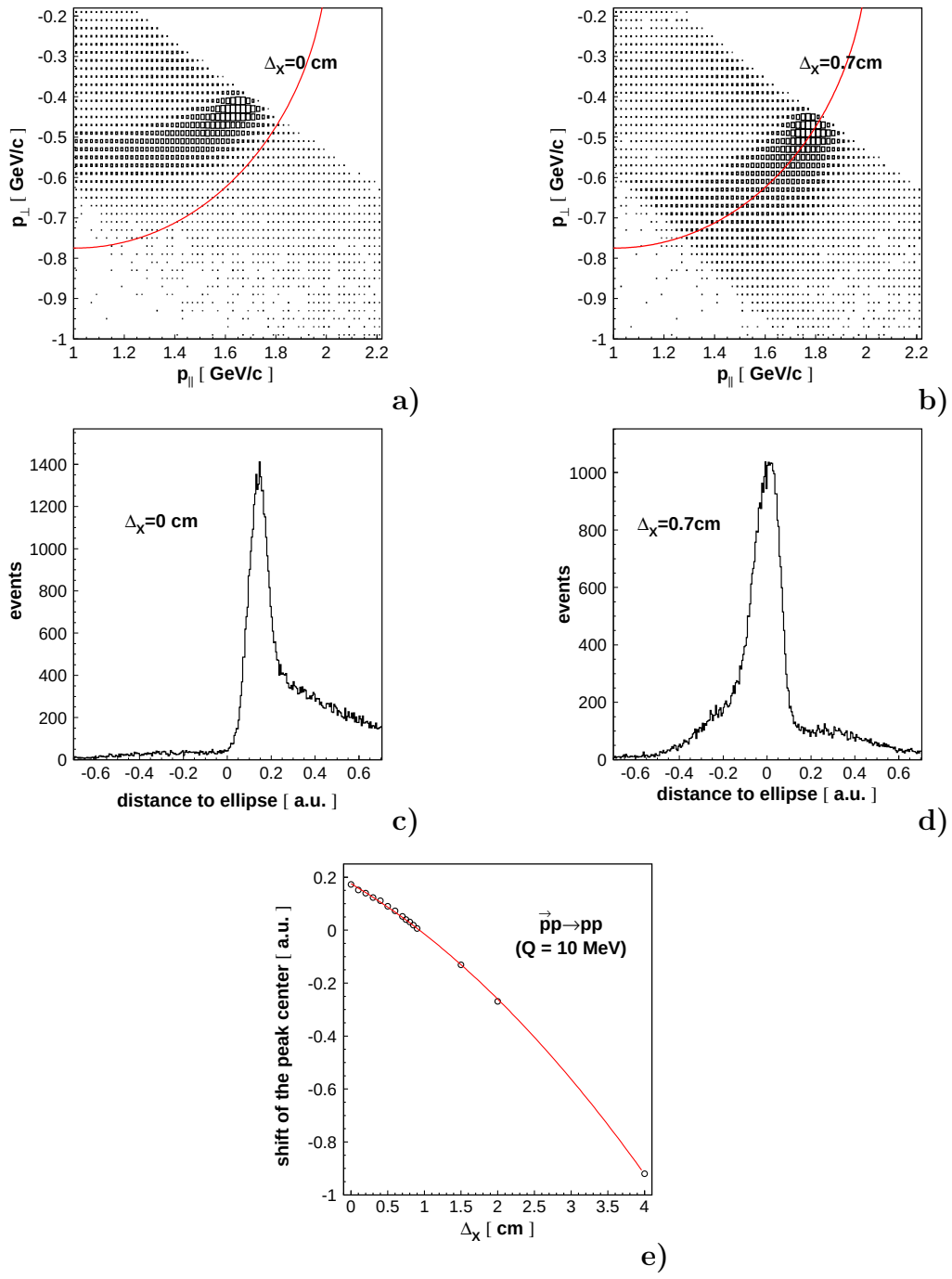

Figure 5.6: Perpendicular versus parallel momentum component of the elastically scattered protons measured at the beam momentum of $p_{beam} = 2.010$ GeV/c for $\Delta_X = 0$ (a) and $\Delta_X = 0.7$ cm (b). The solid line represents the theoretical kinematical ellipse for this particular value of the beam momentum. Enhancement of the event distribution shows the elastically scattered protons over the constant background originating from the production reactions. Figures (c) and (d) show the projections of the event distribution along the theoretical ellipse for data from figures (a) and (b) respectively. (e) Distance between the theoretical ellipse and the centre of the points distribution from the $(p_\perp - p_\parallel)$ plot versus the parameter Δ_X.

Following the studies of [97] we have been searching for the optimal position of the reaction vertex, by changing the Δ_X parameter in the range from 0 to 4 cm. In Figure 5.6.a a distribution of the reconstructed momenta of the elastically scattered protons is presented, for the case where Δ_X was set to $\Delta_X = 0$. The enhancement of the event distribution is assigned to the elastically scattered protons. The background is mainly due to many body reactions. As one can see, the reconstructed momenta of the elastically scattered protons are lying inside the theoretical kinematical ellipse, which means that the reconstruction yields too small values of the particle's momentum. This is also seen in Figure 5.6.c, where we presented the projection of the event distribution along the kinematical ellipse. One can notice the shift of the centre of the distribution outside the zero value.

For the same data sample and with $\Delta_X = 0.7$ cm the components of the reconstructed particle's momenta are lying on the kinematical ellipse, as can be seen in Figure 5.6.b. Figure 5.6.d shows the projection of the data set onto the kinematical ellipse for this case. Indeed, the event distribution is centered around the zero value. This means that for the data sample we considered here, the optimal value of the Δ_X parameter equals $\Delta_X = 0.7$ cm.

The same procedure has been differentially performed for the whole sample of data. The experimental data have been divided into 32 groups, corresponding to about 6 hours of measurement, and for each out of these 32 groups the value of the Δ_X parameter has been determined using a χ^2 test, where χ^2 was calculated between the experimental event distribution and the theoretical kinematical ellipse.

In Figure 5.6.e we have presented the relation between the parameter Δ_X and the shift of the centre of the peak, originating from the projection of the experimental points along the kinematical ellipse. This dependence have been studied in the Δ_X range from 0 to 4 cm, and it was found that it may be described fairly well by a polynomial function of second order, the one presented in the Figure 5.6.e. One can see in this figure that the zeroth shift of the peak centre corresponds to the value of $\Delta_X \approx 0.7$ cm.

5.1.5 Missing mass technique

The idea of the missing mass technique is sketched. The software presort of the events with two protons in the final state is given. We also present the missing mass spectra for both excess energies.

As the η meson is a non-charged short living particle, its direct registration in any of the nowadays known detectors is impossible due to the very low distance that is passed by this particle before it decays[2]. To our best knowledge, nowadays

[2]The Particle Data Group [99] gives the value of the total width of the η meson Γ_η =

three methods are applied in the worldwide experiments in order to identify the η meson. First of them is the missing mass technique, which will be described in the following part of this section. Second method is the reconstruction of the four momentum of the η meson by means of the identification of its decay products, e.g. 2γ rays. Third method is the combination of the two latter techniques, namely, the measurement of the 2γ decay in coincidence with the directions (and/or energies) measurements of two final particles. This method, for example, will be used at the recently installed WASA-at-COSY experiment [69].

The idea of the missing mass technique involves the theorem of the four momentum conservation. Let us consider the $pp \to ppX$ reaction with the accelerated proton beam and the proton target with zero momentum value. Denoting by $P_b = (E_b, \vec{p}_b)$, $P_t = (E_t, 0)$, $P_1 = (E_1, \vec{p}_1)$, and $P_2 = (E_2, \vec{p}_2)$ the four momenta of the beam, target, and two outgoing protons, respectively, one can calculate the missing mass (m_X) of an undetected particle or system of particles in the exit channel according to the formula:

$$\begin{aligned} m_X^2 = E_X^2 - \vec{p}_X^{\,2} = (P_b + P_t - P_1 - P_2)^2 = \\ = (E_b + E_t - E_1 - E_2)^2 - (\vec{p}_b + \vec{p}_t - \vec{p}_1 - \vec{p}_2)^2 . \end{aligned} \tag{5.5}$$

After the adjustment of the drift chambers' parameters Δx and $\Delta\alpha$ and the parameter Δ_X, and having performed the time calibration of the S1 and S3 scintillators, as well as the calibration of the drift chambers (described in Sections 5.1.1–5.1.4) one can reconstruct the momenta of the outgoing particles and also their velocities. Having the momenta ($\vec{p}$) and velocities (β) of the particles one can calculate their squared invariant masses applying the relativistic formula:

$$m^2 = \frac{(\vec{p})^2\,(1-\beta^2)}{\beta^2}. \tag{5.6}$$

Figure 5.7 shows the distribution of the invariant masses of two particles measured in coincidence at the excess energy of Q = 10 MeV. Over the background arise four "isles" of the events with π^+-π^+, π^+-proton, proton-π^+, and proton-proton identified in the final state. For the further analysis only events with two protons were taken into account. The software cut on the squares of the missing masses of particles is denoted with the solid lines. The dotted lines show the values of the π^+ meson and proton squared masses.

1.30 $\pm$ 0.07 keV, which yields the mean life-time of the η meson equal to $\tau_\eta = (5.10 \pm 0.29) \cdot 10^{-19}$ s, corresponding to $c\tau_\eta = 1.53 \cdot 10^{-10}$ m.

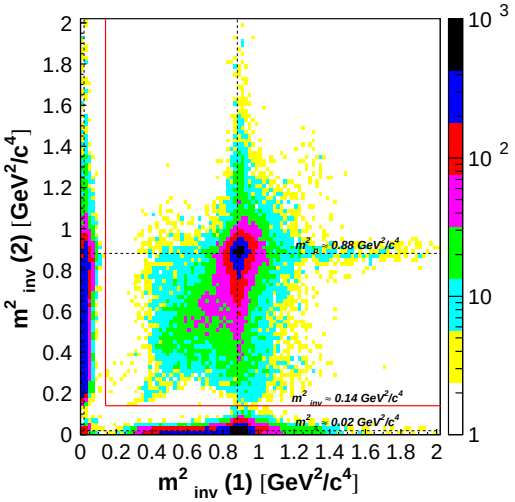

Figure 5.7: Squared masses of two simultaneously measured particles in the exit channel. Events from the measurement of the $\vec{p}p \to pp\eta$ reaction at the excess energy of Q = 10 MeV are presented.

Knowing all the four momenta – P_b, P_t, P_1, and P_2 – and applying Equation 5.5 one can calculate the missing mass of X for each event separately. The spin-averaged missing mass spectra for the $\vec{p}p \to pp\eta$ reaction as measured using the COSY-11 detection setup are presented in Figure 5.8. Over the wide background, originating mainly from the multipionic production, clear η peaks are visible for both measurements. There are around 3000 and 1500 η events at Q = 10 and 36 MeV, respectively, integrated over both spin orientations.

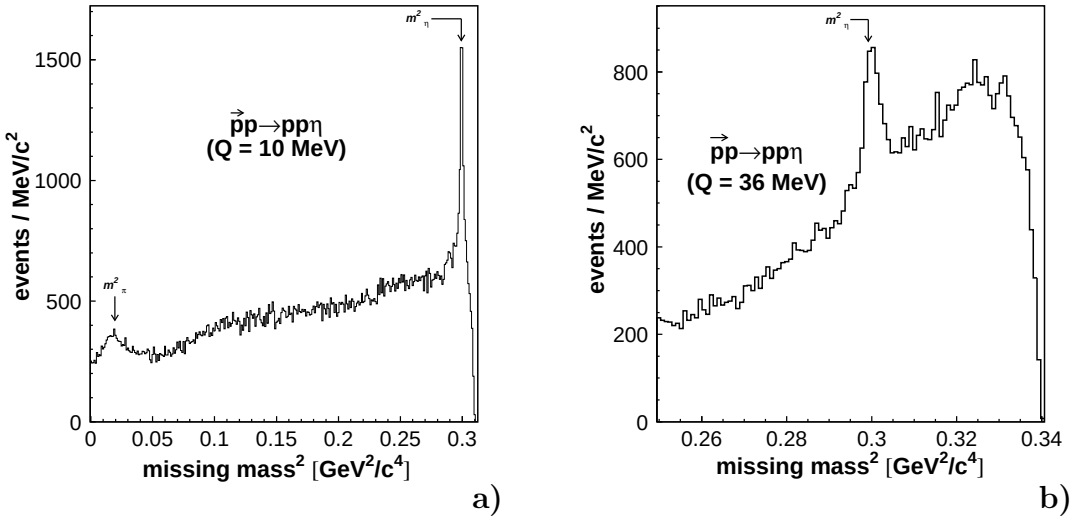

Figure 5.8: (a) Spin-averaged spectrum of the square value of the missing mass for the $\vec{p}p \to pp\eta$ reaction at the excess energy of Q = 10 MeV, as measured by means of the COSY-11 detector setup. (b) The same, but for the excess energy of Q = 36 MeV.

The differences in the shape of the background are due to the different trigger setting between two measurements, and also due to the fact that in both analyses different software cuts have been applied. It is also visible that the signal from the η meson production at Q = 10 MeV is closer to the kinematical limit than the signal at Q = 36 MeV. This is due to the fact that the kinematical limit m_{max}

$$m_{max} = m_\eta + Q, \tag{5.7}$$

equals[3] m^2_{max}= 0.311 MeV^2/c^4 at Q = 10 MeV and it equals m^2_{max}= 0.340 MeV^2/c^4 at Q = 36 MeV.

5.2 Identification of the spin up and down modes

It is shown how we resolve the problem of the identification of the spin state of the polarised proton beam using the elastically scattered events.

A few words of explanation are required concerning the method of spin up and down identification. In principle the polarisation state could have been determined from the known spin orientation in the polarised ion source and the number of imperfection resonances, mentioned in Section 4.1.3, to be crossed in order to accelerate the beam up to the required momentum. However, even without a precise knowledge of the beam optics during the acceleration process it is possible to determine the spin state of accelerated protons.

To enable an offline assigment of the polarisation mode two scaler channels have been used, working in the sequence mode. Whenever there was a beam in the spin state A one of the scaler channels has been working while the other one remained idle, and vice-versa.

In order to identify the spin state A with spin up or down mode the detector system of Figure 5.5 for registration of the elastic scattering in the accelerator plane has been used.

For the elastically scattered protons at the beam momentum of p_{beam} = 2.010 MeV/c, which reach the drift chambers D1 and D2 (see Figure 5.5) the scattering angle θ_2 may vary from 35° to circa 80° [4] in the centre-of-mass system. Here we deal only with scattering to the right with respect to the polarisation plane. For spin up mode, where the polarisation vector of the proton beam is pointing along the Oy^{acc} axis defined in Section 2.2, the formula 2.13 – integrated

[3] In the calculations the η meson mass $m_\eta = 547.75$ MeV/c^2 [53] has been used.

[4] Which is restricted by the acceptance of COSY-11 setup for the $pp \to pp$ reaction – see also Figure 5.12.

over m_{pp}, $m_{p\eta}$, and ψ angle – reads:

$$\sigma\left(\theta_2, P\right) = \sigma_0\left(\theta_2\right)\left(1 - PA_y\left(\theta_2\right)\right) \qquad \text{for } \cos\theta_2 \in \left(35^\circ, 80^\circ\right), \phi \approx 180^\circ; \tag{5.8}$$

while for spin down it yields:

$$\sigma\left(\theta_2, P\right) = \sigma_0\left(\theta_2\right)\left(1 + PA_y\left(\theta_2\right)\right) \qquad \text{for } \cos\theta_2 \in \left(35^\circ, 80^\circ\right), \phi \approx 180^\circ; \tag{5.9}$$

where the $\pm$ sign in front of $PA_y(\zeta)$ term is subject to the Madison convention quoted in Section 2.2. As the number of registered events is proportional to the $\sigma(\zeta, P)$, from Equations 5.8 and 5.9 we expect to register more elastic scatterings during the spin down mode, since $\mathrm{A}_y\left(\theta_2\right)$ is positive for the quoted θ_2 ranges [28]. Starting with the unidentified spin orientations A and B, we divided the available range of θ_2 into 10 bins, each of 4° width. For each bin and both spin orientations the numbers of elastic scatterings $\mathrm{N}_A\left(\theta_2\right)$ and $\mathrm{N}_B\left(\theta_2\right)$ have been determined and exemplary results for the experiment performed at Q = 10 MeV are presented in Table 5.1.

$\theta_2[^\circ]$	$\mathrm{N}_A\left(\theta_2\right)$	$\mathrm{N}_B\left(\theta_2\right)$
40	200054 ± 836	353972 ± 1106
44	159864 ± 748	275061 ± 983
48	128808 ± 679	214802 ± 874
52	103183 ± 612	162223 ± 761
56	71068 ± 513	105549 ± 616
60	65849 ± 493	90496 ± 575
64	61430 ± 469	76328 ± 520
68	53476 ± 437	61810 ± 467
72	37984 ± 364	42024 ± 384
76	14784 ± 232	15694 ± 236

Table 5.1: Number of elastic scatterings $\mathrm{N}_A\left(\theta_2\right)$ and $\mathrm{N}_B\left(\theta_2\right)$ for the unidentified spin orientations A and B as a function of the CM scattering angle θ_2 as measured during the experiment with p_{beam} = 2010 MeV/c (Q = 10 MeV).

Having a look at the numbers in Table 5.1 one can notice that for each bin of the scattering angle θ_2 we have:

$$N_B\left(\theta_2\right) > N_A\left(\theta_2\right), \tag{5.10}$$

therefore one can identify mode A with the spin up orientation and mode B with spin down. The difference between $\mathrm{N}_A\left(\theta_2\right)$ and $\mathrm{N}_B\left(\theta_2\right)$ is undoubtfully statistically significant. The same method was used for identification of the spin up and down modes for the experiment at Q = 36 MeV.

5.3 Calculation of the relative luminosity

A method of the determination of the relative luminosity is presented. A detection subsystem used for this purpose is described. Systematical errors of this method are evaluated.

In order to determine the relative luminosity L_{rel} of Equation 2.22, the scattering in the polarisation plane (see page 6) had been used, as in this plane the differential cross section for any nuclear reaction induced by the strong interaction does not depend on the magnitude of beam polarisation. This is a consequence of the fact, that the parity in strong interactions is conserved. For detailed explanation the reader is referred to Appendix C.

Therefore, whenever in the experiment we are restricted to the scattering in the polarisation plane the result of the measurement should only depend on the polar angle θ, and is independent of the beam polarisation. Thus, the number of reactions – $n(t)$ – registered in the polarisation plane within a time interval t may be used as the measure of the integrated luminosity over this time interval:

$$\int_0^t L(t')dt' \sim n(t). \tag{5.11}$$

In order to determine the relative luminosity, the detector system schematically presented in Figure 5.9 had been used. It consists of four scintillator detectors: two round-shaped, placed vertically in front of the COSY-11 magnet, and two square-shaped located horizontally between the magnet coils. The location of the scintillators has been chosen in order to conform the kinematic conditions of the elastically scattered protons in the polarisation plane. The coincidence rate originates mainly from the elastic proton-proton scattering, which constitutes about 75% [100] of all reactions. The rest of about 25% comes from multibody reactions. The number of coincidences of the following type:

$$(SC_1 \wedge SC_2) \vee (SC_3 \wedge SC_4). \tag{5.12}$$

was measured.

Denoting by $n_\uparrow$ and $n_\downarrow$ numbers of coincidences integrated over the time of the measurement during the cycles with spin up and down, respectively, we get from Equation 2.22 and relation 5.11:

$$L_{rel} = \frac{\int L_\uparrow dt}{\int L_\downarrow dt} = \frac{n_\uparrow}{n_\downarrow}. \tag{5.13}$$

The numbers of coincidences $n_\uparrow$ and $n_\downarrow$ and also the relative luminosities L_{rel} for runs at Q = 10 MeV and Q = 36 MeV have been determined using this method and are presented in Table 5.2.

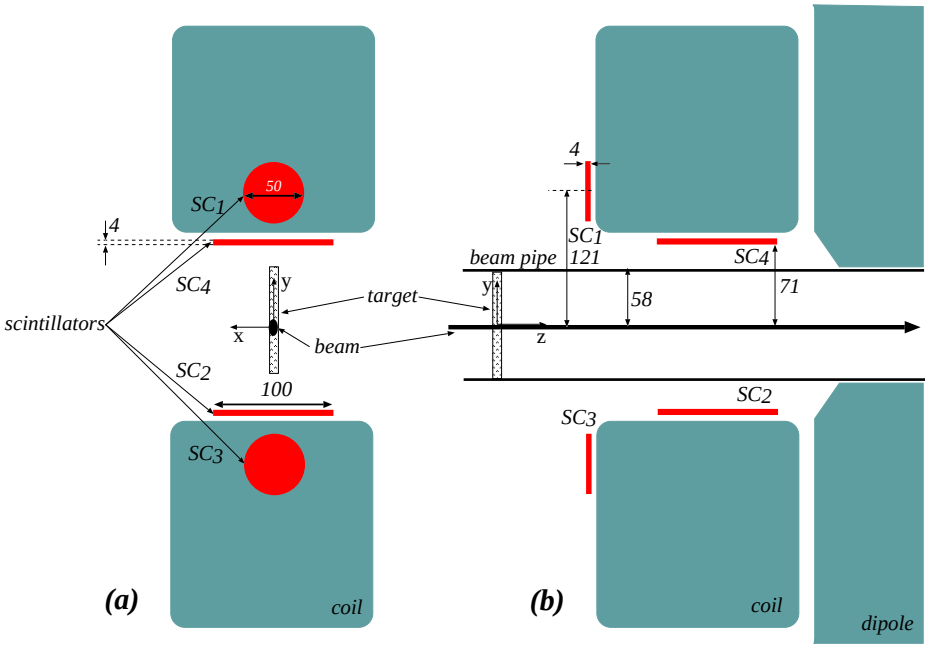

Figure 5.9: Schematic view of the detection system dedicated for the relative luminosity determination, as mounted at the COSY-11 section of the COSY ring. (a) front view, (b) side view. Beam is circulating along the z-axis and target is along the y-axis.

Q[MeV]	$n_\uparrow$	$n_\downarrow$	L_{rel}	$L_{rel}^{corrected}$
10	5732570 ± 2394	5942438 ± 2438	0.96468 ± 0.00056	0.98468
36	5657318 ± 2378	5874621 ± 2424	0.96301 ± 0.00057	0.98301

Table 5.2: Relative luminosities, and numbers needed for their calculation for runs at excess energies Q = 10 and Q = 36 MeV. $L_{rel}^{corrected}$ are the values of the relative luminosities, corrected for the shift of the target, as explained in the text below. The errors indicated in the table are the statistical uncertainties only. The systematic errors are evaluated in the text.

The detectors were installed centrally around the nominal target position ($\Delta_X = 0$), however one should keep in mind that the Δ_X found in Section 5.1.4 equals 0.7 cm. This introduces false asymmetries into the calculations of L_{rel}, and so, the values of L_{rel} have to be corrected for these false asymmetries. In order to do so, Monte-Carlo simulations have been performed, using the GEANT3-based code [101], containing the geometry of the luminosity system from Figure 5.9, and taking into account the phase-space distribution of the events modified by the differential cross sections [102] and analysing powers for the $\vec{p}p \to pp$ reaction [28]. In the simulations the real values of the polarisations (quoted in the

following section) were taken into account. Subsequently, the same number of events have been generated for spin up and down modes, and indeed, it has been found that the 7 mm shift introduces false asymmetry that changes the value of the L_{rel} from $L_{rel} = 1$ (for the symmetric system) to $L_{rel} = 0.98$. Therefore the value of $\Delta L = 1 - 0.98 = 0.02$ has to be added to the L_{rel} in order to obtain the real values of the luminosities, which in Table 5.2 we called $L_{rel}^{corrected}$.

It appears from results given in Table 5.2 that the corrected relative luminosities differ from 1 by circa 2%, although the spin was flipped from cycle to cycle. The overall integrated luminosity during spin down cycles is greater than the luminosity for spin up. This apparent inconsistency may be explained by the fact that the measurements were always started with the spin down orientation, however the breaks in the data taking (due to the target regeneration, beam optimization and other events aiming in improvement of the quality of measurement) happened accidentally with the same probability for both spin adjustments[5].

Statistical uncertainties were calculated according to the rule of the error propagation applied to Equation 5.13:

$$\sigma(L_{rel}) = \sqrt{\left(\frac{\partial L_{rel}}{\partial n_\uparrow}\right)^2 \sigma(n_\uparrow)^2 + \left(\frac{\partial L_{rel}}{\partial n_\downarrow}\right)^2 \sigma(n_\downarrow)^2}, \tag{5.14}$$

where

$$\sigma(n_{\uparrow(\downarrow)}) = \sqrt{n_{\uparrow(\downarrow)}} \tag{5.15}$$

are the statistical uncertainties of $n_{\uparrow(\downarrow)}$. After inserting the partial derivative and relations 5.15 into Equation 5.14, the formula simplifies to:

$$\sigma(L_{rel}) = L_{rel}\sqrt{\frac{1}{n_\uparrow} + \frac{1}{n_\downarrow}}. \tag{5.16}$$

After these remarks on the statistical uncertainties we will discuss the systematic errors. The main source in the systematic error of the relative luminosity determination originates from the uncertainty of the position of the scintillator detectors from Figure 5.9. A possible non-symmetrical adjustment of the detectors with respect to the polarisation plane would lead to the false asymmetries and hence to the error of the L_{rel} determination. In order to estimate the systematic

[5]Indeed, during the experiment there were circa $n = 16$ breaks in the operation of the COSY accelerator. Therefore, in average, there were around 8 cycles with spin down more than the ones with spin up. The whole time of measurement for experiment at Q = 10 MeV lasted T = 829201 s. The time period of spin up or spin down cycle for the run at Q = 10 MeV was equal to t = 1200 s. The rough estimation gives the total number of cycles (spin up and down altogether) equal k = T/t $\approx$ 690 – out of which, we assume, there were 349 cycles with spin down and 341 with spin up. Therefore the relative difference in the time of measurement with spin down and spin up mode equals to circa 2%. The same inference is valid for the experiment at the excess energy Q = 36 MeV.

error the conservative assumption has been made that the centres of the scintillators from Figure 5.9 were shifted from the nominal position by Δr = 4 mm. In order to estimate the systematic uncertainty of L_{rel}, again we have performed Monte-Carlo simulations, taking into account all the factors quoted when discussing the influence of the Δ_X on the L_{rel}. Numerical evaluation brings the value of 1% for the systematic uncertainty of L_{rel}.

5.4 Beam polarisation

The methods of the determination of beam polarisation along with the used detection systems are described. All the methods are basically based on the asymmetry measurements for the $\vec{p}p \to pp\eta$ reaction.

During two measurements of the analysing power at different excess energies, three independent methods have been used in order to determine the beam polarisation. In the run at the excess energy of Q = 10 MeV the COSY-11 polarimeter has been used as the main equipment to extract information about the value of the polarisation degree. During this run in parallel the polarimeter of the COSY team [103] has also been used as the auxiliary detector to monitor the polarisation and to verify the information from the COSY-11 polarimeter.

During the measurements performed at the excess energy of Q = 36 MeV we managed to get access to the EDDA polarimeter [103], commonly used by many experimental groups to perform the exact determination of the degree of polarisation at the COSY accelerator.

All three methods of the polarisation monitoring will be described in this section.

5.4.1 Measurement at the excess energy of Q = 10 MeV

The methods for the determination of the degree of polarisation by means of the internal COSY polarimeter as well as the COSY-11 polarimeter will be described.

The internal COSY beam polarimeter

One of the polarimeters used for the polarisation monitoring in this experiment was a polarimeter of the COSY team [103]. Subsequently we will refer to it as to the COSY polarimeter. A schematic view of this setup is presented in Fig. 5.10.

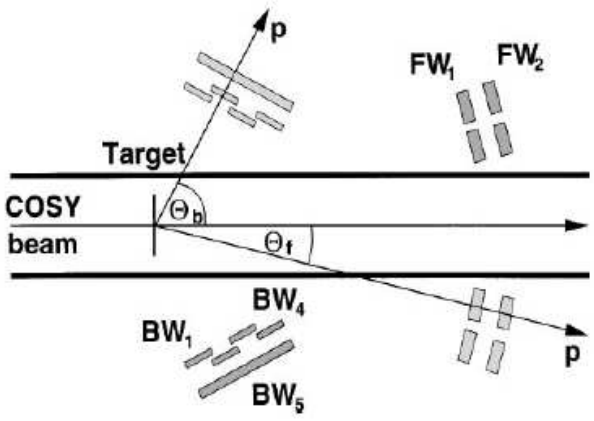

Figure 5.10: Schematic view of the COSY polarimeter. For the short-cuts' explanation see text. Figure is adapted from [103].

Protons from the polarised beam are scattered on the protons from an internal CH_2 fiber target and subsequently they reach the detectors presented in Fig. 5.10. There is a kinematical correlation between the angles of the forward (Θ_f) and backward (Θ_b) scattered protons, namely:

$$\tan\Theta_{f,lab}\tan\Theta_{b,lab} = \frac{2m_pc^2}{T_p + 2m_pc^2}, \tag{5.17}$$

where m_p denotes the proton mass, while T_p is proton's kinetic energy. The geometry of this polarimeter was designed such that due to this kinematical restriction the polarimeter can operate within the beam energy range from 300 MeV up to several GeV.

The detector setup may be rotated via remote control around the beam axis by $\Delta\phi = 290^0$ in order to eliminate the false asymmetries. For the true asymmetry measurements, the $\Delta\phi$ ranging from 23^0 (for $\Theta_f = 11^0$) to 13^0 (for $\Theta_f = 19^0$) has been used. For the dimensions and other details of the detector geometry the reader is referred to [103].

The principle of the determination of the degree of polarisation by means of this setup is based on the asymmetry (ϵ) measurements of the quasi-free $\vec{p}p$ elastic scattering realized by using a CH_2 fiber target. All the detectors presented in Figure 5.10 are scintillator detectors. The beam line is the symmetry axis of the detector setup. FW_1, FW_2, and their symmetric mirrors constitute the forward detector to register the fast proton, while the recoil protons are detected in the conjugate backward arm, consisting of four detectors BW_1, ..., BW_4, and a larger common detector BW_5 which helps to get rid of the accidental coincidences and

give the trigger signal along with the FW_1 and FW_2. Thus, the trigger conditions to be fulfilled for calculation of the asymmetry are:

$$FW_1 \wedge FW_2 \wedge BW_5, \tag{5.18}$$

for left and right arm of the polarimeter.

The asymmetry $\epsilon(\Theta)$:

$$\epsilon(\Theta) = \frac{N_+(\Theta) - N_-(\Theta)}{N_+(\Theta) + N_-(\Theta)} \tag{5.19}$$

is calculated using the geometrical averages $N_\pm$ defined as follows:

$$N_+ \equiv \sqrt{N_+^\uparrow N_+^\downarrow} = C(1 + PA_y(\theta_\eta)), \tag{5.20}$$

and

$$N_- \equiv \sqrt{N_-^\uparrow N_-^\downarrow} = C(1 - PA_y(\theta_\eta)), \tag{5.21}$$

where C is the constant depending on the detector efficiencies and the relative luminosity during spin up and down modes. The arrows denote the spin mode of the beam particles.

Thus, the degree of polarisation may be calculated as:

$$P = \frac{1}{A(\Theta)}\epsilon(\Theta), \tag{5.22}$$

where $A(\Theta)$ is the analysing power for the proton-proton elastic scattering. Please note, that the degree of polarisation calculated in this way is independent of the efficiencies of the detectors.

In order to correct the above formula for false asymmetries, originating from the beam misalignment, the following formula has been applied [104]:

$$P = \frac{1}{A(\Theta)} \frac{\epsilon(\Theta) - \epsilon'(\Theta)}{1 - \epsilon(\Theta)\epsilon'(\Theta)}, \tag{5.23}$$

where $\epsilon'(\Theta)$ stands for the false asymmetries, calculated from equation 5.19, for a measurement with an unpolarised proton beam. The results of polarisation measurement with the COSY polarimeter [105] are presented in Figure 5.14 in the following section. Here, we would only like to mention that the main source of the systematic error in the calculations of P arises from the beam misalignment and this has been estimated to be less than 4% [105].

It's worth mentioning that the construction of this polarimeter allows to calculate the polarisations for spin up and down separately. It occurs that during the experiment the discrepancy between both polarisations was less than $\pm 3\%$ [105]. In order to compare the polarisation values obtained with this equipment with the results of the COSY-11 polarimeter for time periods when the COSY polarimeter has been in operation the average values of the polarisations during spin up and down cycles have been calculated.

COSY-11 polarimeter

The second method devoted to the evaluation of the degree of polarisation made use of the COSY-11 detector setup. This method is based on the asymmetry measurement for the elastic $\vec{p}p \rightarrow pp$ process. The COSY-11 detectors that served for this purpose are presented in Figure 5.5 of Section 5.1.4.

The elastically scattered events have been identified based on the constraints given by the two body kinematics. The relation 5.17 for Θ_1 and Θ_2 puts constraints on the event distribution, and according to that relation there is a correlation between the hit position in S1 – x_{S1} – and the index of the silicon pad that gave a signal. This correlation may be seen in Figure 5.11.a as an enhancement in the density of the event distribution. The events lying outside the correlation curve originate from inelastic reactions, which occasionally fulfill the trigger conditions for the elastic scattering:

$$T_{elas} = S1 \wedge S4. \tag{5.24}$$

The background subtraction is necessary for the evaluation of $N_+(\Theta)$ and $N_-(\Theta)$ – the numbers of elastically scattered events during cycles with spin up and down, respectively.

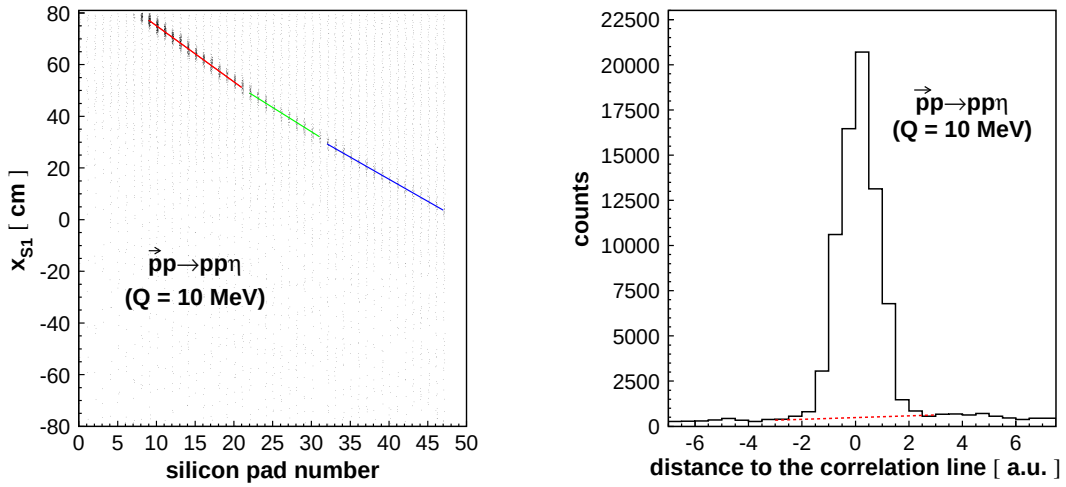

Figure 5.11: (a) Correlation plot for the proton-proton elastic scattering at the beam momentum $p_{beam} = 2010$ MeV/c. For the explanation see text. (b) Exemplary spectrum of the distance of the events to the correlation curve of Figure (a) for the arbitrarily chosen angle $\Theta_{CM} = 47^0$. The dotted line denotes the approximated background limit.

To facilitate an easy background subtraction, the correlation curve has been divided into three ranges as shown in Figure 5.11.a and in each range it was approximated by a straight line. Event distribution visible in this figure has been

projected along the correlation line, and an exemplary spectrum, for $\Theta_{CM} = 47^0$, is depicted in figure 5.11.b. Next, the linear interpolation of the background has been performed (see dashed line in Figure 5.11.b), for each range of Θ_{CM} angle. As it is seen in Figure 5.11.b, the background constitutes only about 5% of the signal, and since it is smooth and flat on both sides of the signal peak we assumed, conservatively, that the systematic error due to the assumption of the linearity of the background is less than 10%. Hence, the overall systematic error due to the background subtraction is not greater than 0.5%. Another source of the systematic error of the number of events in the individual Θ_{CM} ranges originates from the possible beam position misalignment, which may have been different for spin up and down modes. In our estimations we have assumed conservatively a 2 mm shift of the beam between spin up and spin down modes, a choice which was dictated by the geometrical dimensions of the reaction region [27]. The Monte-Carlo simulations performed with this 2 mm shift of the beam revealed the value of 0.5% of the systematic error. Therefore, the overall systematic error of the number of events in the individual Θ_{CM} ranges we estimate to be less than 1%.

After the background subtraction events lying within 2.5 or less distance from the correlation line are regarded to be elastics. Number of elastic events for scattering during spin up and down cycles allows to determine the asymmetry defined in Equation 5.19.

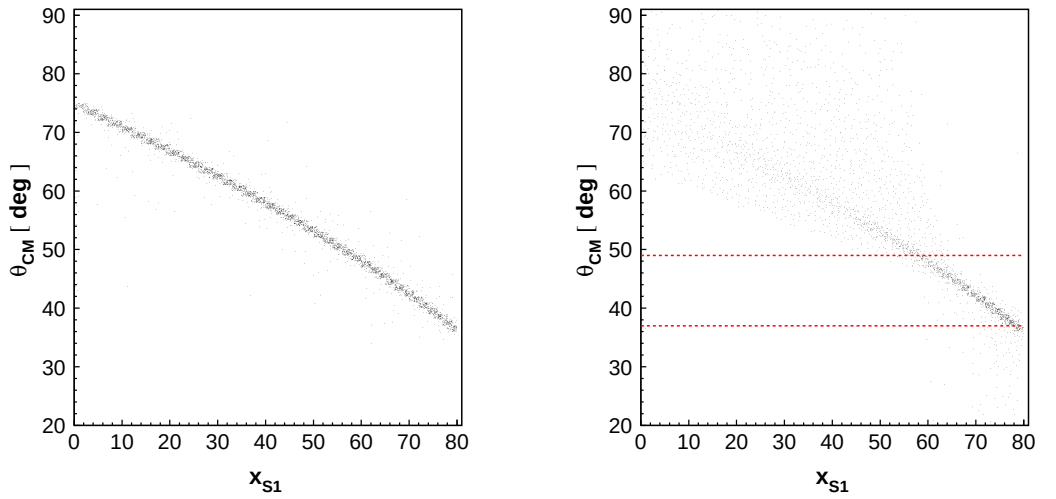

Figure 5.12: Relation between the centre-of-mass scattering angle and the position in the S1 detector for the $\vec{p}p \rightarrow pp$ elastic scattering at $p_{beam} = 2010$ MeV/c: (a) Monte-Carlo simulations, (b) experiment. Dotted lines are the boundaries of the practical range where the polarisation is calculated. The reason for a poor resolution outside this region is explained in the text.

Figure 5.12 depicts the relation between the centre-of-mass scattering angles

and the position in the S1 detector for the $\vec{p}p \rightarrow pp$ reaction at the beam momentum of p_{beam} = 2010 MeV/c. The scattering angles for which both protons may still be measured in coincidence by S1 and Si_{mon} ranges from around 35 to circa 75 degrees, as depicted in Figure 5.12.a. However, the practical partition of the CM scattering angles that may be used for the polarisation evaluation is squeezed to the range of (37;49) degrees (see Figure 5.12.b). This is due to the strong dependence of the cross section on the scattering CM angle and also due to the deterioration of the momentum determination for protons passing the dipole only on its edge. The experimental distribution of the Θ_{CM} angle as the function of the hit position in the S1 scintillator is shown in Figure 5.12.b.

This range was divided into three sections of 4 degrees width: (37;41), (41;45) and (45;49) degrees, choice which was dictated to facilitate an easy comparison with the data of the EDDA collaboration. As there were no EDDA measurements of the analysing power at the beam momentum p_{beam} = 2010 MeV/c, we used the average of the $\vec{p}p \rightarrow pp$ analysing powers measured at p_{beam} = 1995 MeV/c and p_{beam} = 2025 MeV/c [28] (see Figure 5.13). The obtained average values of the analysing power for the $\vec{p}p \rightarrow pp$ process at the beam momentum of p_{beam} = 2010 MeV/c are given in Table 5.3. It is worth noting that values of A_y for p_{beam} = 2010 MeV/c and p_{beam} = 2025 MeV/c are about the same within the statistical uncertainties.

i	Θ_i [°]	A_y
1	(37;41)	0.385 ± 0.013
2	(41;45)	0.376 ± 0.013
3	(45;49)	0.348 ± 0.013

Table 5.3: Analysing power values at a beam momentum of p_{beam} = 2010 MeV/c for the corresponding ranges of the CM scattering angle.

For the purpose of the analysis it is enough to know only the value of polarisation averaged over the time of measurement. However, in order to check the performance of the used polarimeters we have also performed the differential measurements of the degree of polarisation. The number of scatterings during spin up $N_+(\Theta)$ (scattering to the right side with respect to the polarisation plane) and spin down $N_-(\Theta)$ (scattering to the left side) has been determined for periods of 20 cycles, corresponding to circa 1.5 h of measurement. The values of N_+ and N_- have been normalized to the corresponding luminosities. We used the following formula to calculate the degree of polarisation:

$$P = \frac{\sum_{i=1}^{3} P(\Theta_i)}{3}, \tag{5.25}$$

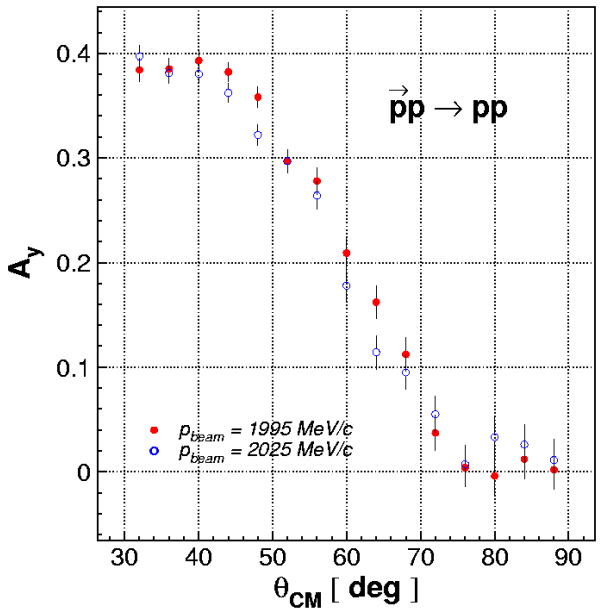

Figure 5.13: Analysing power for the $pp \to pp$ elastic scattering as measured by the EDDA collaboration at the beam momenta of p_{beam} = 1995 MeV/c and p_{beam} = 2025 MeV/c. In the COSY-11 experiment the beam momentum was set to p_{beam} = 2010 MeV/c, which is the middle of the range of beam momenta presented in this figure.

where

$$P(\Theta_i) = \frac{1}{A_y(\Theta_i)} \frac{N_+(\Theta_i) - N_-(\Theta_i)L_{rel}}{N_+(\Theta_i) + N_-(\Theta_i)L_{rel}}. \tag{5.26}$$

The ranges of Θ_i were chosen as indicated in Table 5.3. L_{rel} are the relative luminosities defined in equation 5.14, calculated separately for each time interval of polarisation averaging. The method of L_{rel} calculation has been described in Chapter 5.3.

The confrontation of the polarisation values determined with the COSY and COSY-11 polarimeters is shown in Figure 5.14. The open circles are the averaged values (averaged over spin up and down periods) as obtained by means of the COSY polarimeter, whereas the full circles show the results of the COSY-11 polarimeter.

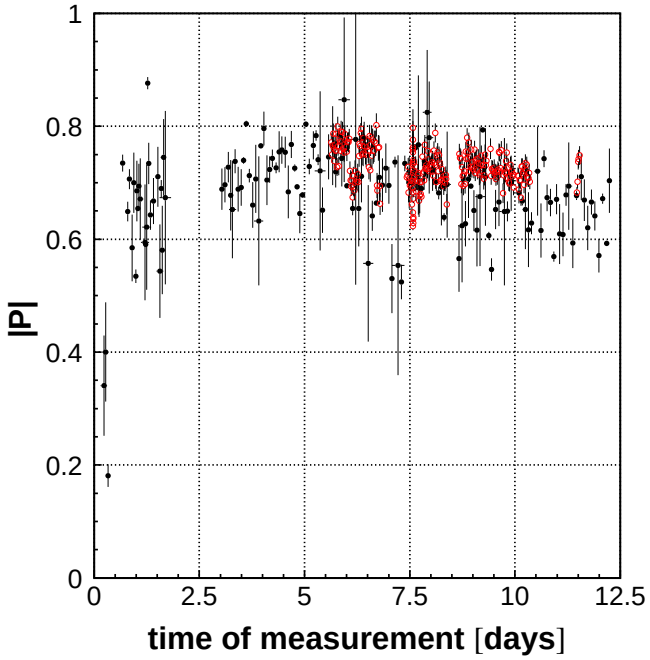

Figure 5.14: The degree of polarisation versus the time of the measurement as obtained during the experiment at the excess energy of Q = 10 MeV. Open circles denote results obtained by means of the COSY polarimeter [105], whereas the full points were determined using the COSY-11 setup.

It is worth mentioning that the presentation is only for the sake of the comparison between the results obtained by means of both abovementioned methods. Due to the technical problems the COSY polarimeter has been operating only for about 1/3 of the period of measurement. Over the most of this time the results from both polarimeters are in a good agreement. Low polarisation values in the first day of the run was due to the ongoing polarisation development by the accelerator team. Errors in the Figure 5.14 are the total errors, containing both statistical and systematic uncertainties.

Finally, based on the COSY-11 polarimeter the polarisation value for the full time of measurement has been computed and equals:

$$P = 0.680 \pm 0.007, \tag{5.27}$$

where the statistical error of the polarisation has been given. The systematic error of polarisation determination depends on the uncertainty of the analysing power $A_y(\Theta_i)$, the error of the relative luminosity L_{rel}, and the uncertainty of the scattering yields $N_{\pm}(\Theta_i)$. The systematic uncertainty of the $A_y(\Theta_i)$ equals

1.2% [28], the L_{rel} systematic error has been estimated in Section 5.3 to be about 1%, and the systematic uncertainties of the determination of $N_{\pm}(\Theta_i)$ is not greater than 1%. Applying the error propagation method for the systematic uncertainties to Equation 5.26 yields the following formula for the systematic uncertainty of the polarisation:

$$\Delta P = |\frac{\partial P}{\partial A_y}|\Delta A_y + |\frac{\partial P}{\partial L_{rel}}|\Delta L_{rel} + |\frac{\partial P}{\partial N_+}|\Delta N_+ + |\frac{\partial P}{\partial N_-}|\Delta N_-, \tag{5.28}$$

with

$$\begin{aligned}
\frac{\partial P}{\partial A_y} &= -\frac{1}{A_y^2}\frac{N_+ - L_{rel}N_-}{(N_+ + L_{rel}N_-)^2},\\
\frac{\partial P}{\partial L_{rel}} &= -\frac{1}{A_y}\frac{2N_+N_-}{(N_+ + L_{rel}N_-)^2},\\
\frac{\partial P}{\partial N_+} &= \frac{1}{A_y}\frac{2L_{rel}N_-}{(N_+ + L_{rel}N_-)^2},\\
\frac{\partial P}{\partial N_-} &= -\frac{1}{A_y}\frac{2L_{rel}N_+}{(N_+ + L_{rel}N_-)^2}.
\end{aligned} \tag{5.29}$$

Inserting the partial derivatives 5.29 into Equation 5.28 brings the overall systematic error of polarisation to $\Delta P = 8\%$.

5.4.2 Measurement at the excess energy of Q = 36 MeV

The detector setup EDDA and the method of the measurement of the degree of polarisation by means of this aparatus will be described.

For the polarisation monitoring during this run we made use of the EDDA detector setup [28]. This setup has commonly been used at the COSY synchrotron as an internal high-energy polarimeter since November 1997[6].

The schematic view of the EDDA detector is presented in Figure 5.15. Here we will only sketch the principle of the polarisation measurement. For more information about the detector components and for the explanation of detector's

[6] It is worth mentioning that apart from the monitoring of the polarisation at the COSY storage ring, EDDA is a well operating detector that performed many measurements of the $pp \to pp$ reactions. The EDDA collaboration measured the excitation functions $d\sigma/d\Omega(p_p, \Theta_{CM})$ for the unpolarised proton-proton elastic scattering [102]. Data has been gathered for 108 different proton kinetic energies, ranging from 240 MeV up to 2577 MeV, and are available at [106]. The EDDA group has also performed the measurements of the excitation function for the analysing power $A_N(p_p, \Theta_{CM})$ [28] for 77 different proton beam kinetic energies, ranging from 436 MeV up to 2492 MeV [107]. The centre-of-mass scattering angles of protons – Θ_{CM} – from 30^0 up to 90^0 have been covered. Measurements of the analysing power made use of the polarised CH_2 fiber target [108]. Recently, the spin correlation coefficients have been measured [109, 110] at 34 values of proton's kinetic energy ranging from 504 MeV up to 2493 MeV.

operation the reader is referred to [28, 111]. The EDDA detector consists of two cylindrical double layers that covers Θ_{CM} range from 30^0 to 90^0 for the $\vec{p}p \to pp$ reaction [28]. The construction of the detector is such that about 82% of the full solid angle are covered. The inner part is made of helically wound scintillator fibers of 2.5 mm diameter, while the outer part consists of 32 scintillator bars (B) surrounded by semirings (R). Target used in the experiment was an atomic beam target [108], which can operate in the polarised and unpolarised mode. In the measurements of the polarisation for COSY-11 run it has been operating in the latter mode.

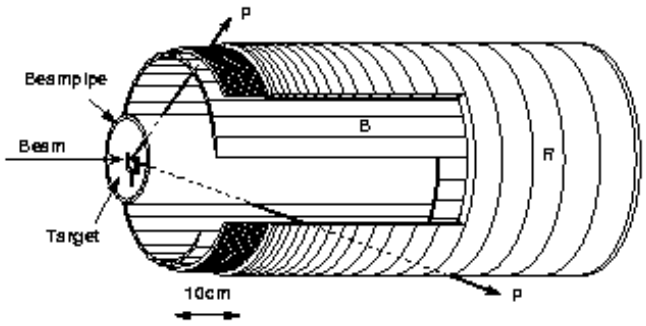

Figure 5.15: EDDA detector. Figure is adapted from [28].

Signals from the outgoing protons are registered in the detectors and subsequently reconstruction of the reaction vertex is performed with the resolution better than 2 mm in all three space directions [28]. Tracks of particles are reconstructed and the calculation of kinematical variables is possible. Next, the asymmetries ϵ for different Θ_{CM} angles can be calculated, using the Formula 5.19 with corrections for false asymmetries. Polarisation is then given by:

$$P = \frac{\epsilon}{A_y \cos(\phi)}, \tag{5.30}$$

where A_y is the analysing power for the $\vec{p}p \to pp$ reaction, determined in previous experiments with the EDDA detector setup, and ϕ is the azimuthal position of the hit in the detector.

As the acceptance of the EDDA detector for registering events scattered to the left and to the right side is large, it was possible to extract the information of the polarisations for spin up and spin down ($P^{\uparrow}$ and $P^{\downarrow}$, respectively) separately. It was found that [112]

$$\begin{aligned} P^{\uparrow} &= 0.642 \pm 0.004 \pm 0.008, \\ P^{\downarrow} &= 0.684 \pm 0.004 \pm 0.008, \end{aligned} \tag{5.31}$$

where the statistical and systematic errors are given, respectively. Thus, the average polarisation degree equals:

$$P = 0.663 \pm 0.003 \pm 0.008. \tag{5.32}$$

In our analysis we used this averaged value due to the reasons explained in Section 2.4. Determination of the polarisation degree for both spin orientations by the EDDA collaboration allowed us to estimate the error we made by this averaging. Similarly as during the measurement at Q = 10 MeV [105] this amounts to about ± 3% only.

5.5 Determination of the background free production rates for the $\vec{p}p \to pp\eta$ reactions

We show the way of the determination of the production yields used for reckoning the analysing power. Different methods at both excess energies have been used. Differences are pointed out in the text.

In Section 5.1 we presented the missing mass spectra for the $\vec{p}p \to pp\eta$ reaction at two excess energies: Q = 10 and 36 MeV. The histograms in Fig 5.8 include all events measured for both beam spin orientations. In order to determine A_y as a function of the centre-of-mass polar angle of the η meson emission – θ_η – we have to divide the events according to the θ_η range and consider events measured during spin up and down modes separately. Optimizing the statistics and the expected shape of the analysing power function, the range of the centre-of-mass polar angle of the η meson emission for both excess energies has been divided into four bins, and the results were integrated over the remaining four kinematical variables introduced in Section 2.3.

Here we will describe the methods of background subtraction from the missing mass spectra determined for both excess energies. We shall start with the description of the procedure for the excess energy Q = 36 MeV, where the shape of the background could be parameterized by a polynomial function of the second order. Then we will describe the more sophisticated methodology of the background subtraction at Q = 10 MeV.

5.5.1 Q = 36 MeV

In order to extract the production rates the missing mass spectra have been determined as a function of the cosine of the centre-of-mass emission angle of the η meson, for spin up and down modes separately. The values of A_y will be derived in accordance with the Madison convention quoted in Section 2.2. Subsequently we will apply the notation defined in Section 2.4 with $N_+^\uparrow$ and $N_-^\downarrow$ denoting the

production yields to the left side with respect to the polarisation plane during spin up and down modes, respectively.

An exemplary spectrum of the missing mass for spin up mode and $\cos\theta_\eta \in [0.5, 1]$ is presented in Figure 5.16. Next, we made the assumption that the background[7] shape may be described by a polynomial of second order, and the function

$$F_{backgr}(mm) = a + b\ mm + c\ mm^2, \tag{5.33}$$

where mm stands for the missing mass, has been fitted to the experimental histograms in the ranges outside the η peak with a, b, and c treated as free parameters.

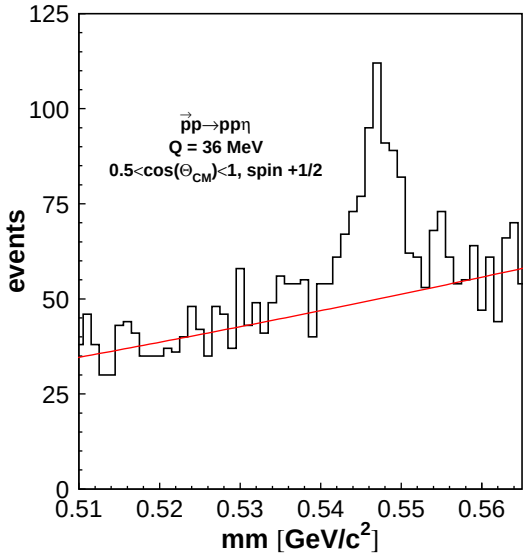

Figure 5.16: A histogram of missing mass for the $\vec{p}p \to pp\eta$ reaction at Q = 36 MeV. Spectrum for spin up mode and $\cos\theta_\eta \in [0.5, 1]$ is shown.

Afterwards, the background evaluated in such a way has been subtracted from the experimental spectra for each histogram separately. The resulting background-free histograms of missing mass are presented in Figures 5.17.a-h as full circles.

Due to low acceptance of the COSY-11 system for the production of the η meson in the backward directions in the centre-of-mass system at the excess energy of Q = 36 MeV (missing mass bin for $\cos\theta_\eta \in [-1, -0.5]$), and as a consequence of the problems with the background subtraction for this bin, resulting in the huge systematical errors, we decided to omit this bin from further analysis and determine the analysing powers at this excess energy for $\cos\theta_\eta$ larger than -0.5.

[7]Originating from the multipionic reactions: $pp \to pp2\pi^0$, $pp \to pp\pi^+\pi^-$, $pp \to pp3\pi^0$, $pp \to pp\pi^0\pi^+\pi^-$, $pp \to pp4\pi^0$, $pp \to pp2\pi^0\pi^+\pi^-$, and $pp \to pp2\pi^+2\pi^-$.

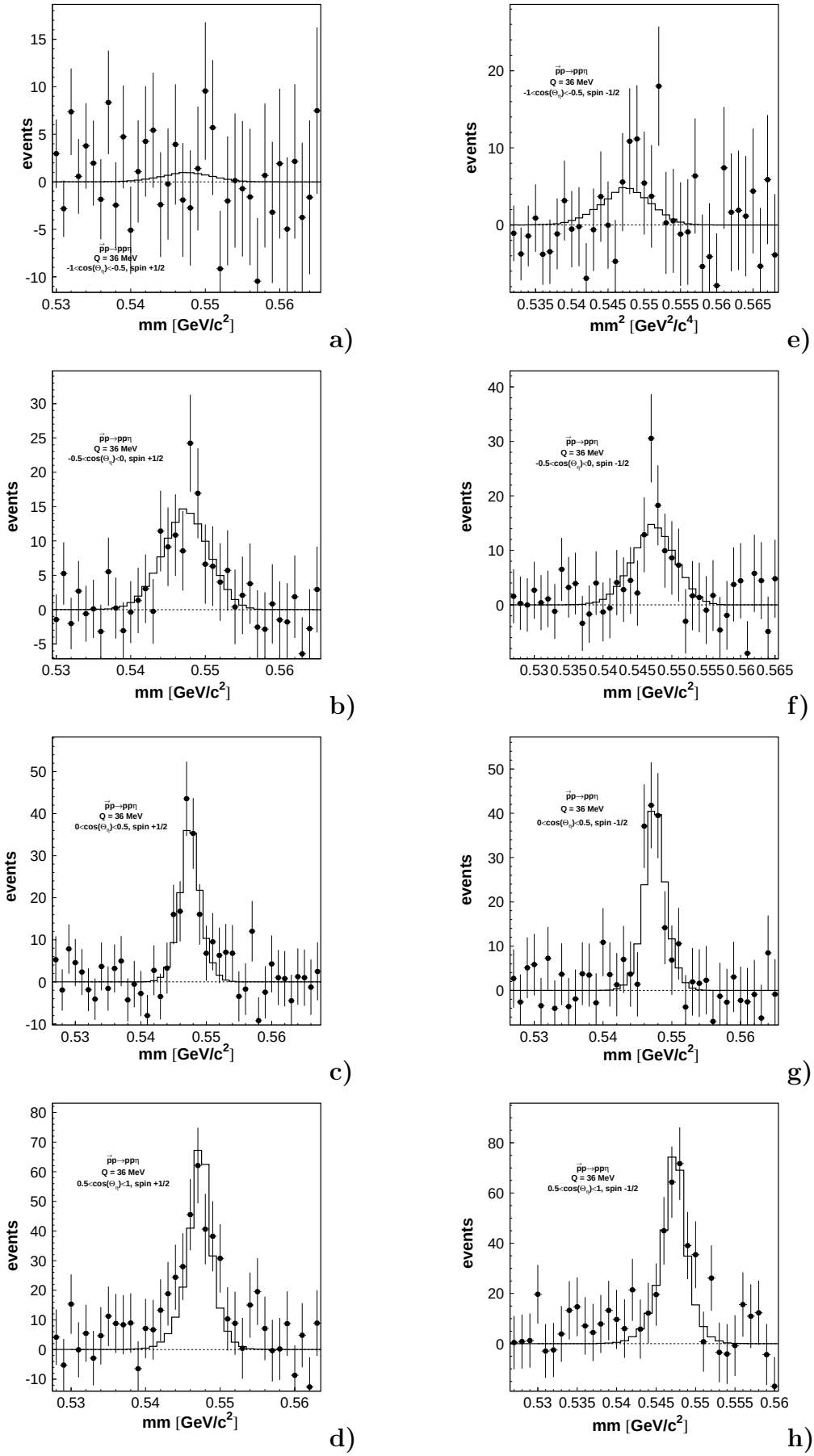

Figure 5.17: Missing mass spectra for the $\vec{p}p \to pp\eta$ reaction at Q = 36 MeV for

Subsequently, the simulations of the shape of the missing mass spectrum for different ranges of $\cos\theta_\eta$ have been done using a program based on the GEANT3 code [101]. This program contains the exact geometry of the COSY-11 detector system as well as the precise map of the magnetic field of the dipole magnet. Also the momentum and spatial beam spreads, multiple scattering, and other instrumentation effects have been taken into account. Generated events which fulfilled conditions equivalent to the experimental trigger have been analysed in the same way as the experimental data and corresponding histograms for the $pp \to pp\eta$ reaction have been determined resulting in three missing mass functions $g_{pp\to pp\eta}(mm, \cos\theta_\eta)$, where mm denotes the missing mass. Further, to the experimental histograms presented in Figure 5.17 the functions

$$G^{\uparrow(\downarrow)}(mm, \cos\theta_\eta) = \gamma^{\uparrow(\downarrow)}(\cos\theta_\eta) g_{pp\to pp\eta}(mm, \cos\theta_\eta) \tag{5.34}$$

have been fitted, for spin up and down separately. Note that the functions $g_{pp\to pp\eta}(mm, \cos\theta_\eta)$ describing the missing mass shape are the same for spin up and down modes, and vary only with the $\cos\theta_\eta$. On the other hand, the free parameters of the fit – $\gamma^{\uparrow(\downarrow)}(\cos\theta_\eta)$ – might be different, depending on the spin orientation. The number of identified η mesons for each $\cos\theta_\eta$ bin and for spin up and down modes have been calculated from the determined $\gamma^{\uparrow(\downarrow)}(\cos\theta_\eta)$ parameters, namely:

$$N^{\uparrow(\downarrow)}_{+(-)}(\cos\theta_\eta) = \gamma^{\uparrow(\downarrow)}(\cos\theta_\eta) \int_0^{mm_{max}} g_{pp\to pp\eta}(mm, \cos\theta_\eta) d(mm). \tag{5.35}$$

The statistical errors $\sigma(N^{\uparrow(\downarrow)}_{+(-)})(\cos\theta_\eta)$ have been estimated based on the formula:

$$\sigma(N^{\uparrow(\downarrow)}_{+(-)}(\cos\theta_\eta)) = \sigma(\gamma^{\uparrow(\downarrow)}(\cos\theta_\eta)) \int_0^{mm_{max}} g_{pp\to pp\eta}(mm, \cos\theta_\eta) d(mm), \tag{5.36}$$

where $\sigma(\gamma^{\uparrow(\downarrow)}(\cos\theta_\eta))$ are the estimates of the $\gamma^{\uparrow(\downarrow)}(\cos\theta_\eta)$ parameters uncertainties (standard deviations) determined by means of the MINUIT minimization package [113]. Results are presented in Table 5.4.

$\cos\theta_\eta$	$N^{\uparrow}_{+}(\cos\theta_\eta)$	$N^{\downarrow}_{-}(\cos\theta_\eta)$
$[-0.5; 0)$	**103 ± 16**	**100 ± 18**
$[0; 0.5)$	**144 ± 16**	**153 ± 18**
$[0.5; 1]$	**259 ± 24**	**296 ± 28**

Table 5.4: Number of identified η mesons in the $\vec{p}p \to pp\eta$ reaction at the excess energy of Q = 36 MeV as the function of the spin orientation and the cosine of the centre-of-mass polar angle of the η meson emission – θ_η.

5.5.2 Q = 10 MeV

At this excess energy the upper-energetic tale of the η peak disperses to the edge of the kinematical limit, as presented in Figure 5.18. This makes the identification of the upper part of the multipionic background more inacurate, and hence the method of the background subtraction similar to the one presented in 5.5.1 would be biased by the larger systematical uncertainties.

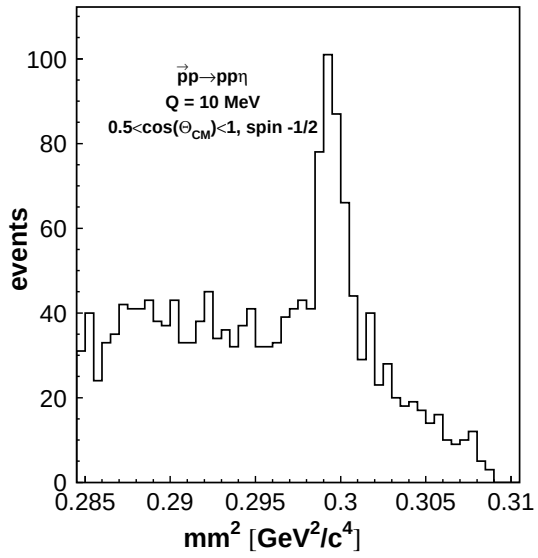

Figure 5.18: A histogram of missing mass squared for the $\vec{p}p \to pp\eta$ reaction at Q = 10 MeV for selected $\cos\theta_\eta$ range as measured during spin down mode.

Therefore, to separate the actual production rates from the background, the reactions with multipionic production as well as the events with the η meson production have been simulated in order to reconstruct the shape of the missing mass spectra. For simulations, the same program as the one described in Section 5.5.1 has been used, but this time apart from the $pp \to pp\eta$ reaction also the background reactions like $pp \to pp\ 2\pi, 3\pi, 4\pi$ have been generated.

In order to perform the credible comparison between experiment and the simulations, in the Monte-Carlo calculations the geometry of drift chambers, as well as the position and geometrical parameters of the target have been fixed to be the same as for the experimental data analysis.

Let the $f_{pp\to pp2\pi}(mm^2, \sigma_p, \Delta p, \cos\theta_\eta)$, $f_{pp\to pp3\pi}(mm^2, \sigma_p, \Delta p, \cos\theta_\eta)$, $f_{pp\to pp4\pi}(mm^2, \sigma_p, \Delta p, \cos\theta_\eta)$, and $f_{pp\to pp\eta}(mm^2, \sigma_p, \Delta p, \cos\theta_\eta)$ denote the generated background functions for double, triple, fourfold pion production and for the η production, respectively, where mm^2 stands for the missing mass

squared, whereas σ_p and Δp are the momentum spread and the deviation of the beam momentum from its nominal value. The functions of the type:

$$\begin{aligned} f^{\uparrow(\downarrow)}(mm^2,\sigma_p,\Delta p,\cos\theta_\eta) = \alpha^{\uparrow(\downarrow)}(\cos\theta_\eta)\ f_{pp\to pp2\pi}(mm^2,\sigma_p,\Delta p,\cos\theta_\eta) + \\ \beta^{\uparrow(\downarrow)}(\cos\theta_\eta)\ f_{pp\to pp3\pi}(mm^2,\sigma_p,\Delta p,\cos\theta_\eta) + \\ \gamma^{\uparrow(\downarrow)}(\cos\theta_\eta)\ f_{pp\to pp4\pi}(mm^2,\sigma_p,\Delta p,\cos\theta_\eta) + \\ \delta^{\uparrow(\downarrow)}(\cos\theta_\eta)\ f_{pp\to pp\eta}(mm^2,\sigma_p,\Delta p,\cos\theta_\eta), \end{aligned} \tag{5.37}$$

with $\alpha(\cos\theta_\eta),\ldots\delta(\cos\theta_\eta)$ as free parameters have been fitted to the experimental spectra of the missing mass squared using the MINUIT [113] minimization package. For Q = 10 MeV also the bin for $\cos\theta_\eta \in [-1,-0.5]$ has been considered in the analysis, as the statistic was sufficient to extract the numbers of events also in this particular bin. The fit has been performed simultaneously to 8 histograms of missing mass squared, each for different spin-$\cos\theta_\eta$ range configuration. It is important to point out that for a given $\cos\theta_\eta$ bin the shapes of the generated missing mass histograms, i.e. the functions $f_{pp\to pp2\pi}(mm^2,\sigma_p,\Delta p,\cos\theta_\eta)$, $f_{pp\to pp3\pi}(mm^2,\sigma_p,\Delta p,\cos\theta_\eta)$, $f_{pp\to pp4\pi}(mm^2,\sigma_p,\Delta p,\cos\theta_\eta)$ and $f_{pp\to pp\eta}(mm^2,\sigma_p,\Delta p,\cos\theta_\eta)$ depend only on the width of the momentum distribution σ_p and the shift from the optimal beam momentum Δp. The χ^2 of the fit has been minimized as a function of 34 parameters: amplitudes $\alpha(\theta_i)$,...,$\delta(\theta_i)$ of the generated background and signal reactions (4 for each histogram) and 2 parameters responsible for the spread and the absolute value of the beam momentum. However, it is worth noting that altogether the histograms contained 480 points.

In Fig. 5.19 the missing masses for the individual $\cos\theta_\eta$ subranges are shown. Full dots denote the experimental data, the shaded parts of the histograms depict the multipionic background, whereas the solid line represents the best fit of the Monte-Carlo data to the experimental spectra. The minimum value of χ^2 for this fit divided by the number of degrees of freedom was determined to be 1.6.

Numbers of η mesons $N^{\uparrow(\downarrow)}_{+(-)}(\cos\theta_\eta)$ for the individual ranges of $\cos\theta_\eta$ for spin up and down cycles have been calculated as:

$$N^{\uparrow(\downarrow)}_{+(-)}(\cos\theta_\eta) = \delta^{\uparrow(\downarrow)}(\cos\theta_\eta)\int_0^{mm^2_{max}} f_{pp\to pp\eta}(mm^2,\sigma_p,\Delta p,\cos\theta_\eta)d(mm^2). \tag{5.38}$$

The statistical errors $\sigma(N^{\uparrow(\downarrow)}_{+(-)}(\cos\theta_\eta))$ have been estimated based on the formula analogous to Equation 5.36:

$$\sigma(N^{\uparrow(\downarrow)}_{+(-)}(\cos\theta_\eta)) = \sigma(\delta^{\uparrow(\downarrow)}(\cos\theta_\eta))\int_0^{mm^2_{max}} f_{pp\to pp\eta}(mm^2,\sigma_p,\Delta p,\cos\theta_\eta)d(mm^2), \tag{5.39}$$

where $\sigma(\delta^{\uparrow(\downarrow)}(\cos\theta_\eta))$ are again the estimates of the standard deviations of the $\delta^{\uparrow(\downarrow)}(\cos\theta_\eta)$ parameters. The obtained number of η mesons per $\cos\theta_\eta$ range are quoted in Table 5.5.

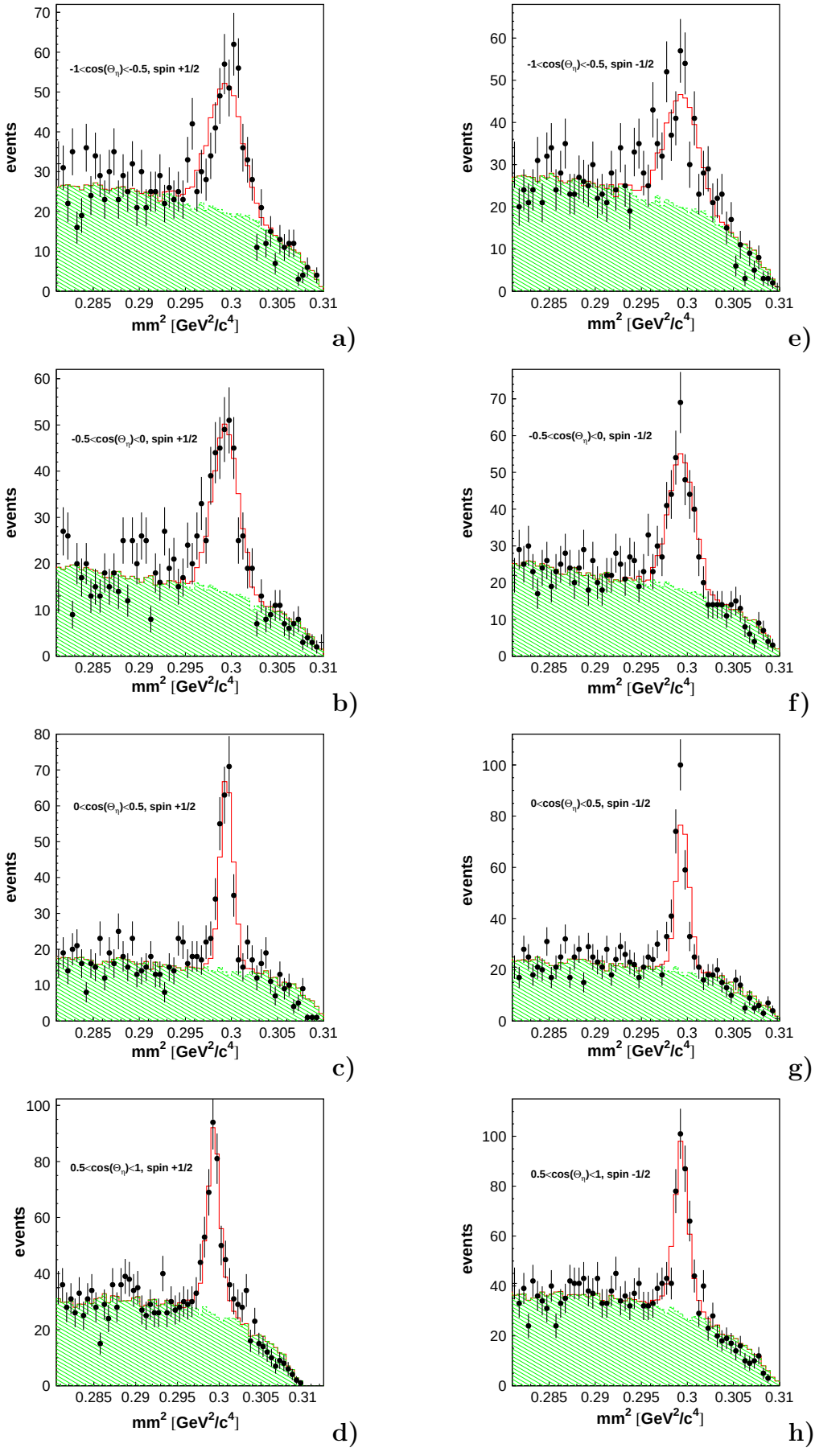

Figure 5.19: Missing mass spectra for different ranges of $\cos\theta_\eta$ for spin up (a–d)

$\cos\theta_\eta$	$N_+^{\uparrow}(\cos\theta_\eta)$	$N_-^{\downarrow}(\cos\theta_\eta)$
$[-1;-0.5)$	**306 ± 27**	**250 ± 26**
$[-0.5;0)$	**267 ± 22**	**260 ± 24**
$[0;0.5)$	**198 ± 18**	**208 ± 19**
$[0.5;1]$	**279 ± 23**	**286 ± 25**

Table 5.5: Number of registered η mesons as the function of the cosine of the centre-of-mass η emission angle (θ_η) and spin orientation of the beam.

In the table only the statistical uncertainties are presented. The systematic errors for the extraction of number of events have been estimated by comparison of the values in Table 5.5 with the number of events determined using the other method, namely assuming that the background is linear in the range of missing mass peak. In such a way for each $\cos\theta_\eta$ bin we obtained values which differed from the numbers quoted in Table 5.5 by no more than 1.5%. This value we assigned to the systematic error of $\mathrm{N}^{\uparrow(\downarrow)}(\cos\theta_\eta)$ at both excess energies.

5.6 Results – the analysing power

The results of the analysing power determination are summarized in the table and in the figures.

Having presented the methodology of L_{rel}, P and $N_{+(-)}^{\uparrow(\downarrow)}(\cos\theta_i)$ determination we can now equate the analysing power for both excess energies. For this purpose we shall exploit Formula 2.23, which reads:

$$A_y(\cos\theta_\eta) = \frac{1}{P}\frac{N_+^{\uparrow}(\cos\theta_\eta) - L_{rel}N_-^{\downarrow}(\cos\theta_\eta)}{N_+^{\uparrow}(\cos\theta_\eta) + L_{rel}N_-^{\downarrow}(\cos\theta_\eta)}. \tag{5.40}$$

Relative luminosities can be found in Table 5.2, average polarisations have been determined in Section 5.4, and finally Tables 5.4 and 5.5 provide the values of background free productions rates for Q = 36 and 10 MeV, respectively. The analysing powers for the $\vec{p}p \to pp\eta$ reaction which were calculated basing on these numbers are shown in 3$^{\mathrm{rd}}$ column of Table 5.6. Values presented in the 4$^{\mathrm{th}}$ and 5$^{\mathrm{th}}$ column of this table are the mean values over a $\cos\theta_\eta$ bin of the theoretical predictions for A_y according to the models with the dominance of the pseudoscalar and vector meson exchanges, respectively. In the derivation we took advantage of the fact that for an isotropic distribution of the differential cross section $\frac{d\sigma}{d\theta}(\theta) = \mathrm{const}$, the average analysing power over an angular range θ is an arithmetical average of the analysing powers for the individual θ_n subranges of θ – for proof see Appendix B.

Q[MeV]	$\cos\theta_\eta$	$A_y(\cos\theta_\eta)$	$A_y^{pseud}(\cos\theta_\eta)$	$A_y^{vec}(\cos\theta_\eta)$
10	$[-1;-0.5)$	$\mathbf{0.163 \pm 0.099 \pm 0.022}$	0.133	-0.170
	$[-0.5;0)$	$\mathbf{0.035 \pm 0.091 \pm 0.012}$	0.067	-0.092
	$[0;0.5)$	$\mathbf{-0.021 \pm 0.095 \pm 0.011}$	-0.082	0.092
	$[0.5;1]$	$\mathbf{-0.003 \pm 0.088 \pm 0.009}$	-0.144	0.170
36	$[-1;-0.5)$	—	0.147	-0.001
	$[-0.5;0)$	$\mathbf{0.039 \pm 0.179 \pm 0.012}$	0.046	0.000
	$[0;0.5)$	$\mathbf{-0.029 \pm 0.122 \pm 0.010}$	-0.062	0.000
	$[0.5;1]$	$\mathbf{-0.084 \pm 0.100 \pm 0.011}$	-0.154	0.001

Table 5.6: Analysing power for the $\vec{p}p \to pp\eta$ reaction determined at the excess energies Q = 10 and 36 MeV. A_y^{pseud} and A_y^{vec} are the theoretical predictions according to the models with the pseudoscalar and vector meson exchange dominance, described in Section 3.1. The first quoted error is statistical, whereas the second one is systematic. The estimation of the systematic errors will be given in the next section.

Statistical uncertainties of A_y were calculated according to the rule of error propagation, and the following formula has been applied for their determination:

$$\sigma(A_y) = \sqrt{\left(\frac{\partial A_y}{\partial L_{rel}}\right)^2 \sigma^2(L_{rel}) + \left(\frac{\partial A_y}{\partial P}\right)^2 \sigma^2(P) + \left(\frac{\partial A_y}{\partial N_+^\uparrow}\right)^2 \sigma^2\left(N_+^\uparrow\right) + \left(\frac{\partial A_y}{\partial N_-^\downarrow}\right)^2 \sigma^2\left(N_-^\downarrow\right)} \tag{5.41}$$

with

$$\begin{aligned}
\frac{\partial A_y}{\partial L_{rel}} &= -\frac{1}{P}\frac{2N_+^\uparrow N_-^\downarrow}{\left(N_+^\uparrow + L_{rel}N_-^\downarrow\right)^2},\\
\frac{\partial A_y}{\partial P} &= -\frac{1}{P^2}\frac{N_+^\uparrow - L_{rel}N_-^\downarrow}{\left(N_+^\uparrow + L_{rel}N_-^\downarrow\right)^2},\\
\frac{\partial A_y}{\partial N_+^\uparrow} &= \frac{1}{P}\frac{2L_{rel}N_-^\downarrow}{\left(N_+^\uparrow + L_{rel}N_-^\downarrow\right)^2},\\
\frac{\partial A_y}{\partial N_-^\downarrow} &= -\frac{1}{P}\frac{2L_{rel}N_+^\uparrow}{\left(N_+^\uparrow + L_{rel}N_-^\downarrow\right)^2}.
\end{aligned} \tag{5.42}$$

It is worth mentioning, that the partial contributions to the overall statistical error from the L_{rel} and P uncertainties were about two orders of magnitude smaller than the contributions from $N_+^\uparrow$ and $N_-^\downarrow$ uncertainties.

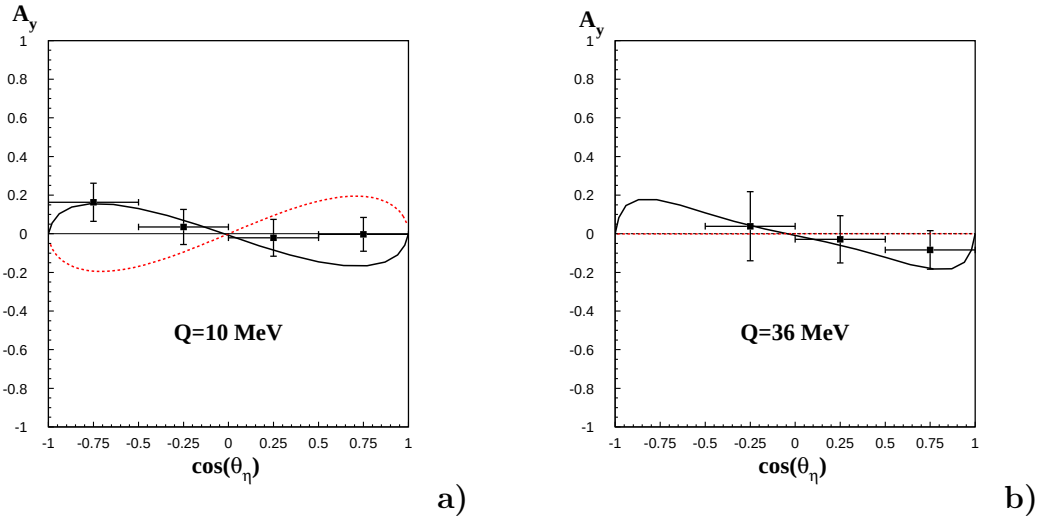

Figure 5.20: Analysing power for the $\vec{p}p \to pp\eta$ reaction as function of the cosine of polar emission angle of the η meson in the centre-of-mass system for Q = 10 MeV (a) and Q = 36 MeV (b). Full lines are the predictions based on the pseudoscalar meson exchange model [11] whereas the dotted lines represent the results of the calculations based on the vector meson exchange [14]. In the right panel the predictions of the vector meson exchange dominance model are consistent with zero. Error bars in both panels of the figure show the statistical uncertainties only. Systematic errors are estimated in next section.

The analysing power from Table 5.6 along with statistical errors and the models predictions for Q = 10 and 36 MeV are depicted in Figure 5.20.a and 5.20.b, respectively.

5.7 Systematic uncertainties of the analysing power

We estimate the systematic uncertainties for the analysing power at both excess energies.

The physical quantities needed to calculate the analysing power A_y, according to the Equation 5.40, are the average beam polarisation P, the relative luminosities between spin up and down modes L_{rel}, and the production rates $N^{\uparrow(\downarrow)}$ for spin up and down, respectively.

The systematic uncertainty of polarisation for Q = 10 MeV has been estimated in Section 5.4.1 and equals ΔP(Q = 10 MeV) = 0.055. The same quantity for the excess energy of Q = 36 MeV was found to be ΔP(Q = 36 MeV) = 0.008 [112].

Differences in the systematic uncertainties between the measurements are due to the fact that different detector setups were used in the determination of the degree of polarisation. The systematic uncertainty of the relative luminosity has been found in Section 5.3 and equals $\Delta L_{rel} = 1\%$ for both excess energies. Finally, the systematic error of the determination of the production rates has been estimated in Section 5.5.2 and amounts to $\Delta N^{\uparrow(\downarrow)}_{+(-)} = 1.5\%$, the same value for both excess energies.

The values quoted above have been used to determine the overall systematic uncertainty of A_y. The contributions from different error sources were added analogously to Formula 5.28, exchanging $P \longleftrightarrow A_y$, $N_+ \longleftrightarrow N^{\uparrow}_+$ and $N_- \longleftrightarrow N^{\downarrow}_-$. This procedure yielded the values of the systematic uncertainties of A_y quoted in Table 5.6.

At this point it is worth mentioning that the beam misaligment between spin up and down modes has no significant influence upon the determination of $N^{\uparrow(\downarrow)}_{+(-)}$ values. Monte-Carlo simulations analogous to the ones presented in Sections 5.3 and 5.4.1 have been performed and the systematic error of $N^{\uparrow(\downarrow)}_{+(-)}$ originating from the beam misaligment was found to be negligible in comparison with $\Delta N^{\uparrow(\downarrow)}_{+(-)}$.

It has also been confirmed that the systematic uncertainty of $N^{\uparrow(\downarrow)}_{+(-)}$ originating from different binnings of histograms from Figures 5.17 and 5.19 is negligible with comparison to the quoted 1.5% uncertainty originating from the determination of $N^{\uparrow(\downarrow)}_{+(-)}$ using different background models.

Chapter 6

Interpretation of the experimental results

6.1 Test of the predictions for $\mathbf{A}_y$

Using the statistical inference it is shown that the derived values of the analysing power disagree with the predictions of the vector meson exchange models at a significance level of $\alpha = 0.006$. The predictions of the pseudoscalar meson exchange dominance model are in line with the data at a significance level of of 0.81. The values of the amplitude of the analysing power are extracted at both excess energies.

In order to determine the statistical significance of our results we have compared the predictions of the models with the experimentally determined values of the analysing power for both excess energies. For both theoretical hypotheses a value of the χ^2 have been calculated according to the formula:

$$\chi^2 = \sum_{i=1}^{7} \left(\frac{A_{y,i}^{model} - A_{y,i}^{exp}}{\sigma\left(A_{y,i}^{exp}\right)} \right)^2 , \tag{6.1}$$

with $\sigma\left(A_{y,i}^{exp}\right)$ denoting the experimental uncertainty of the $A_{y,i}^{exp}$ value and i enumerating the points for the excess energies of Q = 10 and 36 MeV. Altogether there are 7 experimental points determined in both experiments. The $A_{y,i}^{model}$ are the values of the analysing power calculated according to the pseudoscalar and vector meson exchange models, averaged over the same angular divisions as was performed for the experimental data. The value of the analysing power for an angular range θ has been taken as the mean value of the individual analysing powers predicted for this range (see Appendix B). These values along with the experimental values of $A_{y,i}^{exp}$ are quoted in Table 5.6.

We have obtained the values of χ^2 equal to 3.78 and 19.32 for the pseudoscalar and vector meson exchange models, respectively. Taking into account that there are 7 degrees of freedom, the reduced value of the χ^2 for the pseudoscalar meson

exchange model was found to be $\bar{\chi}^2_{psd} = 0.54$, which corresponds to a significance level $\alpha_{psd} = 0.81$, whereas for the vector meson exchange model $\bar{\chi}^2_{vec} = 2.76$ resulting in a significance level $\alpha_{vec} = 0.006$ [1].

Assuming that the predictions of the vector meson exchange model regarding the shape of the angular dependence of the analysing power are correct, we have also performed the χ^2 test in order to determine the amplitude of the angular dependence of the analysing power. As mentioned in Section 3.1, the angular distribution of the analysing power may be parametrized with the following equation:

$$A_y\,(Q, \theta_\eta) = A_y^{max,vec}(Q) \sin 2\theta_\eta, \tag{6.2}$$

where the amplitude $A_y^{max,vec}(Q)$ is a function of the excess energy Q, and its energy dependence is shown in Figure 3.7 as the dotted line. A fit of the abovementioned function to the experimental results has been performed at both excess energies, with $A_y^{max,vec}$ as the only free parameter. We have found $A_y^{max,vec} = -0.071 \pm 0.058$ for Q = 10 MeV, and $A_y^{max,vec} = -0.081 \pm 0.091$ for Q = 36 MeV. The best fit functions of Equation 6.2 to the experimental data are presented in Figure 6.1.

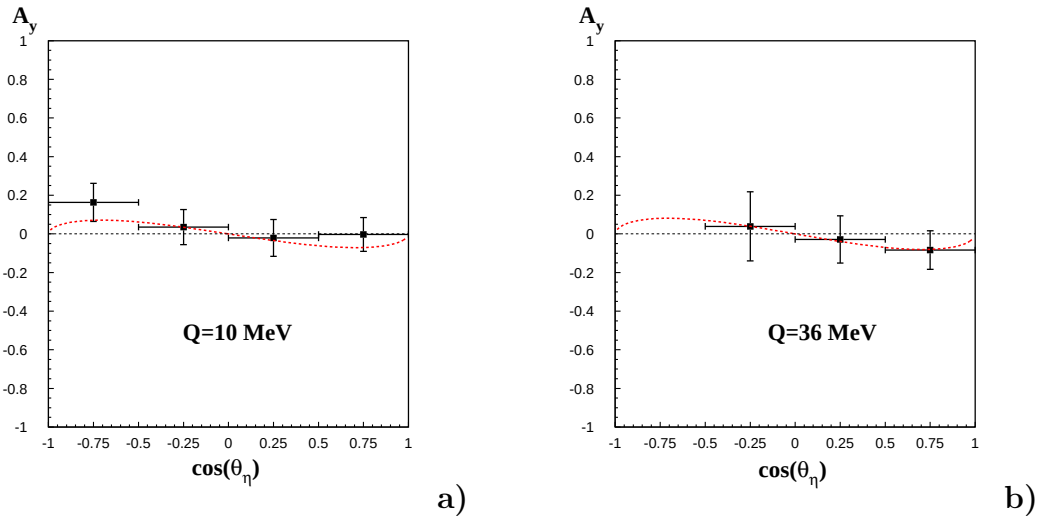

Figure 6.1: Fit of the function $A_y(Q, \theta_\eta) = A_y^{max,vec}(Q) \sin 2\theta_\eta$ to the experimental results of analysing power for Q = 10 MeV (a) and Q = 36 MeV (b). The purpose of the fit was to extract the amplitude $A_y^{max,vec}$ for both excess energies.

Similar studies have been performed for the pseudoscalar meson exchange model. Although authors of this model do not give an explicit analytical prescription of the analysing power's angular dependence, comparison of the predictions for different excess energies leads to the conclusion that they do not differ

[1] The significance levels as the functions of the $\bar{\chi}^2$ values have been taken from [114]

much in shape. This may be seen in Figure 6.2.a, where the theoretical line for Q = 10 MeV is compared with the theoretical line for Q = 25 MeV. The latter curve has been normalized such that the difference between the predictions for these two excess energies is at its smallest. One can see in Figure 6.2.a, that the differences are indeed much smaller than the experimental accuracy of the determined analysing power. Therefore, we may assume that the pseudoscalar meson exchange model's predictions with respect to the analysing power have the same shape for all excess energies within the close-to-threshold region, and only the amplitude of this function varies for different excess energies. Thus, by analogy to Equation 6.2 we may write that

$$A_y(Q, \theta_\eta) = A_y^{max,psd}(Q) f(\theta_\eta), \tag{6.3}$$

where $f(\theta_\eta)$ is the function presented in Figure 6.2.a.

Based on this assumption we have performed a fit of the predicted theoretical functions for Q = 10 and 36 MeV to the experimental data at corresponding excess energies, minimising the χ^2 value with $A_y^{max,psd}$ varied as a free parameter. The amplitudes $A_y^{max,psd} = -0.074 \pm 0.062$ for Q = 10 MeV and $A_y^{max,psd} = -0.096 \pm 0.108$ for Q = 36 MeV have been derived.

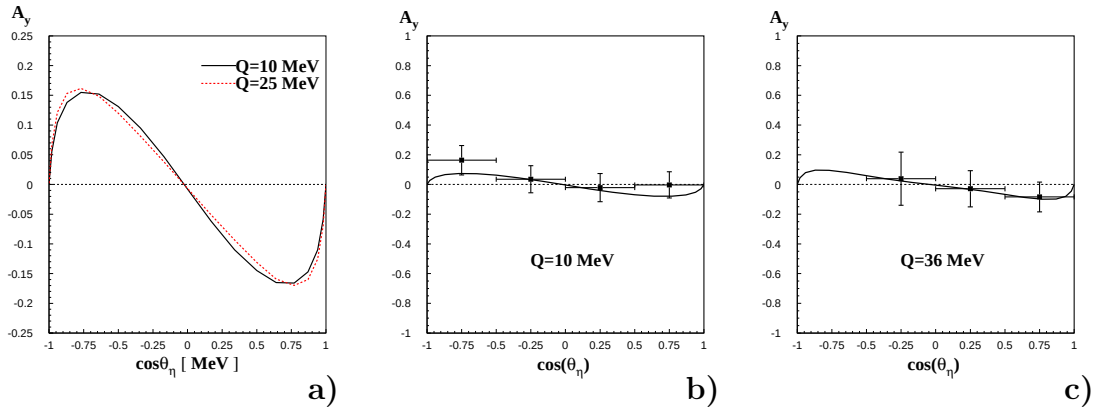

Figure 6.2: (a) Comparison of the shape of the angular distribution of A_y based on the pseudoscalar meson exchange dominance model for arbitrarily chosen Q = 10 MeV and 25 MeV. Predictions at Q = 25 MeV were normalized to those of Q = 10 MeV. The numerical values of $A_y(Q, \theta_\eta)$ have been made available by the authors of the pseudoscalar meson exchange dominance model [11, 115]. (b) Fit of the A_y function for Q = 10 MeV to the experimental data. (c) Similar fit, but for excess energy of Q = 36 MeV.

The values of the analysing power amplitudes together with the theoretical predictions are depicted in Figure 6.3.a for the pseudoscalar meson exchange model and in Figure 6.3.b for the vector meson dominance model.

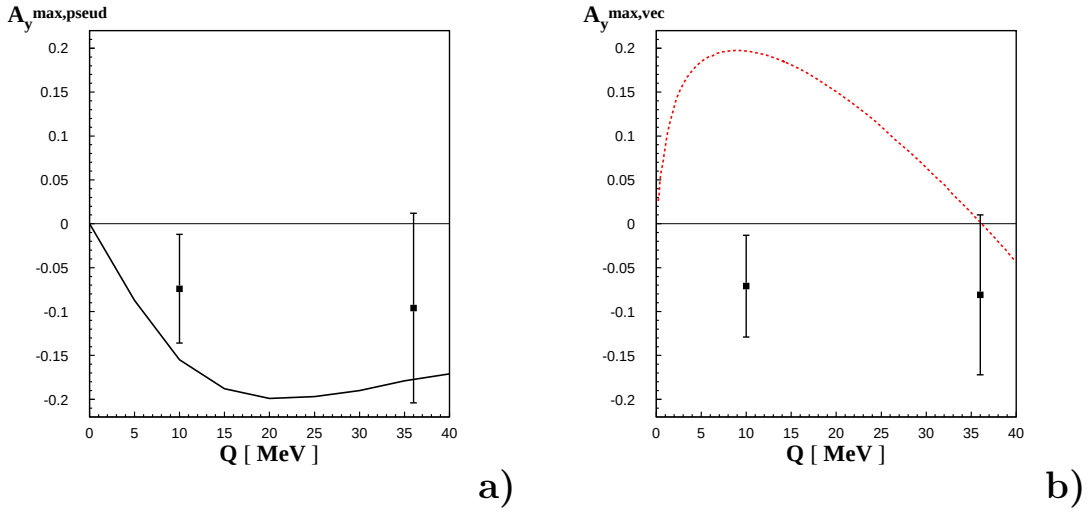

Figure 6.3: Theoretical predictions for the amplitudes of the analysing power angular dependence in the close-to-threshold region confronted with the amplitudes determined in the experiments at Q = 10 and Q = 36 MeV. The solid line in Figure (a) shows the prediction based on the pseudoscalar meson exchange dominance model [11], while the dotted line in Figure (b) corresponds to the prediction of the vector meson dominance model of reference [14].

One can see in this figure that although the amplitude of the vector meson exchange model for the excess energy of Q = 36 MeV lies within about one standard deviation from the experimental result, the predicted A_y^{max} for Q = 10 MeV is 4.3 σ away from the data point. In the pseudoscalar meson exchange dominance model predictions of A_y^{max} lie within one standard deviation from the experimental data.

Another observation that can be made from the results shown in Figure 6.3 is that the extracted A_y^{max} for different models are of about the same value. This is due to the fact that the pseudoscalar and vector meson exchange models predictions do not differ much in the shapes of the angular dependencies of the analysing power.

6.2 Mechanism of the η meson production in nucleon-nucleon collisions

The most probable mechanism of the η meson production in proton-proton collisions is presented.

As pointed out in Section 3.1.1, it has been established by the theoretical

analysis of the data from the total cross section measurements for the $pp \to pp\eta$ reaction, that the resonant current constitutes the main contribution to the production mechanism of the η meson in proton-proton collisions in the close-to-threshold energy region. It appears that amongst the available resonances the $S_{11}(1535)$ resonance plays the most important role as an intermediate state. Excitation of the proton to this resonance may proceed by either one of the light pseudoscalar or vector meson exchanges. However, as far as only the data on the total cross section are concerned an univocal statement cannot be made on which out of the spectrum of possible mesons gives rise to the $S_{11}(1535)$ resonance. Here, the possible particles to be exchanged are the π, η, ρ, and ω mesons.

Some limitations to the models have been made by the measurements of the total cross sections for the quasi-free $pn \to pn\eta$ reaction [13]. It has been found that the $\sigma(pn \to pn\eta)/\sigma(pp \to pp\eta)$ ratio is rather constant in the wide excess energy range from 16 to 109 MeV, and equals about 6.5. From such strong isospin dependence of the production amplitudes it has been deduced that the excitation of the $S_{11}(1535)$ resonance proceeds via the exchange of the isovector mesons, hence this discovery discarded the η and ω mesons as possible intermediate particles. Therefore, there remained two possible particles relevant to excite the S_{11} resonance: the π meson, belonging to the light pseudoscalars meson's nonet and the ρ meson – a member of the light vector meson's nonet.

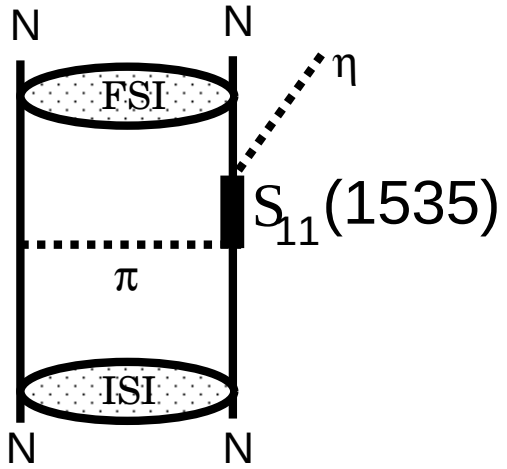

Figure 6.4: The most probable mechanism of η meson production in the nucleon-nucleon collisions: excitation of the nucleon to the $S_{11}(1535)$ resonance via the exchange of a π meson, and its further decay into a nucleon-η system.

We claim to solve this ambiguity by the measurement of the angular dependence of the analysing power presented in this dissertation. The results are presented in Table 5.6 of Chapter 5.6, as well as in Figure 5.20. The χ^2 analysis of the

results allows us to reject the predictions of the vector meson dominance model at a significance level of 0.006. Predictions of the pseudoscalar meson exchange model are in line with data at the significance level of 0.81. This fact, together with the abovementioned presented inference [116] indicate that **in nucleon-nucleon collisions the η meson is produced predominantly by the exchange of a π meson**. The most probable process of η meson production is presented in Figure 6.4.

6.3 A_y and the final state of the ppη system

Based on the experimental data we infer on the final state of the η meson in the $pp\eta$ system.

The analysing power determined in this thesis is within the statistical accuracy consistent with zero, at both excess energies. This result implies that **the η meson is predominantly produced in the s-wave in the close-to-threshold region** [59]. This observation is in agreement with the results of the analysing power measurements performed by the DISTO collaboration [15] where, interestingly, in the far-from-threshold energy region A_y was also found to be consistent with zero within one standard deviation.

Chapter 7

Perspectives

Some ideas on extending the experiments presented in this thesis are pointed out. An experiment for resolving the final state partial waves of the $pp\eta$ system is proposed. It is mentioned that the measurements with the new WASA-at-COSY facility would significantly increase the statistics.

The improvement of the statistics concerning the data on the analysing power for the $\vec{p}p \to pp\eta$ reaction would be possible by means of the measurement of this observable with the recently brought to operation 4π detector WASA-at-COSY [69]. Due to the installation of a pellet target, high luminosities for the experiments with polarised proton beams are expected to be achieved, and are estimated to be at the order of $6{\cdot}10^{29}\mathrm{cm}^{-2}\mathrm{s}^{-1}$. This would yield around 20000 η events per day measured at an excess energy of 10 MeV and about 70000 events at an excess energy of 36 MeV. Therefore, a one-week measurement of the analysing power using the WASA-at-COSY detection setup would yield the result with circa 20 times better statistical significance[1] than measurements reported in this dissertation. The letter of intent for such an experiment has already been published by the COSY-11 collaboration [117] and is awaiting realisation.

Another interesting experiment would be the measurement of the spin correlation coefficients C_{xx} for the $\vec{p}\vec{p} \to pp\eta$ reaction. As proposed by Nakayama et al. [59], measurements of this observable would be helpful to extract the contributions of the individual partial waves for the $pp \to pp\eta$ reaction in the close-to-threshold energy region. Namely, restricting to the η meson production in the s-wave[2] and final proton-proton state in the S and P waves there are only three partial waves[3] that can possibly contribute to the $pp \to pp\eta$ reaction [27]:

[1] Evaluation valid for the experiment performed at the excess energy of Q = 36 MeV

[2] Which is confirmed by the results presented in this thesis.

[3] Here the following notation of the partial waves has been used: ${}^{2S+1}L_J \to {}^{2S'+1}L'_{J'}l$, with S, L, and J denoting the total spin, orbital angular momentum, and total angular momentum of two protons in the initial state. The prime values are corresponding quantities in the final state. l stands for the orbital momentum of the η meson with respect to the pair of protons.

$^3P_0 \rightarrow ^1S_0s$, $^1S_0 \rightarrow ^3P_0s$, and $^1D_2 \rightarrow ^3P_2s$. Denoting the amplitudes of these transitions by α, β, and γ, respectively, yields [59]:

$$\frac{d\sigma}{d\Omega} = |\alpha|^2 + k^2\left(|\beta+\gamma|^2 + 3x^2\left(|\gamma|^2 - 2Re\left(\beta\gamma^*\right)\right)\right),$$

$$\frac{d\sigma}{d\Omega}A_y = 0,$$

$$\frac{d\sigma}{d\Omega}C_{xx} = |\alpha|^2 - k^2\left(|\beta+\gamma|^2 + 3x^2\left(|\gamma|^2 - 2Re\left(\beta\gamma^*\right)\right)\right), \tag{7.1}$$

with k and p standing for the relative momentum in the final and initial proton-proton system, respectively, and $x = \hat{k}\cdot\hat{p}$. From the above equation it is clear that the quantity $\frac{d\sigma}{d\Omega}(C_{xx}+1)$ depends only on the amplitude α. Therefore measuring the spin correlation functions in the region where the differential cross sections for the $pp \rightarrow pp\eta$ reaction are known would provide the model-independent information about the magnitude of the $^3P_0 \rightarrow ^1S_0s$ transition. In a similar way, the combination $\frac{d\sigma}{d\Omega}(C_{xx}-1)$ different than zero would indicate the presence of higher partial waves in the proton-proton final state. Authors of [59] also provide the predictions for the C_{xx} angular dependence, which are presented in Figure 7.1.

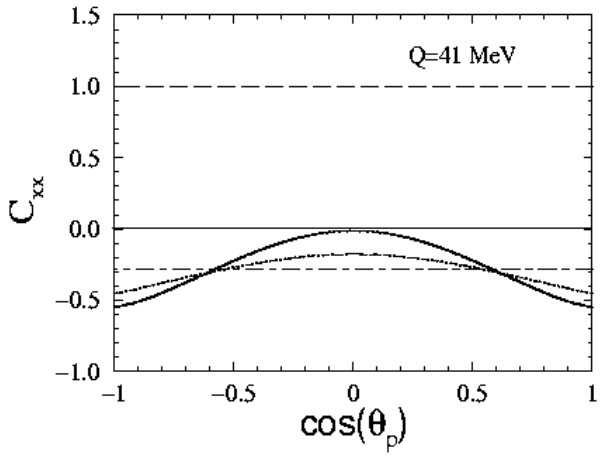

Figure 7.1: Predictions of the spin correlation coefficient C_{xx} for the $\vec{p}\vec{p} \rightarrow pp\eta$ reaction as a function of the final proton angle in the overall centre-of-mass system at the excess energy of Q = 41 MeV. The meaning of the curves is explained in the text.

The dashed line in Figure 7.1 assumes $^3P_0 \rightarrow ^1S_0s$ transition only, leading to the constant value of C_{xx} equal to 1. The dash-dotted line apart from $^3P_0 \rightarrow ^1S_0s$

The values of the angular momenta are expressed in the spectroscopic notation: L = S, P, D,... and l = s, p, d,...

transition takes into account also the transition ${}^1S_0 \rightarrow {}^3P_0 s$. In this case the authors also obtained a constant value of $C_{xx} \approx -0.3$. Inclusion of the ${}^1D_2 \rightarrow {}^3P_2 s$ contribution results in the dotted line. Taking into account the higher partial waves would end up with the angular dependence of C_{xx} being given by the solid curve in Figure 7.1.

The abovementioned experiment has been proposed by the COSY-11 collaboration [117] to be performed on the new WASA-at-COSY detector setup. However there are many technical challenges to be fulfilled before the determination of this measurement will become possible.

Chapter 8

Summary

We have presented the theoretical background, the method of measurement and the results of experiments aiming in determination of the analysing power for the $\vec{p}p \to pp\eta$ reaction in the close-to-threshold energy regime. Measurements have been performed utilizing the polarised proton beam of the COSY accelerator, the cluster jet target delivering jets of H_2 molecules, and the COSY-11 experimental facility used to register and identify the reaction products. For the η meson identification the missing mass method has been applied. The monitoring of relative luminosity has been realized with a dedicated detection subsystem, presented in Section 5.3, measuring the differences in the numbers of reactions taking place in the polarisation plane during the spin up and down modes. The degree of polarisation has been determined by means of a series of measurements of asymmetries for the $\vec{p}p \to pp$ process, utilising three independent polarimeters. Experiments have been performed at beam momenta of $p_{beam} = 2.010$ and 2.085 GeV/c, which for the $\vec{p}p \to pp\eta$ reaction correspond to the excess energies of Q = 10 and 36 MeV, respectively. Results of the data analysis are summarized in Section 5.6.

For the first time ever it was possible to experimentally pin down the dominating production mechanism of the η meson in nucleon-nucleon collisions. Our results indicate, at a significance level of 0.81, that the π meson is an intermediate boson exchanged between colliding nucleons in order to excite one of them to the resonant state $S_{11}(1535)$. In the latter part of the process, this baryonic resonance deexcites with emission of a nucleon and the η meson, as presented in Figure 6.4. It is important to note, that not only the measurements presented in this dissertation contributed to this finding, but also many hitherto performed investigations by various experimental groups have been important in the understanding of this process [2–10, 12, 13].

We have also shown that the predictions of the analysing power angular dependence according to the vector meson exchange model [14], where the ρ meson plays the most important role as an intermediate particle exciting the nucleon to the S_{11} state, disagree with the experimental data at a significance level of $\alpha_{vec} = 0.006$. This result is intuitively clear and understood, as the branching ratio of the $S_{11}(1535)$ decay into Nπ channel is about 45%, which is an order of

magnitude larger than the branching ratio for a decay into a $N\rho$ pair, measured to be at circa 4% [99]. Moreover, the coupling constant for the $NN\pi$ vertex is larger than the corresponding coupling constants for the $NN\omega$, $NN\rho$, $NN\eta$ vertices.

One should, however, keep in mind that the interferences in the exchange of different types of mesons are not excluded and should be studied theoretically and experimentally by the measurement of further spin observables.

The analysing power of the $\vec{p}p \to pp\eta$ reaction for both excess energies studied in this work was found to be consistent with zero within one standard deviation. This may suggest that the η meson is predominantly produced in the s-wave, an observation which is in agreement with the results of the analysing power measurements performed by the DISTO collaboration [15] where, interestingly, in the far-from-threshold energy region the A_y was found to be also consistent with zero within one standard deviation.

The results of this dissertation might be helpful in revisiting the theoretical models, in the sense that they may provide a new input with respect to the coupling constants used for modeling the η meson production in hadronic interaction, and the range of the reaction.

Acknowledgments

Here I would like to thank all the people who helped me during the years of Ph. D. studies.

First of all I would like to express my enormous gratitude to Dr hab. Paweł Moskal, for devoting his time, the number of ideas that helped to bring this dissertation to life, for his patience and offering me help whenever I needed it.

I am extremely grateful to Prof. Walter Oelert for giving me an opportunity to work in the COSY-11 collaboration, for the invitation to the Research Centre Jülich, and for his help.

I would like to acknowledge Prof. Jim Ritman and Prof. Kurt Kilian for allowing me to work in the Research Centre Jülich.

I am grateful to Prof. Bogusław Kamys for allowing me to prepare this dissertation in the Faculty of Physics, Astronomy and Applied Computer Science of the Jagellonian University.

A big "thank you" to all my colleagues from the COSY-11 collaboration: Dr H.-H. Adam, Prof. Andrzej Budzanowski, Eryk Czerwiński, Damian Gil, Dr Dieter Grzonka, Małgorzata Hodana, Michał Janusz, Prof. Lucjan Jarczyk, Prof. Bogusław Kamys, Dr hab. Alfons Khoukaz, Paweł Klaja, Dr Piotr Kowina, Dr hab. Paweł Moskal, Prof. Walter Oelert, Cezary Piskor-Ignatowicz, Timo Mersmann, Joanna Przerwa, Barbara Rejdych, Dr Tomasz Rożek, Dr Thomas Sefzick, Prof. Marek Siemaszko, Dr hab. Jerzy Smyrski, Alexander Täschner, Dr Peter Winter, Dr Magnus Wolke, Dr Peter Wüstner and Prof. Wiktor Zipper. We had a lot of fun during the beamtimes!

A lot of thanks to the COSY team for providing a good quality beam during the experiments.

Special acknowlegdments must be made to Dr Bernd Lorentz and Dr Kay Ulbrich for providing the data on the beam polarisation.

For providing the predictions for A_y special thanks are due to Prof. Kanzo Nakayama, K. S. Man, Prof. Göran Fäldt and Prof. Colin Wilkin.

I'd like to express my gratitude to the others who helped me with their ideas, especially to: Dr Dieter Grzonka, Prof. Lucjan Jarczyk, Dr Piotr Kowina, Prof. Walter Oelert, Cezary Piskor-Ignatowicz, Dr Thomas Sefzick, Dr hab. Jerzy Smyrski, Dr Peter Winter, Dr Magnus Wolke, and Dr Aleksandra Wrońska.

For careful reading and correcting this dissertation my gratitude is due to Dr Dieter Grzonka, Dr hab. Paweł Moskal, Dr Thomas Sefzick and Dr Andrew Smith.

I am also very grateful to Dr Bernd Lorentz, Dr Hans Stockhorst and Dr Ralf Gebels for correcting some parts of this thesis.

Thanks to all my colleagues from "the room 03A" and from IKP for the pleasant atmosphere of the daily work.

I am very grateful to my parents Zofia and Emil, and also to Julia and Anita for their support.

Finally, I am indebted to Paulina Piwowarska for her patience and understanding...

Appendix A

Pseudoscalar and vector mesons

Definitions of the pseudoscalar and vector mesons as well as differences between isoscalar and isovector mesons are given. The structures of the mesons building up the pseudoscalar and vector mesons nonet are given.

According to QCD, mesons are bound states of quark q and antiquark $\bar{q}'$. The quarks q and $\bar{q}'$ may be the same or different. As quarks and antiquarks are the spin 1/2 particles, they may form triplet states ($\uparrow\uparrow$) with the total intrinsic spin J = 1, and singlet states ($\uparrow\downarrow$) with J = 0.

By convention, each quark is assigned positive parity and each antiquark has negative parity. If L denotes the orbital angular momentum of the $q\bar{q}'$ pair, then the parity of the meson built out of this pair equals P = $(-1)^{L+1}$.

From the three lightest quarks – u, d, and s – whose properties are quoted in Table A.1, nine possible $q\bar{q}'$ combinations can be built. This set of SU(3) mesons includes the octet and a singlet states, which can be schematically written as:

$$\mathbf{3} \otimes \overline{\mathbf{3}} = \mathbf{8} \oplus \mathbf{1}. \tag{A.1}$$

Let us assume that $q\bar{q}'$ are the ground state combinations of quark-antiquark pairs with the relative angular momentum L = 0. This implies the parity P of a such constructed meson equals -1. With this condition, the mesons with internal spin J = 0 are called *pseudoscalar mesons* and the ones with J = 1 are called *vector*

Quark	B - baryon number	Q - electric charge	I_3 - isospin third component	S - strangeness
u	1/3	+2/3	+1/2	0
d	1/3	−1/3	−1/2	0
s	1/3	−1/3	0	−1

Table A.1: Additive quantum numbers of the SU(3) quarks. By convention, the flavours of the quarks (I_3 and S) have the same signs as their charges Q.

mesons. The ground state pseudoscalar and vector meson nonets are depicted in Figure A.1.

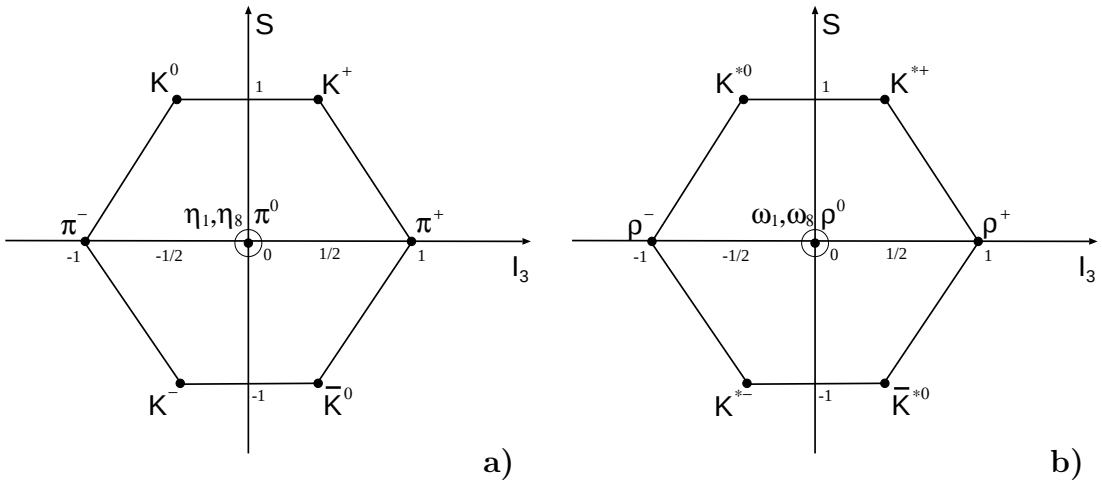

Figure A.1: The nonet of the ground state (a) pseudoscalar ($J^P = 0^-$) and (b) vector ($J^P = 1^-$) mesons. The strangeness S of the meson is plotted versus the third component of its isospin I_3. The neutral mesons at the centre of the S-I_3 plane are the pure mixtures of $u\bar{u}$, $d\bar{d}$, and $s\bar{s}$ states.

States with the same additive quantum numbers, and also the same isospin, total internal spin, and parity can mix. This is a consequence of the SU(3) symmetry breaking. The singlet SU(3) state of the pseudoscalar meson nonet – η_1 – corresponds to the following combination of quarks:

$$\eta_1 = \frac{1}{\sqrt{3}}(u\bar{u} + d\bar{d} + s\bar{s}), \tag{A.2}$$

which mixes with the η_8 state, belonging to the SU(3) octet:

$$\eta_8 = \frac{1}{\sqrt{6}}(u\bar{u} + d\bar{d} - 2s\bar{s}). \tag{A.3}$$

These two states are not the real physical objects. Real mesons which can be observed in the experiments – η and η' – are the mixtures of these pure SU(3) states:

$$\begin{aligned} \eta &= cos(\theta_{psc})\eta_8 - sin(\theta_{psc})\eta_1, \\ \eta' &= sin(\theta_{psc})\eta_8 + cos(\theta_{psc})\eta_1, \end{aligned} \tag{A.4}$$

where a pseudoscalar mixing angle $\theta_{psc} = -15.5^\circ$ has been introduced [118].

Similarly, within the vector meson nonet the theoretical SU(3) states ω_1 and ω_8 mix with each other. This mesons have the quark content corresponding to

Pseudoscalar mesons	Quark combination	Mass [MeV]
π^+	$u\bar{d}$	139.57
π^-	$d\bar{u}$	139.57
π^0	$\frac{1}{\sqrt{2}}\left(u\bar{u}-d\bar{d}\right)$	134.98
K^+	$u\bar{s}$	493.68
K^0	$d\bar{s}$	497.67
K^-	$\bar{u}s$	493.68
$\bar{K}^0$	$\bar{d}s$	497.67
η	$A_1\left(d\bar{d}+u\bar{u}\right)+B_1\left(s\bar{s}\right)$	547.30
η'	$A_2\left(d\bar{d}+u\bar{u}\right)+B_2\left(s\bar{s}\right)$	957.78
Vector mesons	**Quark combination**	**Mass [MeV]**
ρ^+	$u\bar{d}$	769.3
ρ^-	$d\bar{u}$	769.3
ρ^0	$\frac{1}{\sqrt{2}}\left(u\bar{u}-d\bar{d}\right)$	769.3
K^{*+}	$u\bar{s}$	891.66
K^{*0}	$d\bar{s}$	896.10
K^{*-}	$\bar{u}s$	891.66
$\bar{K}^{*0}$	$\bar{d}s$	896.10
ω	$C_1\left(d\bar{d}+u\bar{u}\right)+D_1\left(s\bar{s}\right)$	782.57
ϕ	$D_2\left(d\bar{d}+u\bar{u}\right)+D_2\left(s\bar{s}\right)$	1019.42

Table A.2: Pseudoscalar and vector mesons as the quark-antiquark combinations. Masses of the mesons are taken from [120].

the η_1 and η_8 states, respectively. The physical states ω and ϕ, analogous to the abovementioned η and η' pseudoscalar combinations, are the result of the ω_1 and ω_8 mixing with a mixing angle $\theta_{vec} = 37^\circ$ [119].

The quark structure of the ground state pseudoscalar and vector mesons together with their masses are presented in Table A.2.

The mesons with the total isospin I = 0, like the η and η' mesons within the pseudoscalar meson nonet and the ϕ and ω mesons in the case of the vector meson nonet are called the *isoscalar mesons*.

By the *isovector mesons* we refer to either pseudoscalar or vector mesons with a total isospin I = 1. These are the π and ρ mesons, for the pseudoscalar and vector meson nonet, respectively.

Appendix B

Property of the average analysing power

A proof of the following theorem is presented.

Theorem 1. *For an isotropic distribution of the differential cross section* $\frac{d\sigma}{d\theta}(\theta) = const$*, the average analysing power over an angular range* $\Delta\Theta$ *is an arithmetical average of the analysing powers for the individual* $\Delta\theta_i$ *subranges of* $\Delta\Theta$*:*

$$\bar{A}_y(\Delta\theta) = \frac{\sum_{i=1}^{n} A_y(\Delta\theta_i)}{n}. \tag{B.1}$$

Proof. Without loosing generality, let us consider the production of the η mesons during spin up mode in the plane perpendicular to the polarisation plane. Let the $N_L(\Delta\Theta)$ and $N_R(\Delta\Theta)$ denote the number of the η mesons produced into the $\Delta\Theta$ range, symmetrically with respect to the polarisation plane to the left and right side, respectively. If P denotes the beam polarisation then, according to the Formula 2.19, the averaged beam analysing power for the η meson production into the $\Delta\Theta$ angular range reads:

$$\bar{A}_y(\Delta\Theta) = \frac{1}{P}\frac{N_L(\Delta\Theta) - N_R(\Delta\Theta)}{N_L(\Delta\Theta) + N_R(\Delta\Theta)}. \tag{B.2}$$

Applying the Madison convention defined in Chapter 2.2 and taking into account that the production yields N_L and N_R are proportional to the cross section of Equation 2.13 and under assumption that $\frac{d\sigma}{d\theta}(\Delta\theta) = const$ we can write:

$$N_L(\Delta\Theta) \sim \Delta\Theta\,(1 + PA_y(\Delta\Theta))\,, \tag{B.3}$$

$$N_R(\Delta\Theta) \sim \Delta\Theta\,(1 - PA_y(\Delta\Theta))\,. \tag{B.4}$$

Dividing the $\Delta\Theta$ range into n identical subranges $\Delta\theta_i$ we can rewrite Equations B.3 and B.4:

$$N_L(\Delta\Theta) \sim \sum_{i=1}^{n} \Delta\theta_i\,(1 + PA_y(\Delta\theta_i)), \tag{B.5}$$

$$N_R(\Delta\Theta) \sim \sum_{i=1}^{n} \Delta\theta_i\,(1 - PA_y(\Delta\theta_i)). \tag{B.6}$$

Putting Equations B.5 and B.6 into Formula B.2 yields:

$$\bar{A}_y(\Delta\Theta) = \frac{1}{P}\frac{\sum_{i=1}^{n}\Delta\theta_i\,(1 + PA_y(\Delta\theta_i)) - \sum_{i=1}^{n}\Delta\theta_i\,(1 - PA_y(\Delta\theta_i))}{\sum_{i=1}^{n}\Delta\theta_i\,(1 + PA_y(\Delta\theta_i)) + \sum_{i=1}^{n}\Delta\theta_i\,(1 - PA_y(\Delta\theta_i))}, \tag{B.7}$$

which after reductions leads to:

$$\bar{A}_y(\Delta\Theta) = \frac{\sum_{i=1}^{n}\Delta\theta_i A_y(\Delta\theta_i)}{\sum_{i=1}^{n}\Delta\theta_i} = \frac{\Delta\theta_i\sum_{i=1}^{n}A_y(\Delta\theta_i)}{n\Delta\theta_i} = \frac{\sum_{i=1}^{n}A_y(\Delta\theta_i)}{n}. \tag{B.8}$$

□

One should mention at this point that the inference presented here does not necessarily demands the subranges $\Delta\theta_i$ to be of the same width. This is because one can always divide an arbitrarily chosen subrange $\Delta\theta_i$ into m infinitesimally small subsubranges, division for which the prove has just been presented.

For $n \to \infty$ the relation B.8 becomes:

$$\bar{A}_y\left(\Delta\Theta\right) = \frac{\int_{\theta_1}^{\theta_2} A_y\left(\theta\right) \mathrm{d}\theta}{\int_{\theta_1}^{\theta_2} \mathrm{d}\theta}. \tag{B.9}$$

Appendix C

Parity invariance and the analysing power

It is shown that according to the parity invariance rule the analysing power in the polarisation plane equals zero, hence the scattering yields in the polarisation plane may be used as an absolute measure of the luminosity.

The parity transformation is the reflection of the system with respect to the origin of the reference frame. Parity is a multiplicative quantum number, which is conserved by the strong and electromagnetic interactions.

Parity transformation may also be represented by a threefold reflection of the system in a mirror situated in the $y-z$, $x-z$, and $x-y$ planes. This operation transforms the right handed (x,y,z) frame into the left handed (x',y',z') frame, as depicted in Figure C.1.

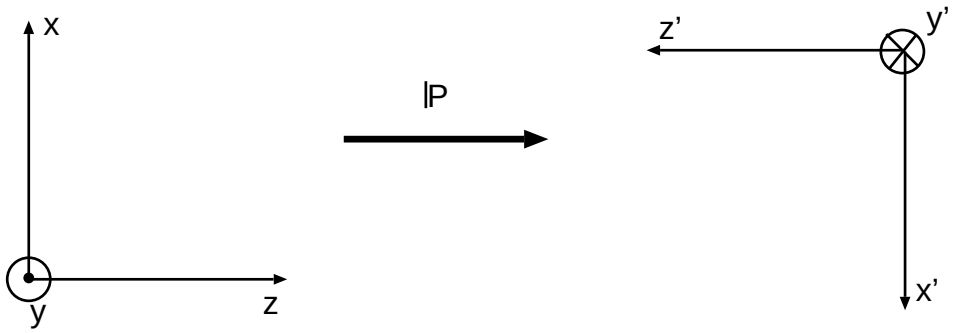

Figure C.1: Parity transformation.

Please note that spin, and as a consequence the polarisation vector, is invariant under the parity reversal and that these objects transform as the *pseudovectors* [1].

[1]The other example of the pseudovector is the angular momentum, which has the same

Indeed, if we considered the particle with its spin along the y axis we would notice that the spin vector changes its direction upon reflecting it in the mirrors positioned perpendicularily to x and z axis, but does not change the direction when mirrored in the plane perpendicular to the y axis. As a consequence spin does not change its direction under the parity transformation.

Now, without loosing generality, let us consider the scattering of a particle with spin along the y axis in the $x - z$ plane, as depicted in Figure C.2.a. We shall also assume that there is an asymmetry in the left-right scattering in the $x - z$ plane, i.e. that the scattering yields N_1 and N_2 are different.

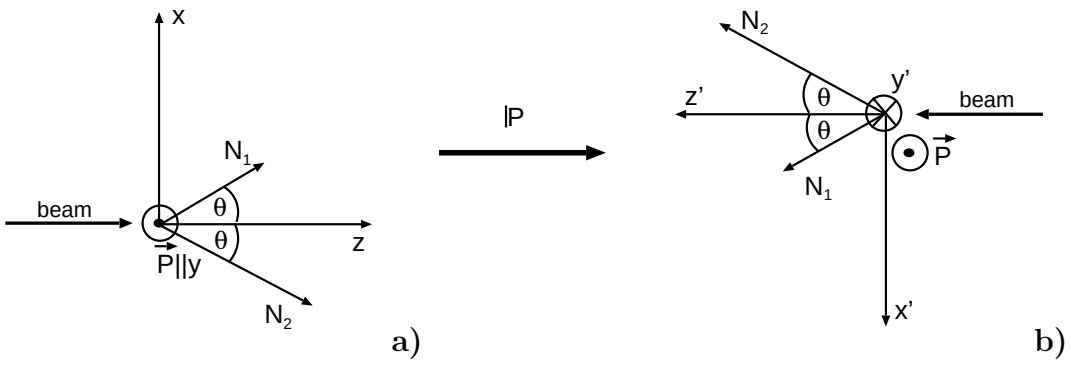

Figure C.2: Parity reversal for scattering in the plane perpendicular to the polarisation plane.

The parity reversal transforms the state presented in Figure C.2.a into the one in Figure C.2.b. Please note, that the transformed state of Figure C.1.b is physically identical with the initial state from Figure C.2.a, as there exist an invariant transformation – which is a rotation by angle π around the y axis – that transforms the final state into initial one. Naturally, the (x',y',z') frame remains a left-handed frame, but the physics of the process does not depend on the choice of the reference frame.

Situation is different when we consider the scattering of a particle with a spin along the y axis in the polarisation plane. Again we assume that scattering yields N_1 and N_2 are different. The initial state and the state resulting from the parity transformation are depicted in Figure C.3.a and C.3.b, respectively.

transformation properties as a spin.

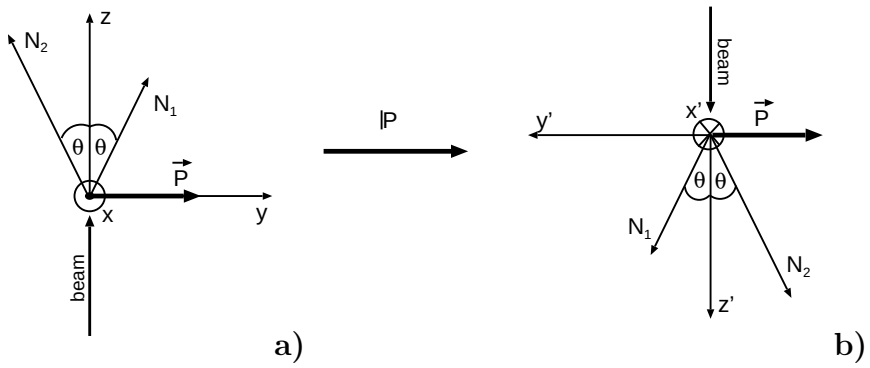

Figure C.3: Parity reversal for scattering in the polarisation plane.

In this case no invariant transformation exists that could retransform the final state into initial one. We note that the rotation about the y axis does not work in this case, as the directions of N_1 and N_2 after the rotation are reversed. This situation is therefore physically not allowed as it would violate the parity invariance rule, which holds for strong interactions.

However, the initial and transformed states would be identical if N_1 and N_2 were equal. Therefore, if the studied reaction is invariant under the parity transformation it cannot result in the asymmetry of yields in the polarisation plane. This demands the analysing power A_y in the polarisation plane must be equal to zero.

Therefore the scattering in the polarisation plane does not depend on the degree of beam polarisation, and the scattering yields in the polarisation plane may be used as an absolute measure of the luminosity.

Bibliography

[1] A. Pevsner et al., Phys. Rev. Lett. **7** (1961) 421.

[2] A. M. Bergdolt et al., Phys. Rev. **D 48** (1993) 2969.

[3] E. Chiavassa et al., Phys. Lett. **B 322** (1994) 270.

[4] H. Calén et al., Phys. Lett. **B 366** (1996) 39.

[5] H. Calén et al., Phys. Rev. Lett. **79** (1997) 2642.

[6] F. Hibou et al., Phys. Lett. **B 438** (1998) 41.

[7] J. Smyrski et al., Phys. Lett. **B 474** (2000) 182.

[8] P. Moskal et al., Phys. Rev. **C 69** (2004) 025203.

[9] P. Moskal et al., arXiv: nucl-ex/0208004.

[10] P. Moskal et al., Nucl. Phys. **A 721** (2003) 657.

[11] K. Nakayama et al., Phys. Rev. **C 65** (2002) 045210.

[12] M. Abdel-Bary et al., Eur. Phys. J. **A 16** (2003) 127.

[13] H. Calén et al., Phys. Rev. **C 58** 2667 (1998).

[14] G. Fäldt and C. Wilkin, Phys. Scripta **64** (2001) 427.

[15] F. Balestra et al., Phys. Rev. **C 69** (2004) 064003.

[16] P. Winter et al., Phys. Lett. **B 544** (2002) 251; erratum-ibid. **553** (2003) 339.

[17] P. Winter, Diploma Thesis, Rheinische Friedrich-Wilhelms-Universität Bonn (2002), IKP Jül-3943.

[18] S. Brauksiepe et al., Nucl. Instr. & Meth. **A 376** (1996) 397.

[19] P. Klaja et al., AIP Conf. Proc. **796** (2005) 160.

[20] J. Smyrski et al., Nucl. Instr. & Meth. **A 541** (2005) 574.

[21] R. Maier, Nucl. Instr. & Meth. **A 390** (1997) 1.

[22] `http://www.fz-juelich.de/ikp/ikp-general/cosyh_e.html`

[23] P. Moskal, Ph.D. Dissertation, Jagellonian University of Cracow (1998), IKP Jül-3685.

[24] M. Wolke, Ph.D. Dissertation, Rheinische Friedrich-Wilhelms-Universität Bonn (1998), IKP Jül-3532.

[25] P. Winter, Ph.D. Dissertation, Rheinische Friedrich-Wilhelms-Universität Bonn (2005), IKP Jül-4177.

[26] Conference Proceedings: "*Polarisation Phenomena in Nuclear Reactions*", University of Wisconsin Press, Madison (1971) pp. XXV.

[27] P. Moskal, e-print arXive: hep-ph/0408162; Habilitation Dissertation, Jagellonian University Press (2004).

[28] M. Altmeier et al., Phys. Rev. Lett. **85** (2000) 1819.

[29] C. Hanhart, Phys. Rep. **397** (2004) 155.

[30] P. Moskal, M. Wolke, A. Khoukaz, W. Oelert, Prog. Part. & Nucl. Phys. **49** (2002) 1.

[31] E. Pickup et al., Phys. Rev. Lett. **8** (1962) 329.

[32] G. Alexander et al., Phys. Rev. **154** (1967) 1284.

[33] A. P. Colleraine and U. Nauenberg, Phys. Rev. **161** (1967) 1387.

[34] L. Bodini et al., Nuovo Cimiento **A 58** (1968) 475.

[35] C. Caso et al., Nuovo Cimiento **A 55** (1968) 66.

[36] S. P. Almeida et al., Phys. Rev. **174** (1968) 1638.

[37] E. Colton and E. Geller, Phys. Rev. **D 1** (1970) 1979.

[38] G. Yekutieli et al., Nucl. Phys. **B 18** (1970) 301.

[39] H. Calén et al., Phys. Lett. **B 458** (1999) 190.

[40] B. Tatischeff et al., Phys. Rev. **C 62** (2000) 054001.

[41] P. Moskal et al., πN Newsletter **16** (2001) 367.

[42] J. F. Germond and C. Wilkin, Nucl. Phys. **A 518** (1990) 308.

[43] J. M. Laget et al., Phys. Lett. **B 257** (1991) 254.

[44] A. B. Santra and B. K. Jain, Nucl. Phys. **A 634** (1998) 309.

[45] K. Nakayama, e-Print Archive: nucl-th/0108032.

[46] M. Batinić et al., Phys. Scripta **56** (1997) 321.

[47] E. Gedalin et al., Nucl. Phys. **A 634** (1998) 368.

[48] T. Vetter et al., Phys. Lett. **B 263** (1991) 153.

[49] M. Peña et al., Nucl. Phys. **A 683** (2001) 322.

[50] V. Baru et al., Phys. Rev. **C 67** (2003) 024002.

[51] N. I. Kochelev et al., Phys. Lett. **B 472** (2000) 247.

[52] M. Dillig, e-Print Archive: hep-ph/0202067.

[53] S. Eidelman et al., Phys. Lett. **B 592** (2004) 1.

[54] C. Wilkin, Report No. TSL/ISV-96-0147 (1996).

[55] B. Krusche et al., Phys. Rev. Lett. **74** (1995) 3736.

[56] B. Krusche et al., Phys. Lett. **B 397** (1997) 171.

[57] K. Nakayama and W. G. Love, Phys. Rev. **C 70** (2004) 012201.

[58] K. Nakayama et al., Phys. Rev. **C 69** (2004) 065212.

[59] K. Nakayama et al., Phys. Rev. **C 68** (2003) 045201.

[60] J. Dietrich et al., Instrum. Exp. Tech. **46** (2003) 581.

[61] `http://www.fz-juelich.de/ikp/anke/en/index.shtml?`

[62] `http://ikpe1101.ikp.kfa-juelich.de/`

[63] `http://www.fz-juelich.de/ikp/pisa.index.html`

[64] `http://www.fz-juelich.de/ikp/gem/gem.html`

[65] `http://www.iskp.uni-bonn.de/gruppen/hires/index.html`

[66] `http://www.iskp.uni-bonn.de/gruppen/momo/momo.html`

[67] A. Bohm et al., Nucl. Instr. & Meth. **A 443** (2000) 238.

[68] http://www.fz-juelich.de/ikp/COSY-TOF/index.html

[69] H.-H. Adam et al., Proposal for WASA-at-COSY, e-print arXiv: nucl-ex/0411038;
http://www.fz-juelich.de/ikp/wasa/index.shtml

[70] D. Prasuhn et al., Nucl. Instr. & Meth. **A 441** (2000) 167.

[71] H. Stockhorst et al., IKP Annual Report (1997) 160.

[72] H. Stockhorst, Schriften des FZ-Jülich, Matter and Materials **11** (2002) 176;
D. Moehl, Nucl. Instr. & Meth. **A 391** (1997) 164;
F. Caspers, Conference Proceedings of the International Symposium on Multi-GeV High Performance Accelerators and Related Techniques, Osaka, Japan, 12-14 March 1997, CERN/PS 97-13 (RF).

[73] R. Weidmann et al., Rev. Sci. Instrum. **67(3)** (1996) 1357.

[74] G.I. Budker et al., Proceedings of the International Conference on High-Energy Accelerators Dubna (1963);

[75] H. Stockhorst, Schriften des FZ-Jülich, Matter and Materials **21** (2004) 106.

[76] R. Gebel, private communication (2006).

[77] V. Bargman et al., Phys. Rev. Lett. **2** (1959) 43.

[78] A. Lehrach, Ph.D. Dissertation, Rheinische Friedrich-Wilhelms-Universität Bonn (1997), IKP Jül-3501.

[79] H. Dombrowski et al. Nucl. Inst. & Meth. **A 386** (1997) 228.

[80] A. Khoukaz et al., Eur. Phys. J. **D 5** (1999) 275.

[81] B. Gugulski et al., Annual Report KFA-IKP(I)-1992-3.

[82] M. Sokołowski et al., Annual Report IKP-KFA 1990 (1991) 219.

[83] Bicron Corporation, Newburry, OH 44065, USA.

[84] M. Wolke, Diploma Thesis, Westfälische Wilhelms-Universität Münster (1993), IKP Jül-2852.

[85] R. Czyżykiewicz, Diploma Thesis, Jagellonian University of Cracow (2002), IKP Jül-4017.

[86] R. Bilger et al., Nucl. Instr. & Meth. **A 457** (2001) 64.

[87] M. Janusz and P. Moskal, Schriften des FZ-Jülich, Matter and Materials **21** (2004) 238.

[88] P. Moskal et al., J. Phys. **G 32** (2006) 629.

[89] P. Moskal, Schriften des FZ-Jülich, Matter and Materials **21** (2004) 249.

[90] P. Moskal, Annual Report IKP-KFA (1996) 35.

[91] J. Przerwa, e-print arXiv: hep-ex/0408016, Diploma Thesis, Jagellonian University of Cracow (2002), IKP Jül-4141.

[92] T. Rożek, Ph.D. Dissertation, Unniversity of Silesia (2005), IKP Jül-4184.

[93] M. Siemaszko, Schriften des FZ-Jülich, Matter and Materials **11** (2002) 194.

[94] J. Smyrski et al., Nucl. Instr. & Meth. A 541 (2005) 574.

[95] T. Sefzick, Annual Report of IKP (2002) 14, Berichte des FZ-Jülich, Jül-4052.

[96] T. Tanimori et al., Nucl. Instr. & Meth. **216** (1983) 57.

[97] P. Moskal et al. Nucl. Inst. & Meth. **A 466** (2001) 448.

[98] E. Byckling, K. Kajantie, "*Particle Kinematics*", John Wiley & Sons Ltd. (1973).

[99] W.-M. Yao et al., J. Phys. G: Nucl. Part. Phys. **33** (2006) 1.

[100] R. Czyżykiewicz, Schriften des FZ-Jülich, Matter and Materials **21** (2004) 122.

[101] GEANT - Detector Description and Simulation Tool, CERN Program Library Long Writeups W5013 (1994).

[102] D. Albers et al., Phys. Rev. Lett. **78** (1997) 1652.

[103] F. Bauer et al., Nucl. Inst. & Meth. **A 431** (1999) 385.

[104] G. G. Ohlsen and P. W. Keaton, Nucl. Inst. & Meth. **109** (1973) 41.

[105] B. Lorentz, private communication (2003).

[106] `http://www.iskp.uni-bonn.de/gruppen/edda/publ/eddaDSG.html`

[107] `http://www.iskp.uni-bonn.de/gruppen/edda/publ/epjANdata.html`

[108] P.D. Eversheim et al., Nucl. Phys. **A 626** (1997) 117c.

[109] F. Bauer et al., Phys. Rev. **C 71** (2005) 054002.

[110] http://www.iskp.uni-bonn.de/gruppen/edda/publ/edda_prc04_Aij_data.html

[111] V. Schwarz et al., Conference Proceedings of 13th International Symposium on High-Energy Spin Physics (SPIN 98) (1998) 560.

[112] K. Ulbrich, private communication (2005).

[113] MINUIT - Minimization Package, CERN Program Library Long Writeups D506 (1994).

[114] J. R. Taylor, "*An Introduction to Error Analysis, The Study of Uncertainties in Physical Measurements, 2 ed*", University Science Books (1997).

[115] K. Nakayama and K. S. Man, private communication (2005).

[116] P. Moskal et al., e-print arXiv: hep-ex/0609035.

[117] P. Winter and R. Czyżykiewicz et al., e-print arXiv: nucl-ex/0406034.

[118] A. Bramon et al., e-print arXiv: hep-ph/9711229.

[119] Y. Nambu and J. Sakurai, Phys. Rev. Lett. **8** (1962) 79.

[120] D. E. Groom et al., Eur. Phys. J. **C 15** (2000) 1.